Proceedings of the 4th BSME-ASME International Conference on Thermal Engineering
27-29 December, 2008, Dhaka, Bangladesh

ENGINEERING EDUCATION IN BANGLADESH

Harun Chowdhury[1], Firoz Alam[1], Shyamal Kanti Biswas[2] and Md. Tazul Islam[2]

[1]School of Aerospace, Mechanical and Manufacturing Engineering,
RMIT University, Melbourne, Australia

[2]Department of Mechanical Engineering,
Chittagong University of Engineering & Technology, Bangladesh

E-mail: harun.chowdhury@rmit.edu.au

ABSTRACT

Being eighth most populus country in the world, Bangladesh has made a slow progress in engineering and technical education since its independence in 1971. With only 29 public, 54 private and 2 International universities, its vast young population are significantly deprived of engineering and technical education due to limited seats available to these universities and the country is currently lagging behind most developing countries in Asia. Although, limited progress was made in humanities, basic and applied sciences, agriculture and medical sciences, a vast gap is left in technical and engineering education in Bangladesh. This paper describes the present condition of the engineering education in the country and explores ways to improve the engineering education in order to meet the national as well as global skill demands. Strategic plans, policies and programmes that are required for implementation to meet future technological global challenges are also outlined.

Key words: *Engineering education, course curriculum, accreditation, student feedback.*

1. INTRODUCTION

Engineering education in today's Bangladesh started with the establishment of Dhaka Survey School by the British for their colonial needs in 1876. The Dhaka Survey School was later upgraded and renamed as Ahsanullah Engineering College after partition of British India in 1948. It was further upgraded to a university under the name of East Pakistan University of Engineering and Technology in 1962. Later it was renamed as the Bangladesh University of Engineering and Technology (BUET) after independence in 1971. Before 1962, only 240 students could enter into this university for several undergraduate engineering programs in erstwhile East Pakistan where Pakistan's majority population lived. Immediately after the independence of Bangladesh, the country required huge technically skilled people for the re-construction of the war savaged country. Unfortunately, it was unable to address the needs due to limited institutional capability and infrastructure. Although four undergraduate degrees offering engineering colleges were established along with lone engineering university, only 1200 students could enter into the engineering undergraduate education till 1986 for the 120 million people. In 1986, the four engineering colleges were upgraded to Bangladesh Institute of Technology (BIT) in the similar format as IIT in neighbouring country, India. Apart from some administrative advances (eg, separation from general university's control) and some lesser degree quality of education and development of infrastructure, no student intake number was increased. As vast population was poor, most students who could not avail the limited places in engineering education were unable to pursue their engineering education elsewhere. The only opportunity existed for around 200 students on merit basis to study in the former Soviet Union (more than 100 engineering students), Eastern European countries (Poland, Bulgaria, former Democratic Republic of Germany, Czechoslovakia, Hungary, Yugoslavia, Romania and Hungary), India and China. Several places have also been offered by Algeria, Turkey and Morocco. However, after the collapse of Soviet Union and East European communist block, these places were disappeared. Only India, China and Turkey still offer some places for undergraduate studies till to date. In short, the growth of engineering education in Bangladesh has been terribly slow since its creation in 1971. Although Bangladesh is one of the largest human resources exporters to the Middle East (9 million) and elsewhere (1 million) in the world but its human resources are predominantly remained unskilled resulting in one of the lowest paid workforce in the world. The remittance could be ten fold if the workforce could be technically skilled and semi-skilled. Relaxation in colonial mentality and opening of education in the private sector in early 1990s, philanthropists, private entrepreneurs and retired educators started to establish several dozen private universities predominantly in the nation’s capital, Dhaka. Whatever the motives of these entrepreneurs might have, the private universities have opened a new horizon in education sector in Bangladesh. These universities are generally offer degrees and courses in business and finance, computer science and IT, and some contemporary programs that are usually not offered by the public universities. However, only couple of private universities offer engineering education. In late 1990s government finally realised that without engineering and science education, it would be extremely difficult to advance the country both domestically and internationally. The governments decided not to establish any public university for general education rather significant emphasis was given to establish more universities for science and technology based education. As a result, several new public universities have established or upgraded focussing on science and technology education (see Table 1). In 2003, all four BITs have been upgraded to full fledged engineering and technological universities and consequently allowing these newly created engineering universities doubling the intake numbers. These universities have also received government conditional approval for opening of new degree offering departments including, automotive engineering, mining engineering, aeronautical engineering, water resources engineering etc. However, these universities show little interest in opening new programs as they have been facing severe shortages of qualified academics and researchers, resources and infrastructures.

The primary objective of this paper is to discuss the current status of education, especially engineering education in Bangladesh. The paper also describes some practices undertaken by the universities of the developed world for the enhancement of quality of engineering education. Some practices can be applied with minor or no modification to Bangladesh engineering education systems in order to prepare graduates for both national and global employment.

2. ENGINEERING EDUCATION IN THE UNIVERSITIES IN BANGLADESH

There are mainly three major types of university operating their activities in Bangladesh. These are:

a) Public university, funded by the government
b) Private university, funded by the private donors, philanthropists, entrepreneurs and students fees,
c) International university, mainly funded by various international organisations and host country government

2.1 Public University

Currently there are 29 publicly funded universities in Bangladesh which control almost 70 percent of higher education sector. These universities are semi-autonomous in governess but financially fully dependent on government. Their funding schemes are managed and controlled by the University Grants Commission (UGC) which is run by the government. The top management of all these public universities are entirely controlled by the government of the day and thus allowing opportunity for external political interference in university's day to day business.

Table 1: Public Universities in Bangladesh in 2008 [16]

SN	Name	Nick	Founded	Region	Specialisation
1	University of Dhaka	DU	1921	Dhaka	General
2	Rajshahi University	RU	1953	Rajshahi	General
3	Bangladesh Agricultural University	BAU	1961	Dhaka	Agriculture
4	Bangladesh University of Engineering and Technology	BUET	1962	Dhaka	Engineering
5	Chittagong University	CU	1966	Chittagong	General
6	Jahangirnagar University	JU	1970	Dhaka	General
7	Islamic University	IU	1980	Khulna	Islam
9	Khulna University	KU	1986	Khulna	General
8	Shahjalal University of Science and Technology	SUST	1987	Sylhet	Technology
10	Bangladesh National University	NU	1992	Country wide	General
11	Bangladesh Open University	BOU	1992	Country wide	General
12	Bangabandhu Sheikh Mujibur Rahman Agricultural University	BSMAU	1998	Dhaka	Agriculture
13	Mawlana Bhashani Science and Technology University	MBSTU	1999	Dhaka	Technology
14	Patuakhali Science and Technology University	PSTU	2002	Barisal	Technology
15	Sher-e-Bangla Agricultural University	SBAU	2002	Dhaka	Agriculture
16	Hajee Mohammad Danesh Science and Technology University	HDUST	2002	Rajshahi	Technology
17	Chittagong University of Engineering and Technology	CUET	2003	Chittagong	Engineering
18	Bangabandhu Sheikh Mujib Medical University	BSMMU	2003	Dhaka	Medical
19	Dhaka University of Engineering and Technology	DUET	2003	Dhaka	Engineering
20	Khulna University of Engineering and Technology	KUET	2003	Khulna	Engineering
21	Rajshahi University of Engineering and Technology	RUET	2003	Rajshahi	Engineering
22	Noakhali Science and Technology University	NSTU	2005	Chittagong	Technology
23	Jagannath University	JNU	2005	Dhaka	General
24	Jatiya Kabi Kazi Nazrul Islam University	KNU	2005	Dhaka	General
25	Chittagong Veterinary and Animal Sciences University	CVASU	2006	Chittagong	Veterinary Sciences
26	Comilla University	UNIC	2006	Chittagong	General
27	Jessore University of Science & Technology	JUST	2006	Khulna	Technology
28	Sylhet Agricultural University	SAU	2006	Sylhet	Agriculture
29	The University of Rangpur	UR	2008	Rajshahi	General

2.2 Private University

Since the introduction of Private University Act by the nation's parliament in 1992, over 54 private universities have been established in Bangladesh. Most of them are concentrated in the capital city, Dhaka (over 25 universities are in one suburb of Dhaka city alone). A complete list of all these universities is shown in Table 2. As mentioned earlier, these universities have opened a new horizon in higher education in Bangladesh. Apart from creating education opportunity in Bangladesh, it can also save millions of dollars to be spent overseas for the overseas education of Bangladeshi students. Although these universities need to work hard to improve the quality of education, they created huge opportunity for the young school leavers to get education in their own country with minimum cost otherwise many of these young talents could be wasted.

Table 2: Private Universities in Bangladesh in 2008 [16]

SN	University	Nick	Founded	Region	Specialization
1	University of Science & Technology Chittagong	USTC	1992	Chittagong	Technology
2	Darul Ihsan University	DIU	1992	Dhaka	General
3	International University of Business Agriculture and Technology	IUBAT	1992	Dhaka	General
4	North South University	NSU	1992	Dhaka	General
5	Central Women's University	CWU	1993	Dhaka	Women's Study
6	Independent University, Bangladesh	IUB	1993	Dhaka	General
7	American International University-Bangladesh	AIUB	1994	Dhaka	General
8	International Islamic University, Chittagong	IIUC	1995	Chittagong	General
9	Ahsanullah University of Science and Technology	AUST	1995	Dhaka	Technology
10	Dhaka International University	DIntU	1995	Dhaka	General
11	Asian University of Bangladesh	AUB	1996	Dhaka	General
12	East West University	EWU	1996	Dhaka	General
13	Gano Bishwabidyalaya	GB	1996	Dhaka	General
14	People's University of Bangladesh	PUB	1996	Dhaka	General
15	Queens University	QU	1996	Dhaka	General
16	University of Asia Pacific (Bangladesh)	UAP	1996	Dhaka	General
17	Southern University, Bangladesh	SUB	2001	Chittagong	General
18	Bangladesh University	BU	2001	Dhaka	General
19	BRAC University	BRACU	2001	Dhaka	General
20	Manarat International University	MIU	2001	Dhaka	General
21	Pundra University of Science and Technology	PUST	2001	Bogra	Technology
22	Sylhet International University	SIU	2001	Sylhet	General
23	Begum Gulchemonara Trust University	BGTU	2002	Chittagong	General
24	Premier University, Chittagong	PU	2002	Chittagong	General
25	City University, Bangladesh	CUB	2002	Dhaka	General
26	Daffodil International University	DIU	2002	Dhaka	General
27	Green University of Bangladesh	GUB	2002	Dhaka	General
28	IBAIS University	IU	2002	Dhaka	General
29	Northern University, Bangladesh	NUB	2002	Dhaka	General
30	Prime University	PU	2002	Dhaka	General
31	South East University	SEU	2002	Dhaka	General
32	Stamford University	SU	2002	Dhaka	General
33	State University of Bangladesh	SUB	2002	Dhaka	General
34	University of Development Alternative	UODA	2002	Dhaka	General
35	Leading University	LU	2002	Sylhet	General
36	Bangladesh University of Business and Technology	BUBT	2003	Dhaka	Technology
37	Eastern University, Bangladesh	EU	2003	Dhaka	General
38	Millennium University	MU	2003	Dhaka	General
39	Presidency University	PU	2003	Dhaka	General
40	Primeasia University	PAU	2003	Dhaka	General
41	Royal University of Dhaka	RUD	2003	Dhaka	General
42	Shanto Mariam University of Creative Technology	SMUCT	2003	Dhaka	General
43	United International University	UIU	2003	Dhaka	General
44	University of Information Technology and Sciences	USTC	2003	Dhaka	General
45	University of South Asia, Bangladesh	USAB	2003	Dhaka	General
46	Victoria University of Bangladesh	VUB	2003	Dhaka	General
47	World University of Bangladesh	WUB	2003	Dhaka	General
48	Metropolitan University	MU	2003	Sylhet	General
49	Atish Dipankar University of Science and Technology	ADUST	2004	Dhaka	Technology
50	University of Liberal Arts Bangladesh	ULAB	2004	Dhaka	General
51	Uttara University	UU	2004	Dhaka	General
52	East Delta University	EDU	2006	Chittagong	General
53	ASA University Bangladesh	ASAUB	2006	Dhaka	General
54	Bangladesh Islami University	BIU	2006	Dhaka	General

2.3 International University

There are only two international universities in Bangladesh. These universities are neither directly managed nor funded by the government, like other public universities. These two universities are the Islamic University of Technology (IUT) which is mainly funded by the Organisation of the Islamic Conference (OIC) and individual foreign donors. It was initially established as the Islamic Centre for Technical and Vocational Training and Research (ICTVTR) to address the technical shortages in OIC member states (57 countries) in 1981. It was upgraded to the Islamic Institute of Technology (IIT) in 1994 and subsequently the Islamic University of Technology (IUT) in 2000 by the OIC. Its total intake number is 310 students from 57 OIC member countries including Bangladesh.

The other international university is the Asian University for Women funded by the Asian University for Women Support Foundation (AUWSF), a US based non-profit organisation. The university got parliamentary approval in 2006 but started to operate in 2008 with a plan to offer undergraduate programs in 2009. It is a general education university to cater the needs of education from disadvantaged women in South Asia, South East Asia and Middle East.

2.4 Demographic Distribution of Universities in Bangladesh

Since 1971, Bangladesh put significant emphasis on primary education and its total education spending currently accounted for 3.5% of GDP. The intra-sectoral allocation for education in the fifth five-year plan (1997-2002) provided primary and mass education with 64.18% of the plan allocation and 24.24% for secondary, Madrasah (religious school) and college education. Universities received only 4.26%, and technical education merely received 3.95% [17]. At present government's spending on technical education is one of the lowest among all other education sectors.

Demographic distribution of public and private universities is shown in Table 3. It indicates that Barisal region (division) has the lowest number of universities about 0.1 university per million of population and Dhaka region (division) has the highest number of universities about 0.24 university per million of population. However, the picture of private universities demographic distribution is alarming as Dhaka division has the highest concentration of the private universities about 0.98 university per million of population.

Figure 1 demonstrates the uneven distribution of the universities throughout Bangladesh. Dhaka has the highest population density and naturally it also has the highest number of universities (e.g., the highest number of university per million people). But in other regions (divisions) there is significantly less number of universities to meet the growing demand of the current regional population. Obviously peoples are migrating to a place where opportunity does exist. As a result, some places like Dhaka becomes overpopulated making the city unsustainable for living.

Table 3: General statistics of number of university in different division with population [18]

Division	Area (Km^2)	Population 2008(Estimated) (Million)	Number of Public Universities	Number of Private Universities	Number of International Universities
Barisal	13296	10	1	0	0
Chittagong	33771	29	5	6	1
Dhaka	31120	46	11	45	1
Khulna	22273	17	3	0	0
Rajshahi	34514	36	3	1	0
Sylhet	12596	9	2	3	0
Total	**147570**	**147**	**25**	**55**	**2**

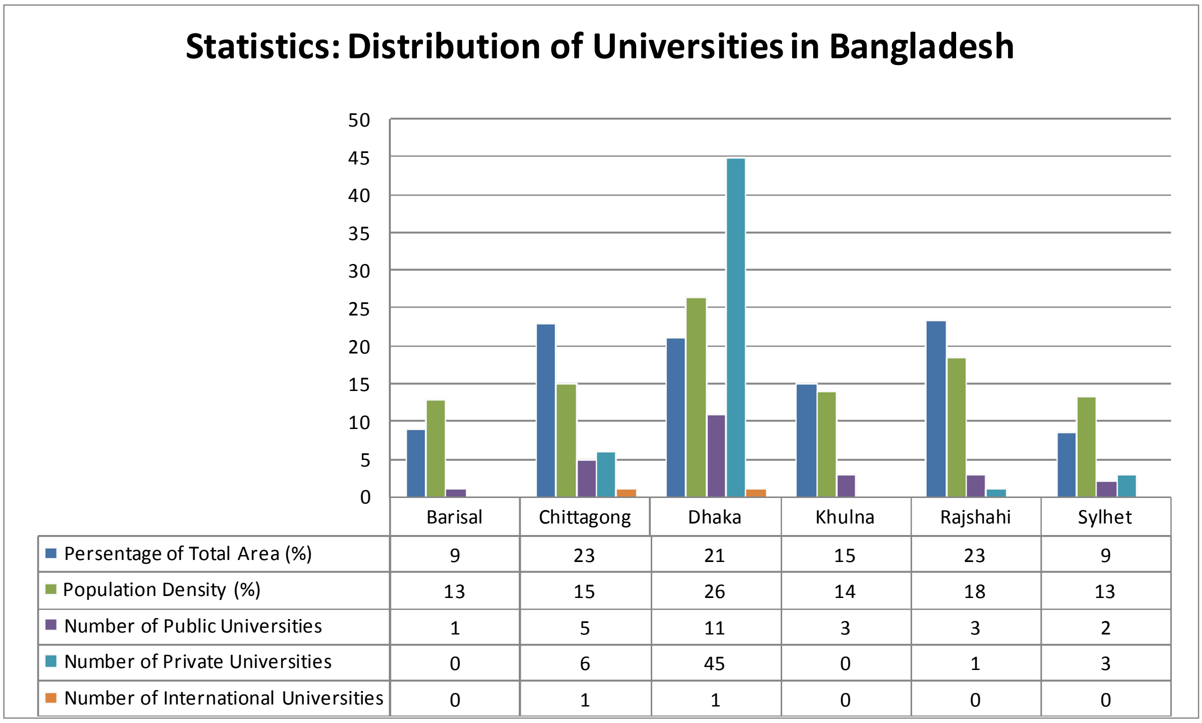

	Barisal	Chittagong	Dhaka	Khulna	Rajshahi	Sylhet
🟦 Persentage of Total Area (%)	9	23	21	15	23	9
🟩 Population Density (%)	13	15	26	14	18	13
🟪 Number of Public Universities	1	5	11	3	3	2
🟦 Number of Private Universities	0	6	45	0	1	3
🟧 Number of International Universities	0	1	1	0	0	0

Figure 1: Distribution of universities through out Bangladesh

3. CURRENT STATUS OF ENGINEERING EDUCATION

According to a report of the University Grants Commission (UGC), the percentages of the scope for higher education are 11.9 in India, 29.3 in Malaysia and 37.3 in Thailand. But in Bangladesh a little over 8% of high school leavers could pursue higher education as the country’s public and private universities do not have adequate number of seats (places) to accommodate them. Prior to independence in 1971, the literacy rate was one of the lowest in the world (less than 10%), therefore, the primary focus on education policy of successive governments was on primary education. It started with the nationalisation of thousands of primary schools in 1973-74 and continued improving and extending primary education and providing opportunities for Education for All (EFA). Primary education was made free and compulsory for all children between the ages of 6 and 10 in 1991 and Bangladesh currently has one of the largest primary education systems in the world. In 2000, there were 76,600 primary schools in Bangladesh and gross enrolment in primary education reached over 96%

[2]. However, negligible investment was made on higher education especially in technical and engineering education.

Although over 500,000 students successfully pass the higher secondary certificate (HSC) examination each year from Bangladesh high school systems, but most of them could not get any places in the higher education systems at all due to very limited combined intake capacity of public and private higher education institutions (155,000). Public universities have capacity for intake of 24,051 students only.

Table 4: Intake Numbers of Bangladesh Higher Education System [14]

Public Universities (29)	**Private Universities (57)**	**Public & Private Medical Colleges (40)**	**University Colleges (61)**	**Degree Colleges (1069)**	**Private Institutions**
24,051	11,000	4,000	55,000	80,000	5,000

For undergraduate engineering programs, only 6000 students are able to get admitted into various engineering programs including computer engineering and computer science in Bangladesh with a population of 150 million. Due to birth rate decline and an increase of precision manufacturing in developed world and elsewhere, demands are huge for technically skilled work forces. Traditional unskilled workforce markets are diminishing and they are replaced with skilled workforce. Bangladesh can tap these markets very effectively thanks to its huge surplus young population (60% of 150 million is under 25 years) [17].

With such a limited intake capacity, still some places are wasted or remain vacant due to complex, chaotic and decentralised tertiary admission systems except medical admission system for public medical and dental colleges. In Bangladesh, there is no centralized admission system based on student HSC and equivalent public examination results. As a result, each university administers its own student admission and selection process at different time and/or same time. This process is informally called “Admission Battle” which is time consuming, frustrating and wastage of resources. A centralised admission system for all public higher education institutions might address this problem. A centralised admission system could not only enhance the quality of intake, but also reduce the anxiety, frustration, financial losses and the wastage of unfilled places. Many developed countries including Australia administer centralised tertiary admission systems.

Table 5 indicates that the maximum number of seats is available for Electrical & Electronic and Communication (EEE/ECE/APECE) and Computer Science & Engineering (CSE) due to increasing demands in the domestic job market. Other engineering also has good domestic demands as country’s GDP is growing increasingly over the decade. A huge demand for textile and leather technology engineering specialists was noted as the garments and textile sectors are emerging as one of the largest manufacturing sectors in the country.

Table 5: Intake number of different engineering programs of universities in 2008 [15]

Institution	ME	CE	EEE/ECE/APECE	CSE	IPE	Chem/ACCT	MME	Petrol	WRE	Naval	URP	Archi	Textile	Leather	Total
BUET	130	180	180	120	180	60	40	-	30	30	30	66	-	-	1046
KUET	120	120	120	60	30	-	-	-	-	-	-	-	-	-	450
CUET	120	120	120	60	-	-	-	-	-	-	-	-	-	-	420
RUET	120	120	120	60	30	-	-	-	-	-	-	-	-	-	450
DUET	120	120	120	60	-	-	-	-	-	-	-	-	60	-	480
SUST	-	60	-	100	50	-	-	30	-	-	-	-	-	-	240
DU	-	-	50	50	-	50	-	-	-	-	-	-	-	-	150
CU	-	-	60	60	-	-	-	-	-	-	-	-	-	-	120
PSTU	-	-	-	90	-	-	-	-	-	-	-	-	-	-	90
HMDSTU	-	-	30	35	-	-	-	-	-	-	-	-	-	-	65
KU	-	-	50	50	-	-	-	-	-	-	-	-	-	-	100
NSTU	-	-	-	60	-	60	-	-	-	-	-	-	-	-	120
MBSTU	-	-	-	50	-	-	-	-	-	-	-	-	50	-	100
JU	-	-	-	60	-	-	-	-	-	-	-	-	-	150	210
BCLT	-	-	-	-	-	-	-	-	-	-	-	-	-	150	150
CTET	-	-	-	-	-	-	-	-	-	-	-	-	180	-	180
MIST	42	45	48	50	-	-	-	-	-	-	-	-	-	-	185
*IUT**	50	-	65	55	-	-	-	-	-	-	-	-	-	-	170
*AUST**	-	100	150	50	-	-	-	-	-	-	-	50	100	-	450
*AIUB**	-	-	150	150	-	-	-	-	-	-	-	150	-	-	450
Total	**702**	**865**	**1263**	**1220**	**290**	**170**	**40**	**30**	**30**	**30**	**30**	**266**	**390**	**300**	**5626**

** Private University*

4. ENGINEERING EDUCATION CURRICULUM AND QUALITY ASSURANCE

Quality of engineering education is paramount, especially in today’s global market. Quality of education depends on a series of factors including contemporary course design, qualification of academic staff and support units, teaching & learning (T&L) facilities and resources, favourable learning environment, student feedback, work integrated learning (WIL) and opportunities. At present quality improvement programs in Bangladesh have so far focused on curriculum and teachers’ training at primary and secondary levels of education system. No visible attempts have been noted in quality improvement programs for tertiary education systems.

4.1 Contemporary Program and Course Curriculum

Course curriculum is the most important part of the engineering education system. Curriculum must be designed to facilitate graduate for immediate employment. Graduate must be prepared for global employability. Like any programs, the engineering program must ensure that its course (subject) structure is responsive to market needs and students demand. It is no doubt that curricula are becoming outdated due to the limited number of international linkages and the lack of up-to-date resources [2]. The courses and programs need to be designed in such a way that it reflects the stage 1 competency [10, 11] which include:

- Knowledge of science and engineering fundamentals
- In-depth technical competence in at least one engineering discipline
- Ability to undertake problem identification, formulation and solution
- Understanding of the social, cultural, global and environmental responsibilities of the professional engineer, and the need to employ principles for sustainable development
- Ability to utilise a systems approach to complex problems and design and operational performance
- Proficiency in engineering design, ability to conduct an engineering project & understanding the business environment

- Ability to communicate effectively, with engineering and with the community at large
- Ability to manage information and documentation
- Capacity for creativity and innovation
- Understanding of professional and ethical responsibilities and commitment to them
- Ability to function effectively as an individual and in multi-disciplinary and multi-cultural teams, with the capacity to be a leader or manager as well as an effective team member
- Capacity for lifelong learning and professional development & professional attitudes
- Graduates have an international perspective; Graduates are global in outlook and competence
- Graduates have an awareness of occupational health and safety issues

Today's engineers need more than just a sound technical background to be successful. In course of solving engineering problems they will need to interact effectively with people of various backgrounds, races, and religions. Therefore, engineering education must offer the students a compelling context for engineering design, a multi-disciplinary team experience, and enough time to learn and practice professional skills, personalized mentoring and exciting technical challenges [15].

4.2 Program Advisory Committee

The Program Advisory Committee (PAC) is mainly composed of internal and external members. The PAC is generally comprised of knowledgeable, committed individuals whose interest in volunteering their own time is sustained by appropriate recognition and rewards achieved in their own fields, i.e., top level professionals from renowned industries (both public and private), senior members of various professional organizations (eg, the Institution of Engineers, Bangladesh, Bangladesh Society of Mechanical Engineer, Bangladesh Computer Society). The primary objectives of the Program Advisory committee are to meet regularly on a long-term basis to provide advice and/or support to an institution and/or one of its programs. By opening a window of exchange with members of the broader society, advisory committee can help institution with a host of important functions: strengthening programs, improving management, reviewing and evaluating mission, programs, and services, recruiting personnel, raising funds, promoting public relations, and improving relationships with other organizations. The first three functions, and sometimes the fourth, are truly advisory in nature, as the committee provides external input into internal processes; the last three fall more into the support category, with committee members serving the organization by helping in the outside world. The Program Advisory Committee becomes an essential part of any engineering degree offering programs in developed world as institutions of higher education and their programs face intense challenges in adapting to and meeting today's needs. Due to tight financial budgets, educational institutions find themselves under increased pressure to do more with less. At the same time, demands and expectations for responsiveness and accountability have increased, requiring greater interaction with the world outside the ivory tower. Advisory committees represent a 'bridge to the external public' and advisory committees can provide mechanisms to help improve communication and interaction with the outside world. They can provide fresh insights, powerful connections, access to valuable resources, and excellent public relations. In conjunction with a strategic plan or total quality management, they can be key elements in renewing and revitalizing an institution. One of the examples is the Program Advisory Committee of the School of Aerospace, Mechanical and Manufacturing Engineering of RMIT University. The committee consists of 10 external people ranging from General Motors Holden Australia, Ford Motor Company of Australia, Royal Automobile Club of Victoria, senior engineers from various engineering consulting firms, Commonwealth Scientific Industrial Research Organisation (CSIRO), various Cooperative Research Centres (CRC), Society of Automotive Engineers Australasia (SAE-A). The committee meets twice a year and the committee comprehensively reviews the program, provide advice and assistance for the future direction. One of the authors of this paper is deeply involved with this process.

4.3 Accreditation of the Programs

Professional accreditation of any engineering program is an integral part of undergraduate engineering education in the developed countries. In today's world, the engineering programs must accredited by the professional bodies any where in the world as reciprocal professional recognition gives graduates global mobility and creates opportunity for global employment. In Australia, undergraduate engineering degree offering programs of all universities are accredited every five years by the Institution of Engineers, Australia (IEAust). In case of an engineering program offered off shore, the IEAust accreditation panel visits off shore location and make sure the quality and standard of program delivery are exactly the same as on shore. If the off shore program fails to comply the set requirements, then on shore program will lose accreditation as well.

In 2003, the Institution of Engineers Bangladesh (IEB) has established the Board of Accreditation for Engineering and Technological Education to oversee the growth and quality of engineering and technical education in the country. It also started to accredit individual engineering program. This is no doubt a first step in the right direction. However, IEB's accreditation board excluded all five public engineering universities (BUET, KUET, CUET, RUET and DUET) from the accreditation process. This exclusion will not bring any good for these universities as well as their graduates. In order to assist engineering graduates from Bangladesh to be recognised globally, the IEB must accredit undergraduate engineering programs of all universities (public & private) without any exclusion and also starts negotiation with the Washington Accord signatory countries' engineering institutions for reciprocal recognition. It will help engineering graduates from Bangladesh to open new horizon be it for further education, employment or migration. Generally an engineering accreditation panel of the professional body consists of professionally renowned academics from other universities, senior practicing engineers from industry (public & private) and some secretarial supports from the professional body [3].

4.4 Teaching & Learning Quality Assurance

4.4.1 Student Evaluation and Feedback

One of the primary tasks of a tertiary institution is to create a learning environment where students, academic and support staff work together to make effective learning outcomes. Proactive communication between students and staff about what makes good teaching and learning is essential to achieving these outcomes. Classroom evaluation has greater psychological effects on students. It allows extracting the best out of the students. Correct classroom evaluation can help the students to find the hidden curriculum (answer-oriented approach to the course); afterwards they can allocate their effort with great efficiency [12]. Teaching & learning evaluation and feedback can be collected using a range of methods (questionnaires and Surveys) including institution approved student course (subject) evaluation surveys, peer reviewing and moderation of student's learning outcomes. They are used to gather student responses to a variety of issues ranging from the effectiveness of a particular lecture to the effectiveness of library and IT provision. Every institution has its own policies on student evaluation and feedback mechanism. For example, in Australia, each university administers at least two standard surveys: Course Experience Survey (CES) for each course or subject by the end of each semester and Program Experience Survey (PES) among the final year students once a year. A standard CES form used by RMIT University is shown in Figure 2. The outcomes of the feedback are used to enhance the quality of teaching and learning, and not to punish any one involved in course delivery. The Australian Federal Government conducts Course Experience Questionnaire (CEQ) among the graduate students after completion of their degrees from the Institution within 6 months. Based on these servery outcomes, Government develops bench marking for the quality of education and allocate some public funds to universities.

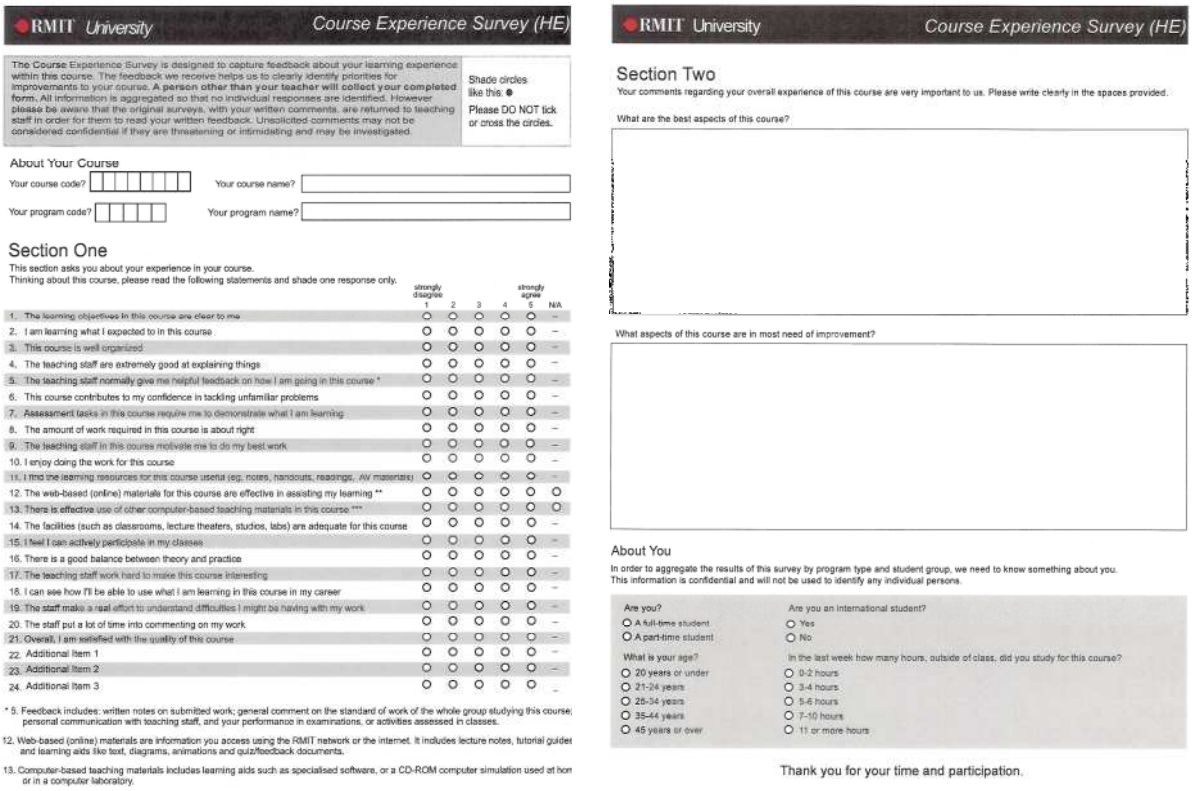

RMIT University — Course Experience Survey (HE)

The Course Experience Survey is designed to capture feedback about your learning experience within this course. The feedback we receive helps us to clearly identify priorities for improvements to your course. **A person other than your teacher will collect your completed form.** All information is aggregated so that no individual responses are identified. However please be aware that the original surveys, with your written comments, are returned to teaching staff in order for them to read your written feedback. Unsolicited comments may not be considered confidential if they are threatening or intimidating and may be investigated.

Shade circles like this: ●
Please DO NOT tick or cross the circles.

About Your Course

Your course code? ☐☐☐☐☐☐☐☐
Your course name? ____________
Your program code? ☐☐☐☐☐
Your program name? ____________

Section One

This section asks you about your experience in your course.
Thinking about this course, please read the following statements and shade one response only.

	strongly disagree 1	2	3	4	strongly agree 5	N/A
1. The learning objectives in this course are clear to me	○	○	○	○	○	–
2. I am learning what I expected to in this course	○	○	○	○	○	–
3. This course is well organized	○	○	○	○	○	–
4. The teaching staff are extremely good at explaining things	○	○	○	○	○	–
5. The teaching staff normally give me helpful feedback on how I am going in this course *	○	○	○	○	○	–
6. This course contributes to my confidence in tackling unfamiliar problems	○	○	○	○	○	–
7. Assessment tasks in this course require me to demonstrate what I am learning	○	○	○	○	○	–
8. The amount of work required in this course is about right	○	○	○	○	○	–
9. The teaching staff in this course motivate me to do my best work	○	○	○	○	○	–
10. I enjoy doing the work for this course	○	○	○	○	○	–
11. I find the learning resources for this course useful (eg. notes, handouts, readings, AV materials)	○	○	○	○	○	–
12. The web-based (online) materials for this course are effective in assisting my learning **	○	○	○	○	○	○
13. There is effective use of other computer-based teaching materials in this course ***	○	○	○	○	○	○
14. The facilities (such as classrooms, lecture theaters, studios, labs) are adequate for this course	○	○	○	○	○	–
15. I feel I can actively participate in my classes	○	○	○	○	○	–
16. There is a good balance between theory and practice	○	○	○	○	○	–
17. The teaching staff work hard to make this course interesting	○	○	○	○	○	–
18. I can see how I'll be able to use what I am learning in this course in my career	○	○	○	○	○	–
19. The staff make a real effort to understand difficulties I might be having with my work	○	○	○	○	○	–
20. The staff put a lot of time into commenting on my work	○	○	○	○	○	–
21. Overall, I am satisfied with the quality of this course	○	○	○	○	○	–
22. Additional Item 1	○	○	○	○	○	–
23. Additional Item 2	○	○	○	○	○	–
24. Additional Item 3	○	○	○	○	○	–

* 5. Feedback includes: written notes on submitted work; general comment on the standard of work of the whole group studying this course; personal communication with teaching staff, and your performance in examinations, or activities assessed in classes.

12. Web-based (online) materials are information you access using the RMIT network or the internet. It includes lecture notes, tutorial guides and learning aids like text, diagrams, animations and quiz/feedback documents.

13. Computer-based teaching materials includes learning aids such as specialised software, or a CD-ROM computer simulation used at hom or in a computer laboratory.

RMIT University — Course Experience Survey (HE)

Section Two

Your comments regarding your overall experience of this course are very important to us. Please write clearly in the spaces provided.

What are the best aspects of this course?

What aspects of this course are in most need of improvement?

About You

In order to aggregate the results of this survey by program type and student group, we need to know something about you.
This information is confidential and will not be used to identify any individual persons.

Are you?
○ A full-time student
○ A part-time student

Are you an international student?
○ Yes
○ No

What is your age?
○ 20 years or under
○ 21-24 years
○ 25-34 years
○ 35-44 years
○ 45 years or over

In the last week how many hours, outside of class, did you study for this course?
○ 0-2 hours
○ 3-4 hours
○ 5-6 hours
○ 7-10 hours
○ 11 or more hours

Thank you for your time and participation.

Figure 2: RMIT Course Experience Survey for Higher Education Form

4.4.2 External Quality Assurance

Each university in Australia needs to undergo education quality scrutiny by the external body such as the Australian Universities Quality Agency (AUQA) which is an independent, not-for-profit national agency that promotes, audits, and reports on quality assurance in Australian higher education. Although it was established by the Ministerial Council on Education, Training and Youth Affairs in 2000, it operates independently of governments and the higher education sector under the direction of a Board of Directors. AUQA is established to be the principal national quality assurance agency in higher education, with responsibility for quality audits of higher education institutions and accreditation authorities, reporting on performance and outcomes, assisting in quality enhancement, advising on quality assurance; and liaising internationally with quality agencies in other jurisdictions, for the benefit of Australian higher education, [13]. Although AUQA ensures the quality of educational programs, it does not accredit any undergraduate programs. University management takes AUQA reports very seriously and tries its best to address any concerns raised by it. It also helps to take adequate preparation for the accreditation of various programs by the professional bodies. A similar independent body can be formed by the Bangladesh government to ensure the quality of education of various programs of all public and private universities.

4.5 Professional Development of Academic Staff and Support Unit

Continuous professional development for academic and support staff is an integral part of quality education. As most engineering academics do not have formal education on teaching methodology, it is essential for academic staff to have in-depth subject matter knowledge, adequate preparation & organisation of the course, effective communication skills, capability of creation of student interest (enthusiasm) for the course, respect for students and conduction of balanced assessment of leaning outcomes. In order to excel in all those, academic staff needs to be continuously involved in scholarship of teaching, scholarship of research and scholarship of administration. Each degree offering department should encourage and provide financial support to individual academic staff for undertaking formal or informal professional development activities. Academic staff should develop and or update the curriculum continuously as new knowledge is pouring and rapid changes in global engineering practices are taken place. New laboratory equipments, learning resources (books, journals articles, conference proceedings, web access to other university resources, computer aided teaching and learning, adequate IT facilities – all are necessary to ensure quality education [1]. Professional development for support staff is also vital as they also contribute to the students learning experience in the educational institution.

5. CONCLUDING REMARKS

The 20-year (2006-2026) strategic plan of the UGC for higher education in the country suggests that at least 28 new universities will be required to establish to absorb around 15% of high school leavers (HSC passed students) for higher education. With an increase number of HSC passed students each year, it is necessary to set up new universities, upgrade existing degree offering colleges/institutions to universities, increase intake numbers of existing universities, allowing more private universities to be established and permitting reputed foreign universities to offer their courses in strategic and technological areas in Bangladesh to accommodate these young minds into the higher education systems.

At the same time importance has to be given for maintaining and upgrading the standard of education in light of work place demands, otherwise the purpose of higher education will not be materialised. Introduction of double shifts and/or evening shift at the public universities and private universities to meet students' demands can be explored.

A centralised undergraduate admission system similar to existing undergraduate medical (MBBS) program admission for all engineering programs offered by all public engineering universities needs to be introduced in order smooth and anxiety free admission for HSC passed school leavers.

Undergraduate program and course curriculum should be revised and updated in light of the industry (work place) needs and all undergraduate programs must be accredited by appropriate professional bodies in order to give graduates global recognition and global employment opportunities.

The location for the establishment of future universities should be selected based on population density and strategic interest of the country. Some specialised undergraduate engineering programs such as automotive engineering, aeronautical/aerospace engineering, mechatronics engineering, oil and gas engineering, and other specialised engineering need to be offered by various universities to prepare graduates for strategic national and global needs. It is Bangladesh's strategic interest to increase the intake numbers for undergraduate textile engineering and leather technology & engineering programs as country's textile, garments and leather product industries have shown promising future.

In addition, an interactive online engineering education system can be developed using BTTB's nation wide IT infrastructure. Libraries of all universities can be connected through high speed Internet connectivity for sharing library resources and other learning materials particularly it is important when limited resources are available in Bangladesh.

REFERENCES

[1] Alam, F., Dilla, E., Subic, A. and Tu, J., A three step teaching and learning method in laboratory experiments for a thermal fluid course, *Journal of Wold Transactions on Engineering and Technology Education*, Vol. 6, No.1 pp13-16, June, 2007

[2] Bourne, J., Harris, D. and Mayadas, F., Online engineering Education: Learning Anywhere, Anytime, *Journal of Engineering Education*, Vol. 94(1), pp 131-146, January, 2005

[3] Becker, F. S., Globalization, curricula reform and the consequences for engineers working in an international company, *European Journal of Engineering Education*, Vol. 31(3), pp 261-272, June, 2006

[4] Patil, A. S., Engineering and technical education in India-current issues and trends, Proceeding *of the first Asia-Pacific Forum on Engineering and Technology Education*, Monash University, Melbourne, Australia, pp172-174, 1997

[5] Patil, A. S., The Development of Engineering and Technical Education in India, *Global Journal of Engineering Education*, Vol. 2, No.3, 1998

[6] Islam, M.T., Current Status and Prospects for E-learning in the promotion of Distance Education in Bangladesh, *Turkish Journal of Distance Education*, Vol. 7, No.1 Article: 10, January, 2006

[7] 13. Roche, E. C. and Dongen, D. B. V., An Industrial Approach to the Unit Operations Laboratory Course, *ASEE Annual Conference & Exposition*, Seattle, 1998

[8] Felder, R. M. and Peretti, S. W., A Learning Theory-based Approach to the Undergraduate Laboratory, *ASEE Annual Conference & Exposition*, Seattle 1998

[9] Coyle, E. J., Jamieson, L. H. and Oakes, W. C., EPICS: Engineering Projects in Community Service, *International Journal of Engineering Education*, Vol 21(1), pp 1-12, 2005.

[10] Engineers Australia - Stage 1 Competencies for Professional Engineers, http://www.ieaust.org.au

[11] RMIT Learning and Teaching Strategy 2007-2010, http://www.rmit.edu.au

[12] Crooks, T. J., The Impact of Classroom Evaluation Practices on Students, *Review of Educational Research*, Vol. 58(4), pp. 438-481, 1988

[13] http://www.auqa.edu.au/ accessed on 22 November 2008

[14] The Bangladesh Today, 2008

[15] Bangladesh Bureau of Educational Information and Statics (BANBIS)

[16] University Grants Commission UGC, Bangladesh, http://www.ugc.gov.bd

[17] Middlehurst, R. and Woodfield, S., The Role of Transnational, Private, and For-Profit Provision in Meeting Global Demand for Tertiary Education: Mapping, Regulation and Impact, a Case Study of Bangladesh, Centre for Policy and Change in Tertiary Education, University of Surrey, UK and Commonwealth of Learning and UNESCO, 2004

[18] Bangladesh Bureau of Statistics (Population Census 2001), http://www.bbs.gov.bd

Proceedings of the 4th BSME-ASME International Conference on Thermal Engineering
27-29 December, 2008, Dhaka, Bangladesh

OFF CAMPUS ENGINEERING EDUCATION

Firoz Alam[1], Aleksandar Subic[1], Gregory Plumb[2], Mark Shortis[2] and Reddy P Chandra[3]

[1]School of Aerospace, Mechanical and Manufacturing Engineering, RMIT University, Melbourne, Australia
[2]Program and Courseware Enhancement, Academic Development Group, RMIT University, Melbourne, Australia
[3]Academic Coordinator, Singapore Institute of Commerce, Singapore
E-mail: firoz.alam@rmit.edu.au

ABSTRACT

In the era of globalisation, traditional on-campus education providers have the opportunity to offer off-campus education to meet student needs. Although a number of many non-engineering programs have been offered off-campus for some time, the engineering program, generally lag behind due to insufficient laboratory and workshop facilities off campus and the difficulties encountered when trying to emulate this learning experience. RMIT University's off-campus mechanical engineering program is designed to overcome these difficulties by combining traditional teaching and learning with flexible learning modes. The program represents a hybrid approach and has drawn significant interest among educational developers and professional bodies.

Key words: *Off campus education, mechanical engineering, residential visit, mixed mode*

1. INTRODUCTION

Engineering education is an organised set of activities that implement learning accomplishments for individual students to perform creative engineering tasks and solve real-world engineering problems. Off-campus engineering education is an organised effort to realise engineering learning using remote delivery. This effectively removes time and place constraints from education thus enhancing lifelong learning by creating professional capabilities. Today, computer-based information systems have altered the meaning of traditional communication and coordination, making global opportunities possible and global competition inevitable – all of these have significant impact on the delivery of education. In today's rapidly changing world educational institutions are forced by financial, social and moral needs to embrace these changes, especially in delivering traditional on-campus education, [3, 4, 5, 6, 7]. As a result, many engineering education institutions are delivering off-campus education, including engineering programs [1]. However, most online programs in engineering are currently offered at postgraduate level as working engineers find it difficult to access campus based learning. Also, postgraduate programs (such as Masters' programs) require relatively less contact hours and laboratory work [4]. On the other hand, any traditional undergraduate engineering (B.Eng) requires more than four times contact hours and significant laboratory facilities. Distance learning, where the total learning package can be taken remotely from the education provider – often in a self-paced form - is more common for social science and general science education. It is relatively difficult to provide engineering education in this form, especially mechanical engineering education as engineering education is predominantly science and mathematics based and the courses are relatively difficult to offer online due to the need for hands on laboratory work and more elaborate connection between theory and practice. Traditionally, engineering needs hands-on laboratory, workshop, learning activities in order to achieve the desired learning outcomes, [8, 9]. Industry and research organizations wish to have work-ready graduates with hands-on practical and theoretical knowledge who are ready for immediate work assignment often without even induction training. Engineering educators have vast responsibilities to educate and train the undergraduate student with hands-on knowledge, especially when fewer students come to the university with experience of so called shade tree mechanics or amateur radio operators as hands on laboratories are the only means to provide students the look and feel of physical systems or to develop a feel for engineering [10, 12, 13, 14].

The School of Aerospace, Mechanical and Manufacturing Engineering, RMIT University has developed a unique hybrid model of off-campus delivery of the Mechanical Engineering Bachelor degree program with a view to overcoming the difficulties traditionally experienced. Many students in South East Asia and South Asia, after completion of their Polytechnic Diploma (or equivalent Advanced Diploma) in engineering, have entered the work force as many of them are the “sole earners” in the family. Many of them do not have the opportunity to advance their formal education further due to work commitments and lack of articulation pathways to higher education in those parts of the world. However, if an articulation pathway is offered, such students can pursue their higher education primarily on a part-time basis. In order to assist such students in this region and expand the reach of its programs, the School has started an off-shore Bachelor of Engineering (Mechanical) program in Singapore in collaboration with a local education provider. The effective learning outcomes of on-shore and off-shore Bachelor of Mechanical Engineering programs are the same as within a specific discipline or specialisation, and all graduates receive the same award regardless of the geographic location of the campus or the mode of delivery. Receipt of the same award requires that the graduate outcomes of the program, the capabilities of the graduates, and the quality of the curriculum are all identical.

2. OFF-CAMPUS PROGRAM DELIVERY AND COMPARISON WITH ON CAMPUS MODE

On-shore delivery of mechanical engineering program is primarily based on face-to-face contact between teaching staff and students in classes, supported to some extent by online (web based) and Internet resources (as well as the University Library and other facilities). Lectures, tutorials and practice classes are the primary mechanisms for student learning. Online materials are an enhancement that provides students with flexibility in accessing the learning materials. The off-shore delivery of the mechanical engineering program reverses this emphasis, with the online learning guides (curriculum materials), Internet resources and text books acting as the primary mechanism of student learning. Students are expected to spend a significant amount of time devoted to self-directed learning, and consequently need a broader range of learning support mechanisms.

The off-shore engineering program, although delivered in a different mode, must achieve equivalent learning outcomes and graduate attributes as the on-shore program. This is achieved by introducing a flexible learning model characterised by a wide range of interactions between staff and students, and between students themselves. For example, the program involves:

- Regular tutorials (3 hours per week throughout the academic semester) and consultations conducted by local staff at the local partner’s premises;

- Pre-examination workshops conducted by RMIT staff at the local centre;
- Online classrooms for each course with a range of communication options including discussion boards, email, video conferences;
- Residential visits, laboratory experimentation and various technical workshops on-campus at RMIT in Australia.

A more detailed overview of the particular elements encompassed by this integrated approach to off-shore education is shown in Figure 1.

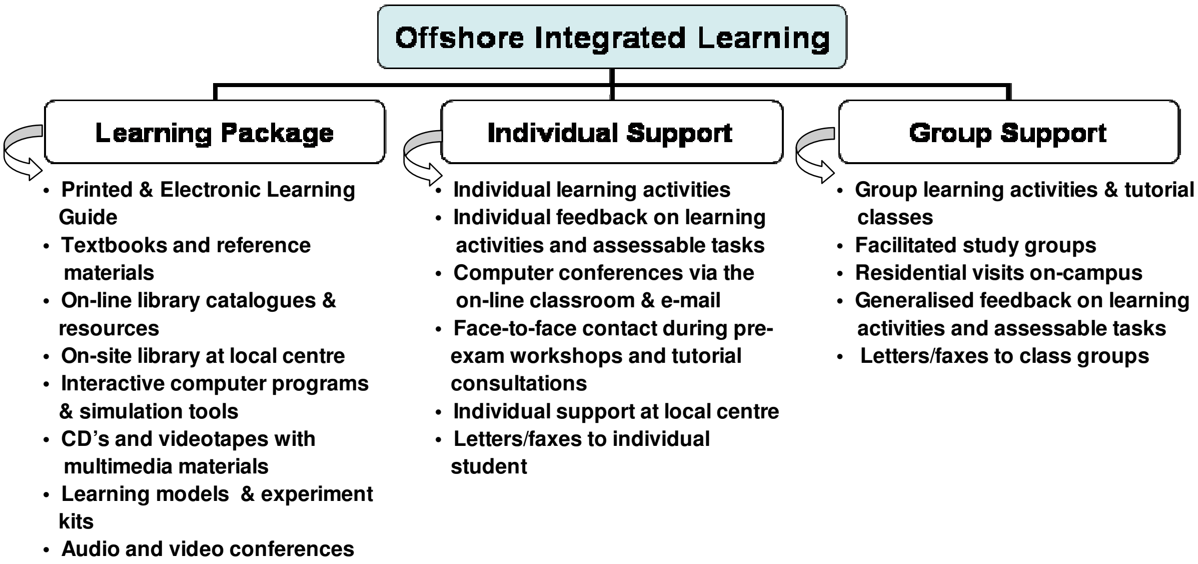

Figure 1: Some aspects of off-shore learning program (adapted from [11, 15])

The implementation of the program is collaborative and integrated, involving a community of learning comprising online education, students, local and RMIT staff, and the RMIT learning support staff in the Program and Courseware Enhancement group. The learning is facilitated through a full partnership of all stakeholders [15]. This model emphasises the importance of student groups through group-based learning activities such as projects (many of them industry based), workshops, field visits, presentations and study groups. This, together with the provision of a wide range of support mechanisms and interactions, aims to avoid some of the pitfalls of more conventional distance education programs, which frequently isolate the student resulting in the loss of motivation and loss of feeling of belonging to the program and the university [15]. The implementation model and approaches described here require academic staff to be committed to online education and to understand the underpinning teaching and learning processes. The off-shore students have shown a strong commitment to learning, resulting in academically excellent performance. The community-of-learning concept that is deliberately nurtured in the program has enabled a more fundamental transformation of how both staff and students perceive online education [15]. As mentioned earlier, students need to attend at least 3 hours face-to-face tutorial classes per week for each subject during the semester with local tutors. The tutors are well trained and supported by the respective RMIT academics (course coordinators/lecturers). Apart from face to-face tutorial classes, the RMIT course academics conduct pre-examination workshops minimum of 8 hours for each course by visiting the off-shore campus where students are located at least two weeks before the examination where respective lecturers go through theoretical concepts and application of these concepts in real world engineering applications.

2.1 Special Requirements on Students

The majority of the requirements on students are imposed by the student selection and entry process. There are four key issues:

- Prior learning;
- Class scheduling;
- Two residential visits (to Australia);
- Fees that generally differ from on-campus students.

All off-shore students are required to have a Polytechnic Diploma and/or equivalent recognised qualification so that they can articulate into the third year equivalent level of the Bachelor of Engineering (Mechanical) program with three second-year level courses. As most students are generally employed full time, all classes are scheduled on week-day evenings to allow students to attend without unduly interfering with their employment. For the same reasons, pre-examination workshops are generally held on weekends and examinations are scheduled for week-day evenings or weekends. All hands-on laboratory work has been done during the two residential visits to the School of Aerospace, Mechanical and Manufacturing Engineering, RMIT University Bundoora East Campus, Australia.

2.2. Home Campus Visit

The off-shore Mechanical Engineering program offered by RMIT University requires two residential visits for students to Australia during their course of study. During the visits students are required to complete:

- A series of laboratory experiments using some ‘state-of-the-art’ RMIT University experimental facilities;
- Special technical workshops;
- Library workshops;
- Industry visits.

These visits are essential as many of these components cannot be provided by the local education provider. The home campus visits and laboratory work are of paramount importance. Students feel that they belong to RMIT University student’s community.

2.3 Professional Practice Exposure

On-shore students have exposure to guest lectures, industry visits, simulated environments within online courseware and industry-sponsored, or guided, major projects in the final year of their program. On the other hand, almost all off-shore students are engaged in full- or part-time employment within the industry and thereby have continual exposure to professional practice and the industrial environment. Additionally, most final-year projects are industry-based, real-world engineering problems.

2.4 Design Skills and Project Work

As previously mentioned, students of the off-shore mechanical engineering program are in full-time employment and are continuously exposed to real-life design work where they need to apply problem- solving skills and communication skills through team work or their individual capacity, and apply high standards of engineering ethics. The RMIT off-shore program provides students technical competency whereas the ongoing job provides professional practice. All off-shore students take their final year projects with day-to-day activities in engineering practice. Each project is coordinated, supported and supervised by at least three supervisors at RMIT University, at the local partner's campus and at their place of employment. In some cases, where the supervisor at the place of employment does not want to be officially a supervisor due to cultural constraints, two supervisors look after the project work and provide advice and guidance to students.

2.5 Retention and Completion

The retention rate for the off-shore mechanical engineering program is much higher than the on-shore program. Although no formal study was conducted on this matter, it is believed that the higher retention rate is primarily due to 100% employment, secured career progression (after graduation) and social and professional status as well as financial commitments. The students' enrolment and retention rates since 2002 are shown in Table 1. Although the highest enrolment was in 2002 and the number gradually decreases till 2006 this was primarily due to local partners' financial difficulties. However, since 2007, the enrolment number is gradually increasing to 90 in 2008 and is expected to be over 100 in 2009. The students' commitment is reflected in their assessments. A high proportion of students obtain degrees with various honours levels.

Table 1: Off-shore program students' enrolment history for B.Eng-Mechanical, [2]

Offshore Program in Singapore	**Student Enrolments History** (Students)							**Retention** (% continuing)					
BEng (Mech)	2002	2003	2004	2005	2006	2007	2008	2002	2003	2004	2005	2006	2007
	105	77	69	60	33	42	90	95	95	95	95	95	95

Offshore Program in Singapore	**Students in Full- or Part-Time Employment (%)**						**Degree Completions** (Graduates)					
	2002	2003	2004	2005	2006	2007	2002	2003	2004	2005	2006	2007
B Eng (Mech)	100	100	100	100	100	100	56	28	13	14	8	15

2.6 Quality Assurance and Students Feedback

Students' learning achievements are continually assessed through a combination of written assignments, presentations, projects, laboratory work, examinations and final-year theses. The standards required of these assessment components are the same as those for RMIT Mechanical Engineering on-campus students. The student experiences in the Mechanical Engineering program are evaluated regularly through student-staff consultative committee meetings, an online feedback system, program audits and through end-of-semester surveys using the expanded Program/Course Experience Questionnaire (CEQ), which is currently used in its standard form by all Australian universities for benchmarking purposes. While student assessment of the program quality is quite high it is also interesting to learn how students perceive quality and what they find most satisfying in the program. When asked what they found most satisfying in the program most of the surveyed students indicated:

- Residential visits and laboratory workshops on-campus at RMIT;
- Interactions with, and support of, the academic staff;
- Interactions with their peers;
- Challenging project work.

Clearly, students find the wide range of interactions and associated social experiences most rewarding in this program. They also appreciate the challenges associated with experiential problem-based and project-based learning, which are of key importance to achieving equivalency with the on-campus program. Student feedback is documented in the program log. Actions arising from these feedback mechanisms are being attended to as quickly as possible and outcomes are reported accordingly.

3. CONCLUSION

The off campus mechanical engineering education was facilitated by the development of flexible learning guides and resources for core engineering courses. These are applicable for off-campus or on-campus teaching and learning. Where necessary, the learning materials are customised to best address the needs of the different cohorts of students. Additionally, the curriculum has been internationalised through this delivery experience. The off campus mechanical engineering has been accredited by the Institution of Engineers, Australia (IEAust) through vigorous auditing and quality assurance processes and onsite visits by the IEAust accreditation panel. The innovative off-campus mechanical engineering program delivery method ushers in internationalisation of engineering education especially in South East Asia. The program confirms the commitment to hands on laboratory works for undergraduate engineering students by integrating residential visits in the mode of delivery. Residential visits enable laboratory exercises to be done and also give students exposure to industrial environments as well as opportunities for attending various technical workshops on home campus. The program allows students to continue working while pursuing their studies. This model of program delivery can easily be replicated anywhere in the world. The off-campus delivery of the program has enabled teaching student to further build their educational capabilities by exposing them to new technologies and opportunities.

REFERENCES

[1] Alam, F., Dilla, E., Subic, A. and Tu, J., "A three step teaching and learning method in laboratory experiments for a thermal fluid course", *Journal of World Transactions on Engineering and Technology Education*, Vol. 6, No. 1, pp 13-16, June, 2007

[2] Alam, F., "*Students progress map for Off-shore programs*", School of Aerospace, Mechanical and Manufacturing Engineering, RMIT University, Melbourne, Australia, 2008

[3] Becker, F. S., "Globalization, curricula reform and the consequences for engineers working in an international company", *European Journal of Engineering Education*, Vol. 31 (3), pp 261-272, June, 2006

[4] Bourne, J., Harris, D. and Mayadas, F., "Online Engineering Education: Learning Anywhere, Anytime", *Journal of Engineering Education*, Vol. 94 (1), pp 131-146, January, 2005

[5] Condit, P. and Pipes, R. B., "The global university, improving engineering education for the 21st century", *Issues in Science and Technology,* Vol.14, No. 1, pp 27, 1997

[6] Downey, G. L., Lucena, J. C., Moskal, B. M., Parkhurst, R., Bigley, T., Hays, C., Jesiek, B. K., Kelly, L., Miller, J., Ruff, S., Lehr, J. L. and Nichols-Belo, A., "The globally competent engineer: working effectively with people who define problems differently", *Journal of Engineering Education*, Vol. 95, No. 2, pp 107-122, 2004

[7] Fiedler, K. D.; Deans, C.; Loch, K. D. and Palvia, P., C., "Response to the mandate for the internationalization of information systems education", *Proceedings of the 27th Annual Meeting of the Decision Sciences Institute,* V 2, Decis Sci Inst Atlanta GA, USA, pp 672, 1996

[8] Feisel, L. D. and Rosa, A. J., "The Role of the Laboratory in Undergraduate Engineering Education", *Journal of Engineering Education*, Vol. 94 (1), pp 121-130, January, 2005

[9] Gillett, D., Latchman, H. A., Saltsman, C. and Crisalle, O., "Hands-on Laboratory Experiments in Flexible and Distance Learning", *Journal of Engineering Education*, Vol. 90, No. 2, pp 187-191, 2001.

[10] Moore, D. J. and Voltmer, R. R., "Curriculum for an Engineering Renaissance", *IEEF Transaction on Education*, Vol. 46 (4), pp. 452-455, 2003

[11] *Offshore Engineering Program Accreditation Report*, SET Portfolio, RMIT University, Melbourne, Australia, 2006

[12] Rover, D. T., "The Academic Bookshelf- Closing the Distance", *Journal of Engineering Education*, vol. 95 (2), pp 175-176, April, 2008

[13] Rover, D. T., "The Academic Bookshelf- Engineering Education in a Global Context", *Journal of Engineering Education*, vol. 97 (1), pp 105-108, January, 2008

[14] Ross, S. and Scanlon, E., *"Open Science: The Distance Teaching and Open Learning of Science Subjects"*, Paul Chapman Publishing, 1995

[15] Subic, A. and Maconachie, D., "Flexible learning technologies and distance education: a teaching and learning perspective", *European Journal of Engineering Education*, Vol. 29 (1), pp 27-40, March, 2004

Proceedings of the 4th BSME-ASME International Conference on Thermal Engineering
27-29 December, 2008, Dhaka, Bangladesh

VIBRATION EFFECTS OF GOODS TRAINS ON THEIR FREIGHT

Firoz Alam[1] and Randall Cape[2]

[1]School of Aerospace, Mechanical and Manufacturing Engineering, RMIT University, Melbourne, Australia
[2]Distribution Solutions, Melbourne, Australia

E-mail: firoz.alam@rmit.edu.au

ABSTRACT

Low frequency vibration generated by the freight train can make significant damage to freight goods. These low frequency vibrations are all but impossible to attenuate. Therefore, goods specific vibration damping device is an alternative to reduce the damage. A custom made airbag with variable air pressure was developed and evaluated for its effectiveness on the reduction of low frequency vibration magnitude. The results indicated that the custom made airbag with differential air pressure is capable of reduction in low frequency vibration induced damage and can be used for a range of freight goods that are susceptible to low frequency vibration.

Key words: *Vibration, low frequency, goods train, freight, wooden pallet.*

1. INTRODUCTION

A lion's share of goods has been transported over the land by freight trains around the world including over the vast land in Australia. Some freight are subjected to damages caused by the low frequency vibration generated by the impact of steel wheels on the rails, the gap between the wheel flanges and rails, and the geometry of the rail truck. Additionally, the combined effects of the elasticity of the rail, surface roughness and discontinuities at the rail joints can also cause the vibration both in horizontal and vertical directions, [1-5]. It is difficult to control these low frequency vibrations as the centre of gravity of a typical rail carriage is located high above the spring suspension. The natural frequency of a suspension system of a rail carriage largely depends on the type of spring and the mass of the rail carriage. The natural frequency of the rail carriage body on the main springs usually ranges between 1 to 4 Hz. Therefore, it is virtually impossible to use isolators with a lower frequency than the natural frequency of the main spring system. It is very unlikely that isolators can provide significant protection to payloads (freight goods/equipment) with respect to overall motion of the vehicle body. It may be noted that a typical range of natural frequency of the suspension system in the vertical direction of a rail carriage is between 2.5 to 7.5 Hz. Meanwhile, the natural frequency of the un-sprung weight (also called “wheel hop” frequency) is usually in between 10 and 20 Hz. In short, as mentioned earlier, it is not feasible to design isolators to have natural frequencies substantially lower than the natural frequency of the un-sprung weight unless isolators do not alleviate vibration from this source. A problem associated the application of isolators is to avoid resonance with this source of vibration. It is not easy to estimate the optimum magnitude of friction damping as it depends on the weight of the carriage and the nature of the excitation (eg, the vibration resulting from irregularities in the rails). As the mass of the rail carriage increases, the natural frequency decreases, thus, the nature of the vibration of the carriage (car body) varies with load. This effect is best evaluated experimentally. Generally with train speeds both lateral and vertical vibration magnitudes are increased. As most freight carried by the rail carriage are not isolated from these low frequency lateral, vertical and their combined vibrations, a significant damage is occurred during the transportation process.

In order to identify the main excitation frequency of train carriage vibration under a range of operating speeds, the Pacific National, one of the largest rail carriage operators in Australia has conducted a series of experimental measurements of rail carriage vibration on tracks in between Whyalla and Pt Augusta; and Crystal Brook and Coonamia sections of southern and south-eastern Australian rail corridor. The measurements included both vertical and lateral motions at 80, 90, 100, 120 and 130 km/h for Whyalla and Pt Augusta section and 100, 110, 120 and 130 km/h for Crystal Brook and Coonamia section. An average of 80 seconds time domain data was recorded using accelerometers. The results from the measured data showed that the maximum vibration energy was located at low frequencies (approximately 2 Hz) for the lateral motion. However, for the vertical motion, the dominant frequencies were 10 to 20 Hz (see Table 1).

Table 1: High Frequency and Magnitude for Vibration in Lateral and Vertical Directions

Highest Peak	**Magnitude/Freq** g	**Car Type**
Lateral	0.8 (3 Hz)	Stucki RB 14
	0.2 (15-25 Hz)	Miner 4500
	4 (2 Hz)	RQCY 65
	8 (2 Hz)	RQKY 2760
	0.6 (2 Hz)	RQKY 2345
Vertical	0.8 (10 Hz)	Stucki RB 14
	8.8 (20 Hz)	Miner 4500
	2 (9 Hz)	RQCY 65
	1.3 (15 Hz)	RQKY 2760
	0.6 (5 Hz)	RQKY 2345

It is believed that the above mentioned low frequency excitations were the primary cause of damages to some fragile and delicate freight such as wine bottles during the shipments by train carriage from Melbourne to other major cities around Australia. Wine bottles are generally stacked together on a wooden pallet. A wooden pallet can hold up to 1000 bottles in several layers and each layer is separated by a high density fibre board (also called Masonite sheet, see Figures 2 and 3). The Masonite sheet is made of compressed wood dust and /or recycled paper. AMCOR, ACI Freight Company and Distribution Solutions have been primarily involved in transportation of glass wine bottles from Melbourne to various wineries in Adelaide, Perth and Sydney by freight trains, trucks and ships. During the shipment of bottles by freight trains from Melbourne to Adelaide (828 km) and Adelaide to Perth (2659 km), the glass bottles have been subjected to low frequency lateral and vertical vibration of the rail carriage (2 Hz to 20 Hz). As a result of this induced vibration, scalping occurs between the bottle opening and the underside of Masonite sheet by generating the dust powder. The penetration of dust powder into the bottles makes them unsuitable for the wine bottling (use). The damage has been causing significant financial losses to these aforementioned transport companies.

In order to understand how low frequency excitation (vibration) can cause scalping of a Masonite sheet in laboratory environments, the primary objective of this study was to design a series of test to simulate vertical, horizontal and transverse vibration caused by a rail carriage that are generally experienced by the bottles during the shipment by freight rails. A pallet of bottles with several layers was put on a vibration bench that can generate a range of frequency with different magnitudes. The test was conducted at the Army Engineering Laboratory with excitation frequency of 1 Hz to 100 Hz. The test showed that low excitation frequency (ranging from 2 Hz to 26 Hz) can cause the instability of the wooden pallet and ultimately causing the damage to the bottles. The test also revealed that the most excitation (vibration) energy was located at 3, 26 and 70 Hz for vertical motion. However, the highest vibrational energy was found to be at 15 Hz for the combined motions in the transverse and longitudinal directions.

Identifying the possible excitation frequencies that might cause damage to the glass bottles, several options were explored including the use of mechanical spring, air spring (air cushion/pillow) and rubber spring. Each of these types of spring has relative advantages and disadvantages. However, a custom made air spring (air bag) with variable air pressure was thought to be more appropriate for the wooden pallet as it could be easily inflated and fitted under the wooden pallet with out creating any obstacle for the forklift operator during the loading and unloading of wooden pallet (see Figures 1 & 2).

2. DESIGN OF AIRBAG

In order to measure the vibrational damping characteristics of the air spring, a custom made air pillow was designed and constructed. Each wooden pallet was fitted with two air bags underneath of the wooden pallet approximately 800 mm apart as shown in Figure 1.

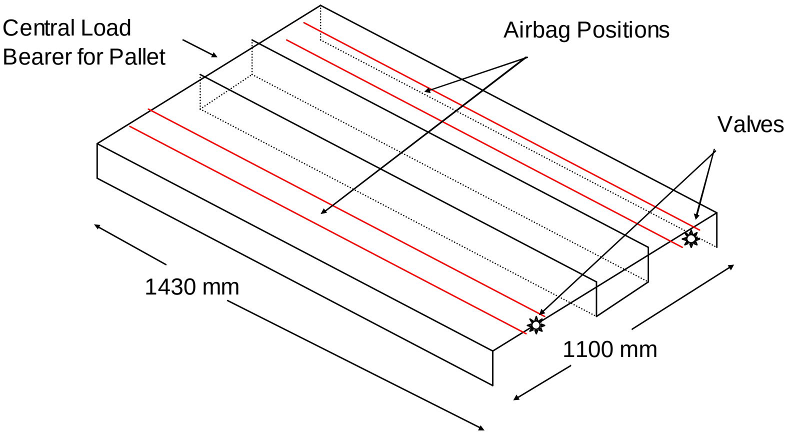

Figure 1: Schematic of airbag and wooden pallet

Figure 2: A typical wooden pallet

In order to determine the effectiveness of airbag with variable pressures under a range of loading conditions and excitation frequencies of rail carriage during motion, a series of test has been conducted at the Army Engineering Laboratory Workshop in Melbourne as it is only facility equipped with the state-of-the-art instrumented vibration test rig as required for this study. In order to make sure that there was no pressure drop from the pressurised airbag made for the palette platform, static load tests were conducted. The pressurised airbag was observed for 72 hours for any possible air leak. It was decided to test the airbag with maximum load of 1000 kg (to simulate the real loads with two pallets: one on the top of the other) for 72 hours at 4 bar (58 psi) pressure. However, static test was conducted at pressure close to 60 psi (little over 4 bars). Tests were done with maximum pressure under maximum loads with anticipation that if there was no pressure drop at a high pressure under maximum loads, then there would be less likelihood to have pressure drop due to air leak at a lower pressure under smaller load.

Vibration tests were conducted at four input frequencies (10, 20, 50 and 80 Hz) at acceleration level of 0.25 g, 0.50 g and 1 g. Tests below 10 Hz was attempted but without success due to excessive magnitude of vibration as pallets were displaced from the platform. No measurements were taken at higher "g" as it is not the continuous case and also the instrument limitation at the Army Engineering Laboratory Workshop. The tests were done at 3 pressure levels (max 60 psi, median 40 psi and minimum 25 psi) with 1 pallet and 2 pallets (one on the top of other). The minimum pressure was determined under maximum loads (two pallets) in such a way that under any circumstances the floating metallic plate could not touch the bracket of airbag through which static load transferred to the mounting floor. At least 5 mm gap was kept. The whole measurement process was completed with careful visual inspection. The experimental set up along with pallets and accelerometers are shown in Figures 3 to 8.


Figure 3: Two Pallets on Test Rig


Figure 4: Input Floor with Accelerometers

a) Air Bag Set Up

b) Support Mounting with Input Floor

Figure 5: Air Bag and Floor Mounting

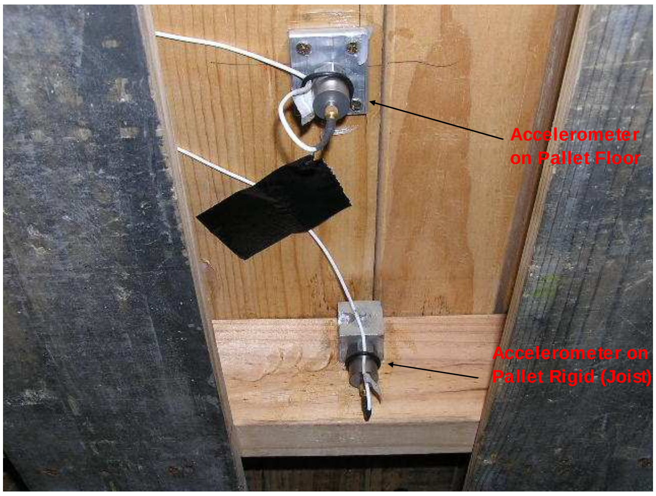

Figure 6: Accelerometers on Wooden Floor above the Metallic Floor on Air Bag

Figure 7: Experimental Set Up

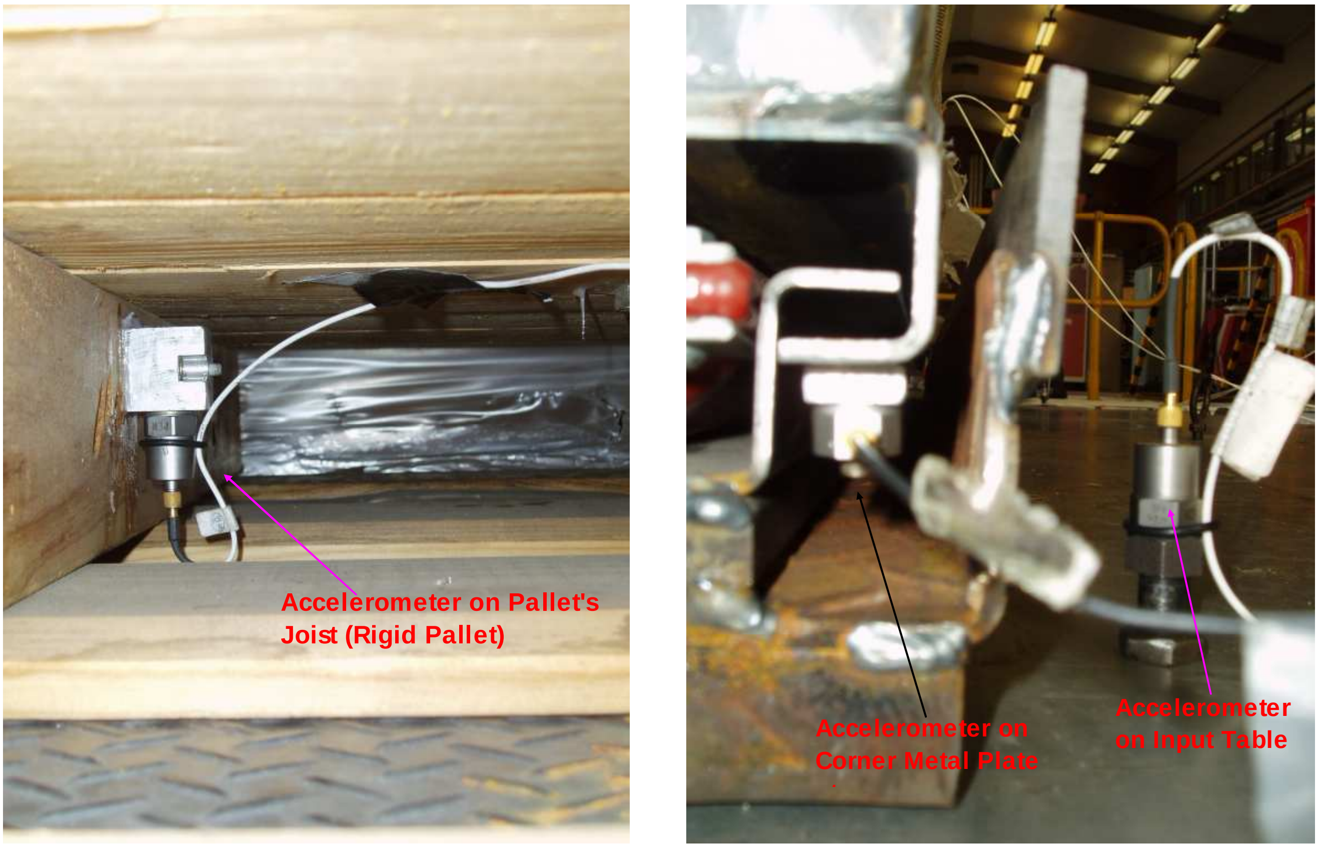

a) Accelerometer on Pallet Ribs (Floor)

b) Accelerometer on Metal Plate on Air Bag

Figure 8: Location of accelerometers

3. RESULTS AND DISCUSSION

The output accelerations as a function of frequencies (10, 20, 50 & 80 Hz) of pallet floor, rigid pallet and metal plate on corner are shown in Figures 9 to 11. The output acceleration plots under 60, 40 and 25 psi pressures along with the static load of 1000 kg are shown on the left hand side of each figure. Similarly, plots under the static load of 500 kg (one pallet) are shown in the hight hand side of each figure.

The magnitude of the output acceleration reduces significantly at all frequencies under the static load of 1000 kg (two pallets), see Figures 9 and 10. However, a relatively less reduction of 1 g acceleration magnitude was noted at 10 Hz. A desirable reduction was achieved under the static load of 500 kg (one pallet) at lower air pressure (below 40 psi). The reduction was not significant at 60 psi pressure at 10 Hz. However, the reduction of magnitude was notable at higher frequencies (above 10 Hz). The output acceleration trends are similar for both locations mentioned earlier (pallet floor and rigid pallet), which were located approximately at the centre of the bottom pallet. The acceleration outputs from the accelerometer located on the corner of the metal plate were from one location only, which might not reflect the average response of the bottom pallet. The output plots for this location indicate that the magnitude initially reduces and then increases at frequencies 50 Hz and over under the static loads of 1000 kg and 500 kg. However, the variation is significant at lesser static load (eg, 500 kg), see Figure 11.

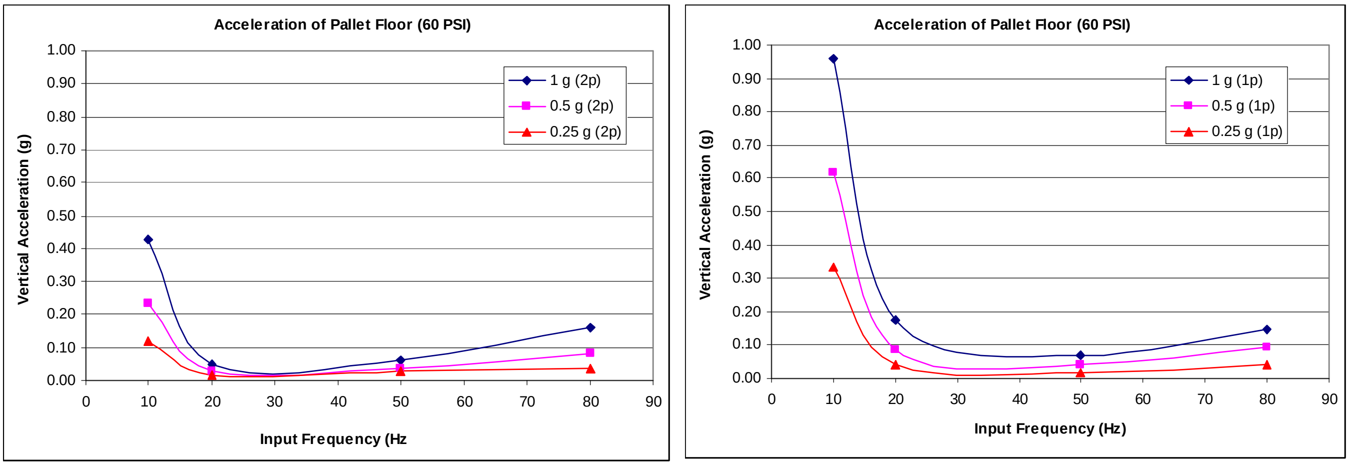

a) Pressure 60 PSI and Two Pallets

b) Pressure 60 PSI and Single Pallet

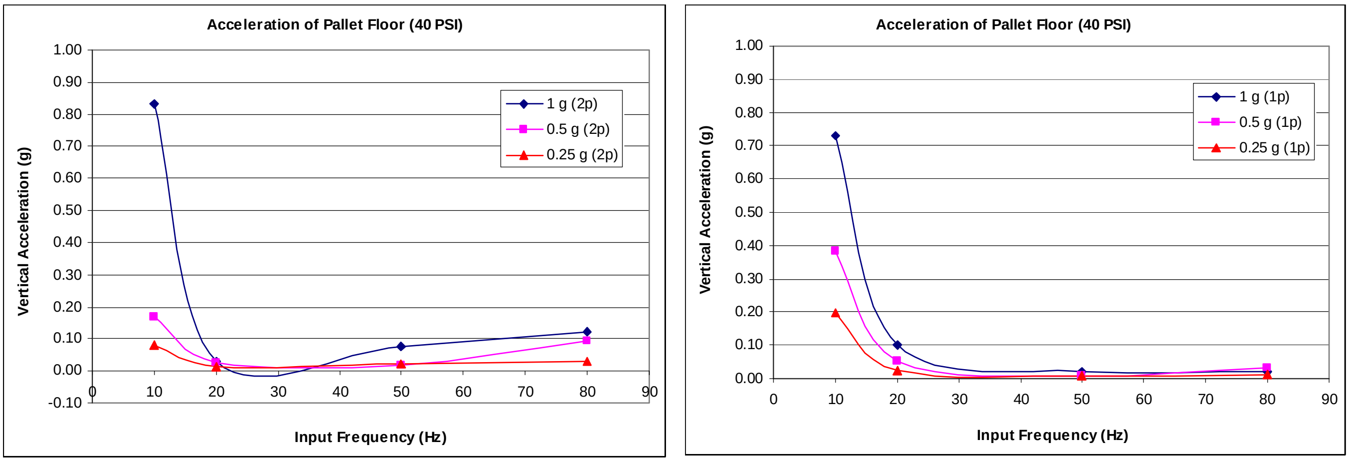

c) Pressure 40 PSI and Two Pallets

d) Pressure 40 PSI and Single Pallet

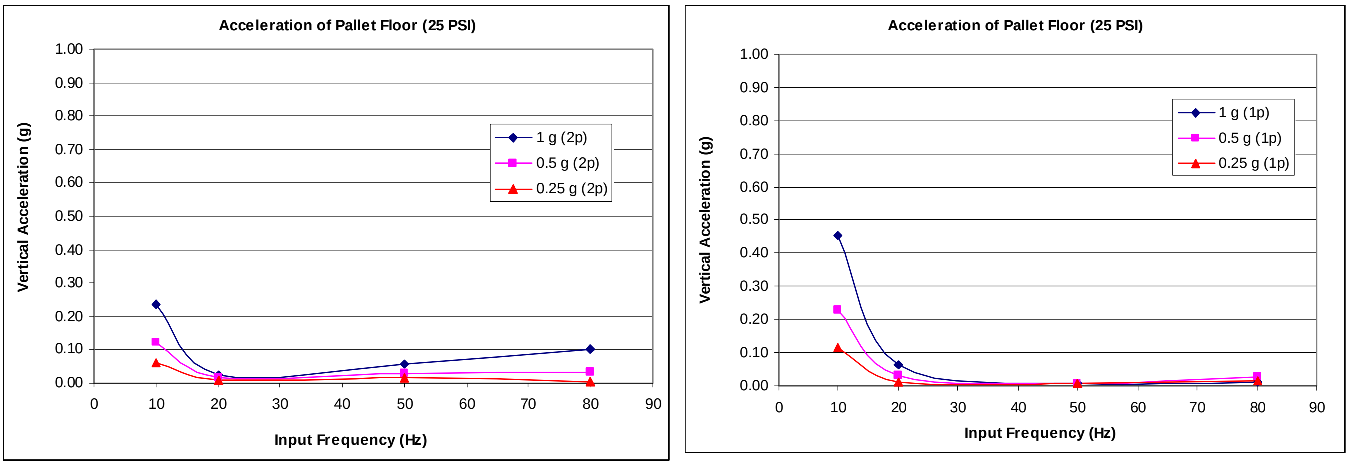

e) Pressure 25 PSI and Two Pallets

f) Pressure 25 PSI and Single Pallet

Figure 9: Pallet Floor Vertical Acceleration Variation with Frequencies and Pressure

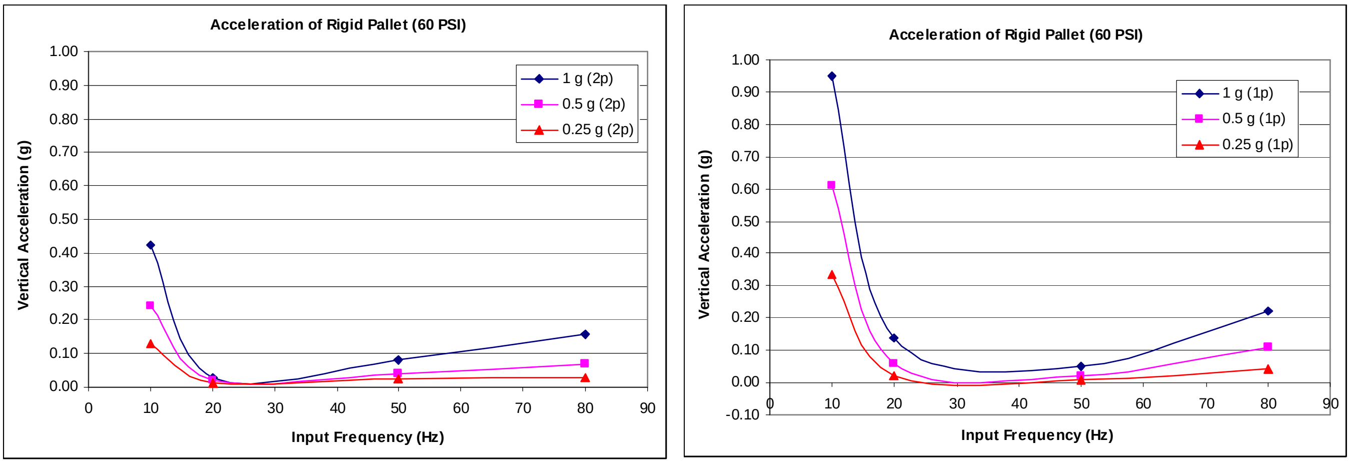

a) Pressure 60 PSI and Two Pallets

b) Pressure 60 PSI and Single Pallet

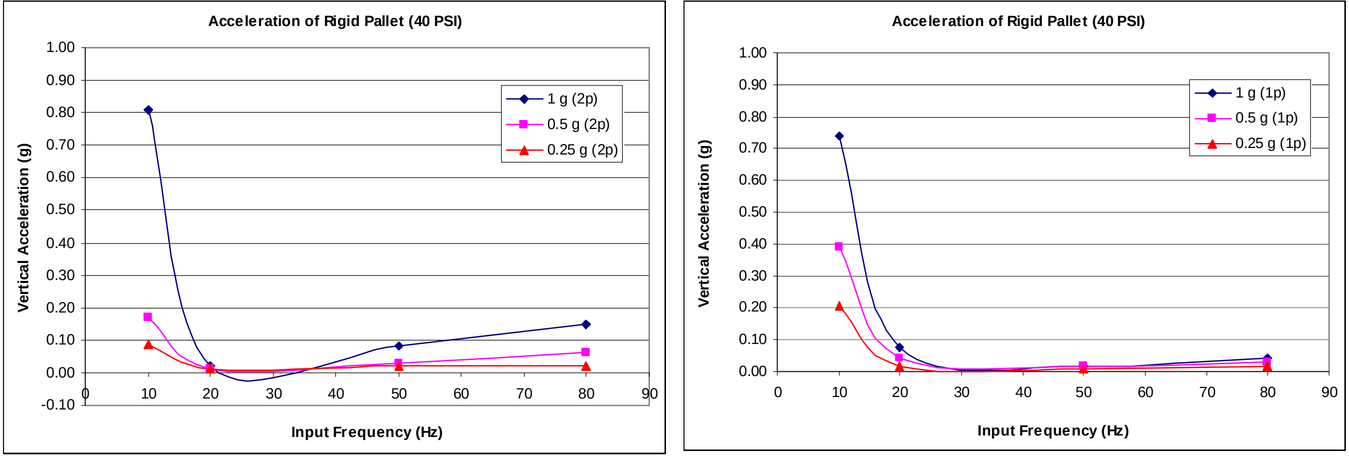

c) Pressure 40 PSI and Two Pallets

d) Pressure 40 PSI and Single Pallet

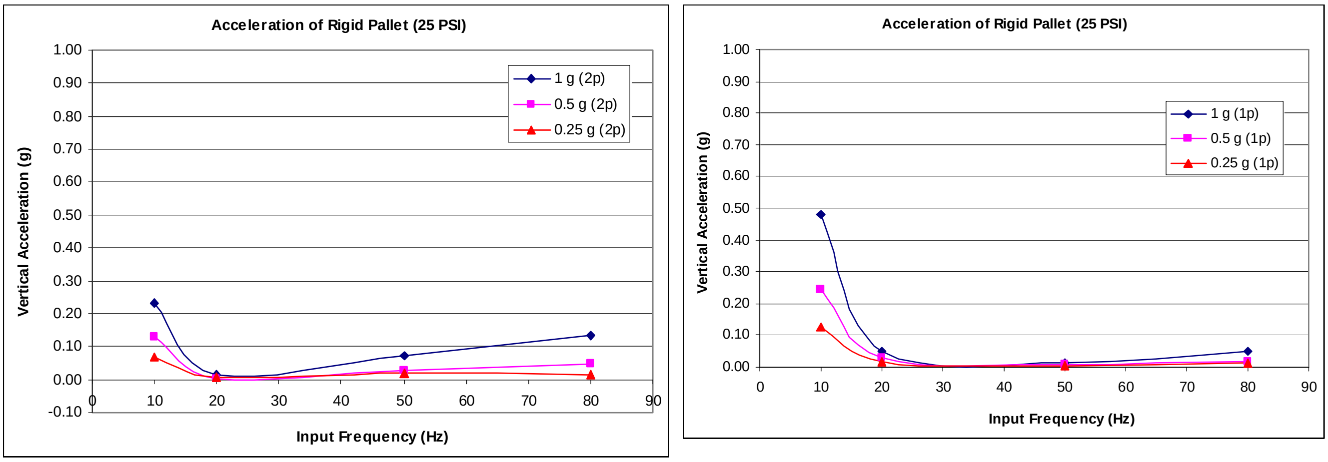

e) Pressure 25 PSI and Two Pallets

f) Pressure 25 PSI and Single Pallet

Figure 10: Rigid Pallet Vertical Acceleration Variation with Frequencies and Pressure

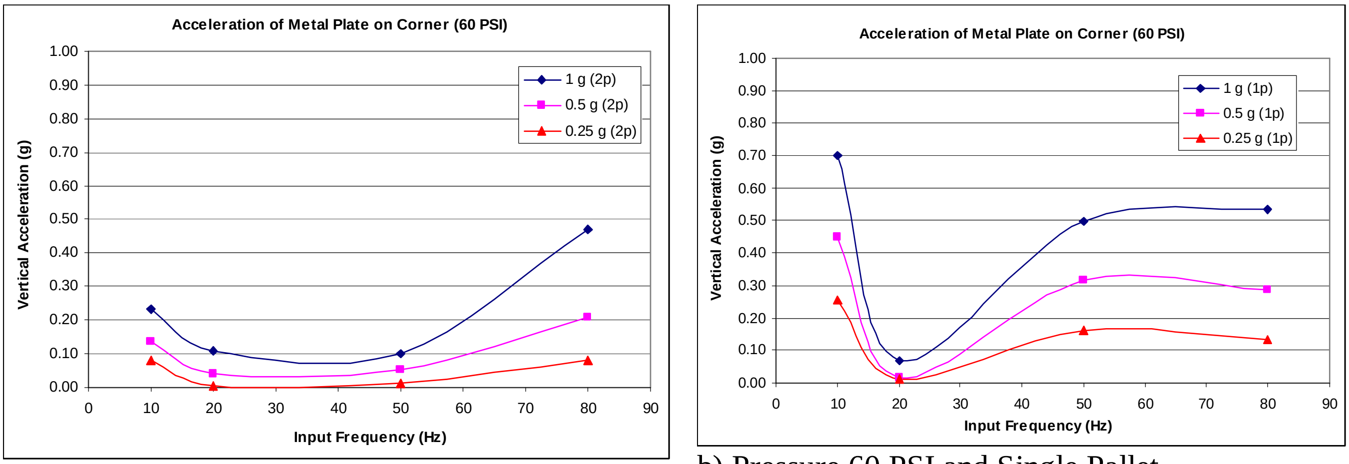

a) Pressure 60 PSI and Two Pallets

b) Pressure 60 PSI and Single Pallet

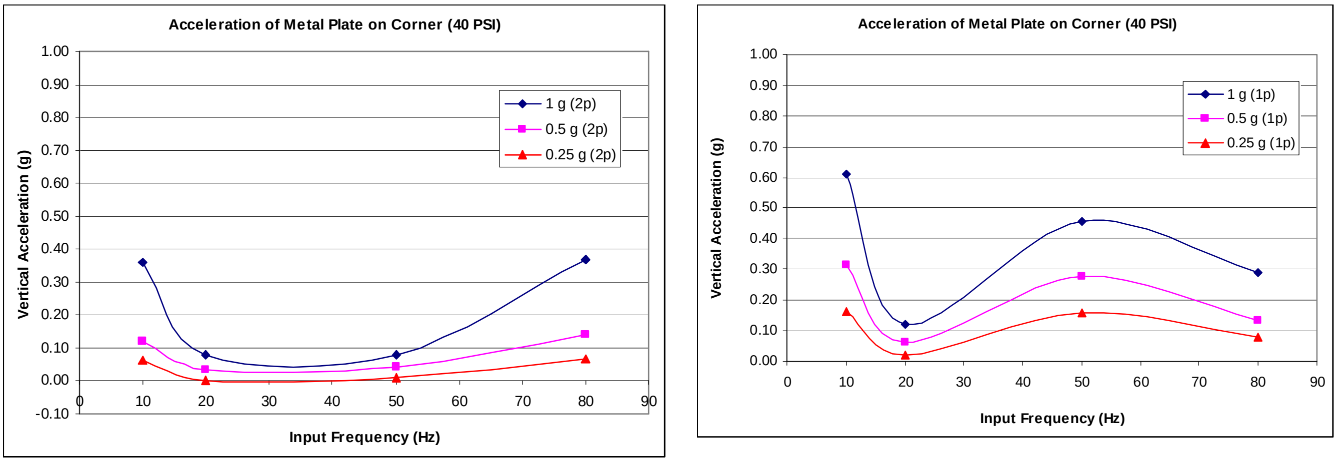

c) Pressure 40 PSI and Two Pallets

d) Pressure 40 PSI and Single Pallet

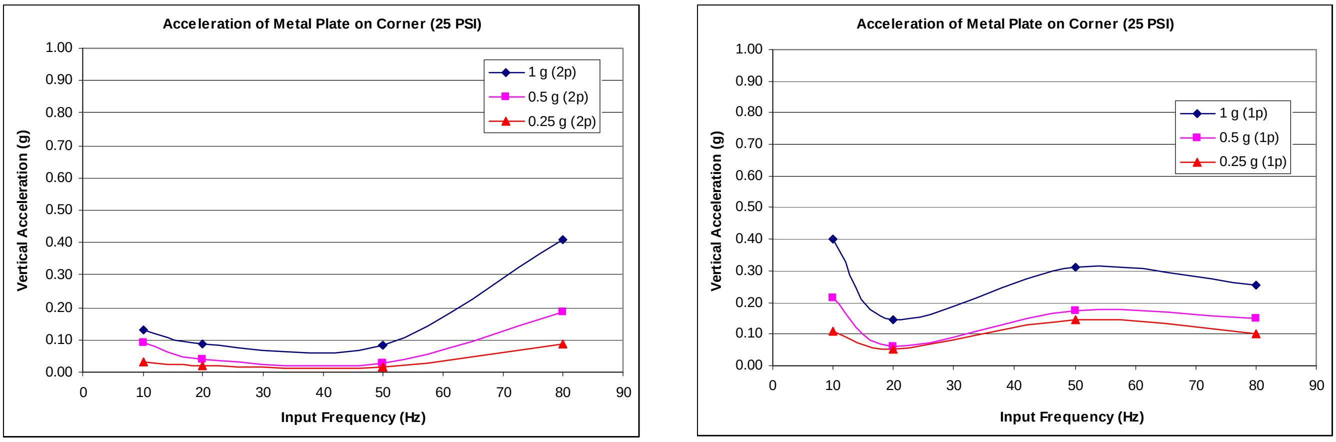

e) Pressure 25 PSI and Two Pallets f) Pressure 25 PSI and Single Pallet

Figure 11: Metal Plate on Corner, Vertical Acceleration Variation with Frequencies and Pressure

4. CONCLUSIONS

The following conclusions are made from the experimental investigations conducted in this work:

- Under the maximum static load, the air bag is effective at frequencies between 20 and 80 Hz under all acceleration modes (0.25 g, 0.5 g and 1 g). However, the attenuation of acceleration magnitude is relatively small at 10 Hz for 1 g acceleration mode only.
- Under the minimum static load, the lowest airbag pressure (25 psi) is more effective at all frequencies under all acceleration modes, except some minor variations at 10 Hz for all acceleration modes. At 10 Hz, the attenuation is not effective at high pressure (60 psi) for all acceleration modes.
- Twenty five to thirty psi pressure for the airbag is effective for the two pallets configurations and 20 to 25 psi is believed to be the effective pressure for one pallet configuration

ACKNOWLEDGEMENTS

The authors would like to express their sincere thanks to Mr Brett Oldfield of Army Engineering Laboratory Workshop, Mr David Pearce of Industrial Conveying Australia Pty Ltd, National Pacific Rail, and ACI Logistics for the assistance with the testing, data processing and the airbag design.

REFERENCES

[1] Ahmed, A.K.W., “Ground transportation systems”, *Encyclopaedia of Vibration*, pp 603-620, 2004
[2] Alam, F., “Report of vibration effects on wooden pallets”, ACI logistics, Melbourne, Australia, 2 April, 2004
[3] Dinwoodie, J., “Rail freight and sustainable urban distribution: Potential and practice”, *Journal of Transport Geography*, Vol 14 (4), pp 309-320, July 2006
[4] Lee, S.Y. and Cheng, Y. C, “Influences of the vertical and the roll motions of frames on the hunting stability of trucks moving on curved tracks”, *Journal of Sound and Vibration*, Vol 294 (3), pp 441-453, June 2006
[5] Haris, C. M. and Crede, C. E. (editors), *Shock and Vibration Handbook* (in three volumes), McGraw Hill, New York, 1961

Proceedings of the 4th BSME-ASME International Conference on Thermal Engineering
27-29 December, 2008, Dhaka, Bangladesh

MATHEMATICAL MODELING OF TEMPERATURE DURING LASER FORMING USING BIMODAL BEAM

Masoud Sistaninia and Mohammad Haghpanahi

Department of Mechanical Engineering
Iran University of Science and Technology
Tehran, Iran

E-mail: m_sistani@mechEng.iust.ac.ir

ABSTRACT

An analytical and numerical solution is developed for a transient heat conduction equation in which a plane slab is heated by a bimodal distribution beam over the upper surface. In laser heat treatment of steel few methods use to produce a wider and nearly uniform average irradiance profile. This may be achieved by a bimodal (TEM_{11}) shaped laser beam. In this paper, the mentioned 3-D models are used to model the thermal field of laser forming with bimodal beam distribution. The ANSYS code was used for finite element modeling. The results show that bimodal beam is useful for obtaining a uniform heat intensity distribution.

Keywords: *Thermal modeling, laser forming, finite element, bimodal beam*

1. INTRODUCTION

Laser forming is a novel technique, where a laser beam causes thermal expansion locally, and deformation is achieved by scanning the laser beam across one side of the material. In laser heat treatment of steel bimodal distribution beam (Figure 1) is used to produce a wider and nearly uniform average irradiance profile. The temperature gradients that are developed through the material induce distortion because the temperature changes with thickness and thus causes different expansion of adjoining layers. Laser forming is currently used because of its technical benefits why it does not require external forces and thus reduces cost and increases flexibility. In past years, considerable attention has been paid to the comprehending the laser forming mechanisms and the investigation of the effects of laser forming parameters on the deformed shape and on the mechanical properties of the formed parts [1-3]. In the recent years, considerable research has been done on computer modeling of the laser forming process of plates [3-6].

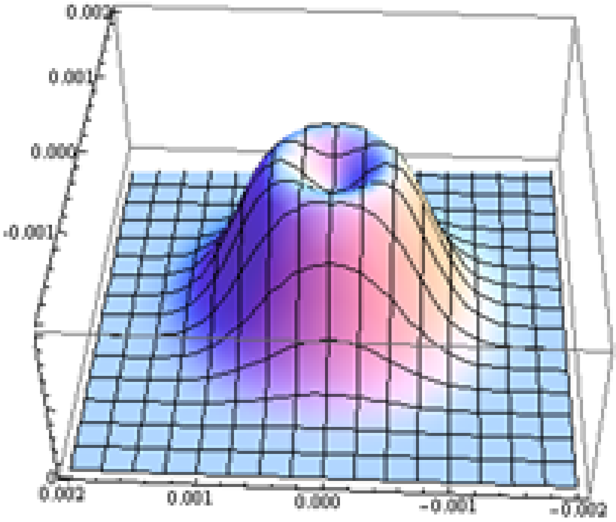

Figure1: Schematic of bimodal distribution beam

2. ANALITICAL MODEL

An analytical model, based on the renowned transient heat conduction equation, was used to establish the temperature rise as a function of time and step *T(r,t)* in the material under the action of a laser beam:

$$\frac{1}{\alpha}\frac{\partial T}{\partial t}-\nabla^2 T=\frac{f(r,t)}{K} \qquad (1)$$

where $\alpha = K/\rho\, c_p$ is the thermal diffusivity (ρ the density, K thermal conductivity and c_p specific heat) of the material. The internal heat generation term *f(r,t)*, at the right side of Eq. (1), is identified as the energy distribution of the laser beam.

In the case of three-dimensional transient, nonhomogeneous heat conduction problem given by equation (1), the solution for T(r,t) is expressed in terms of the three-dimensional Green's function [7].

$$T(\mathbf{r},t)=\frac{\alpha}{K}\int_{\tau=0}^{t}d\tau\int_R G(\mathbf{r},t\,|\,\mathbf{r}',\tau)\,f(\mathbf{r}',\tau)dv'+\int_R G(\mathbf{r},t\,|\,\mathbf{r}',\tau)\,|_{\tau=0}\;F(\mathbf{r}')dv' \qquad (2)$$

where $F(\mathbf{r}')$ is the initial temperature distribution.

The three-dimensional Green's function can be obtained from the product of the three one-dimensional Green's function in rectangular coordinates:

$$G(x,y,z,t\,|\,x',y',z',\tau)\;=\;G1(x,t\,|\,x',\tau)\;.\;G2(y,t\,|\,y',\tau)\;.\;G3(z,t\,|\,z',\tau) \qquad (3)$$

where each of the one-dimensional Green's functions $G1$, $G2$ and $G3$ depends on the extent of the region (i.e. , finite, semi infinite, or infinite) and the boundary conditions. The one-dimensional infinite medium Green's function is obtained as [7]:

$$G(x,t\,|\,x',\tau)=\left[4\pi\alpha(t-\tau)\right]^{-1/2}\mathbf{exp}\left(-\frac{(x-x')^2}{4\alpha(t-\tau)}\right) \qquad (4)$$

and the semi infinite medium Green's function when the boundary at z=0 is of the second kind (insulate) is obtained as [7]:

$$G(z,t\mid z',\tau)=\left[4\pi\alpha(t-\tau)\right]^{-1/2}.\left[\mathbf{exp}\left(-\frac{(z-z')^2}{4\alpha(t-\tau)}\right)+\mathbf{exp}\left(-\frac{(z+z')^2}{4\alpha(t-\tau)}\right)\right] \tag{5}$$

Substituting $G1(x,t\mid x',\tau)$, $G2(y,t\mid y',\tau)$ and $G3(z,t\mid z',\tau)$, in Eq. (3) yields the three-dimensional Green's function, for $z^{'}=0$'

$$G(x,y,z,t\mid x^{'},y^{'},z^{'}=0,\tau)=2\left[4\pi\alpha(t-\tau)\right]^{-3/2}\times\mathbf{exp}\left(-\frac{(x-x^{'})^2+(y-y^{'})^2+z^2}{4\alpha(t-\tau)}\right) \tag{6}$$

Substituting $x^{'}=x-r\cos\theta$, $y^{'}=y-r\sin\theta$ and $G(\mathbf{r},t\mid\mathbf{r}',\tau)$ from Eq. (6) in Eq. (2) the temperature distribution is obtained as:

$$T(x,y,z,t)=T_O+\frac{\alpha}{K}\int_0^t\int_{-\pi}^{\pi}\int_0^{\infty}f\,(x-r\cos\theta,y-r\sin\theta,\tau)\times 2[4\pi\alpha(t-\tau)]^{-3/2}.\mathbf{exp}\left(-\frac{r^2+z^2}{4\alpha(t-\tau)}\right).r\mathrm{d}r\mathrm{d}\theta\mathrm{d}\tau \tag{7}$$

If a piece of finite depth, *L*, is considered the three-dimensional Green's function for a slab with finite depth becomes:

$$G(x,y,z,t\mid x^{'},y^{'},z^{'}=0,\tau)=\left[4\pi\alpha(t-\tau)\right]^{-1}\times\mathbf{exp}\left(-\frac{(x-x^{'})^2+(y-y^{'})^2}{4\alpha(t-\tau)}\right)$$

$$\times\left(\frac{1}{L}+\frac{2}{L}\sum_{n=1}^{\infty}e^{-\alpha(\frac{n\pi}{L})^2(t-\tau)}\cos(\frac{n\pi}{L}z)\right) \tag{8}$$

and from Eq. (2) with the substitution $x^{'}=x-r\cos\theta$, $y^{'}=y-r\sin\theta$, the temperature distribution for a piece of finite depth, *L*, can be expanded as:

$$T(x,y,z,t)=T_O+\frac{\alpha}{K}\int_0^t\int_{-\pi}^{\pi}\int_0^{\infty}f\,(x-r\cos\theta,y-r\sin\theta,\tau)\times[4\pi\alpha(t-\tau)]^{-1}.\mathbf{exp}\left(-\frac{r^2}{4\alpha(t-\tau)}\right)$$

$$\times\left(\frac{1}{L}+\frac{2}{L}\sum_{n=1}^{\infty}e^{-\alpha(\frac{n\pi}{L})^2(t-\tau)}\cos(\frac{n\pi}{L}z)\right)rdrd\theta d\tau \tag{9}$$

In this equation, or in equation (7), $f(x\text{-}r\cos\theta,y\text{-}r\sin\theta,\tau)$ is the heat intensity distribution.

For a bimodal distribution on a circular disc heat source; the heat release intensity *q(r)* is a function of *r*. The bimodal distribution which the distance from the center of the distribution curve to one of its peaks on the r_i-axis is 0.24 r_o can be expressed by the following equation,

$$q(r)=4.3677\frac{Q}{\pi r_o^2}[e^{-(3.947(r/r_o)-0.947)^2}+e^{-(3.947(r/r_o)+0.947)^2}] \tag{10}$$

So, for bimodal distribution that moves along a straight line the function *f(x-rcosθ, y-rsinθ, τ)* takes the form,

f(x-rcosθ, y-rsinθ, τ)=

$$4.3677\frac{Q}{\pi {r_o}^2}\left[e^{-\left(\frac{3.947\sqrt{(x-r\cos\theta-v\tau)^2+(y-r\sin\theta)^2}}{r_o}-0.947\right)^2}+e^{-\left(\frac{3.947\sqrt{(x-r\cos\theta-v\tau)^2+(y-r\sin\theta)^2}}{r_o}+0.947\right)^2} \right] \qquad (11)$$

3. FINITE ELEMENT MODEL

The basic heat-transfer equation considered is:

$$\mathrm{F} = \nabla(-KT) \qquad (12a)$$

Which relates the heat flux **F** to thermal gradient

$$\nabla(K\nabla T)-\rho c_p\frac{\partial T}{\partial t}=-G \qquad (12b)$$

This equation applies to unsteady-state heat conduction, where again ρ is the density, c_p the specific heat, T the temperature, t the time , K the thermal conductivity and G the internal generation of heat. G is zero where the incident laser power is modeled as a heat flux.

In this model the time during which the laser beam continuous irradiation is divided to n increments Δt, and during each increment Δt, it can be assumed that the laser beam doesn't move. The program determines the thermal load for each node on the heated surface which depends on the laser beam position, heat intensity distribution and the node position. Laser beam position depends on its moving path, speed and time thus the value of load for every node on the heated surface is a function of time and place.

In each increment an implicit 3-D finite element model is used to compute the solution of the heat transfer equation (12), and consequently the results of each increment becomes the initial condition of the next time increment. For small Δt, one can assume that the laser moves continuously. The flow chart of the finite element simulation is shown in Figure 2.

In this model, it is necessary to make a decision about the element size and shape, time increment and number of step n^* for each increment with the help of the analytical model. Since these quantities are not independent, the following relation can be written:

$$\begin{cases} F_o = \dfrac{\Delta x^2}{\alpha\Delta t^*} \\ \Delta t^* = \dfrac{\Delta t}{n^*} \end{cases} \qquad (13)$$

The Fourier number F_o, which includes material thermo-diffused efficiency α, time step Δt* and node spacing Δx should be below 2. For small time increment every load step can be solved by one substep ($n^*=1$ or $\Delta t=\Delta t^*$).

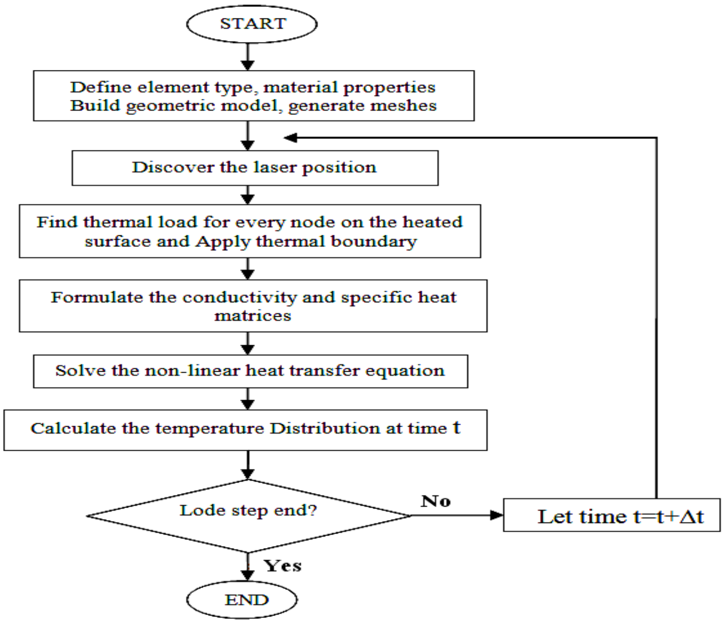

Figure 2: Flow chart of thermal modeling during laser hardening using a finite element method

4. RESULTS AND DISCUSSION

The 3-D models developed, is exemplified in the investigation of the laser forming of a stainless steel plate (AISI 304L). A slab of 30 × 30 mm and 4 mm thickness was used for the investigation. A summary of the processing parameters which are used in this investigation is given in Table 1. The material was assumed to be homogenous and isotropic. The ambient temperature was set at 25 ^{o}C.

Table 1: Laser forming parameters

Laser power, q (w)	278
Beam diameter, d (mm)	4
Scan speed (mm.sec^{-1})	30
Absorptivity	0.72
Thermal conductivity, k (Wm^{-1} K^{-1})	20
Heat capacity c (J kg^{-1} K^{-1})	552
Thermal diffusivity α (m^{2} s^{-1})	4.61e-6

Figure 4 shows a comparison between analytical result and FEM results for different mesh size. This Figure shows the temperature history of a point on the heated surface at x=3.1mm, y=0.48mm during laser forming with a bimodal beam. In this comparison the model has been discretized by cubic elements, in order to improve efficiency and reduce calculation dense meshes are used around the heated region. Mesh 1 relates to a meshing which the distance between nodes on the heated surface and around the heated region is 0.25 mm. This mesh under the laser is such that it has sufficient number of elements to capture the inflection of the bimodal distribution (Figure 3). The number of elements for this mesh is 84906. As it is obvious for this case we found a good agreement between FEM result and analytical result. Mesh 2 relates to a meshing which the distance between nodes on the heated surface and around the heated region is 0.5 mm and 8 elements were used along the z-direction (in thickness direction) and mesh 3 relates to a meshing which the distance between nodes on the heated surface and around the heated region again is 0.5 mm but 4 elements used along the z-direction (in thickness direction).

The mesh 1 is in a good agreement with the analytical model although there is few difference between the analytical and numerical model but if the number of the meshes increase the error dose not decrease considerably and the time of solve increase drastically.

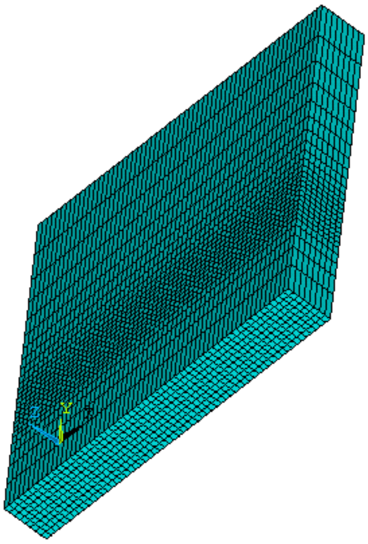

Figure 3: The 3D model that has been discretized by cubic elements

Figure 5 shows the temperature change with time at various points on the heated surface for the bimodal beam mode. This Figure shows the maximum temperature occurs on the center line and as the distance increase from the center line the temperature falls precipitously.

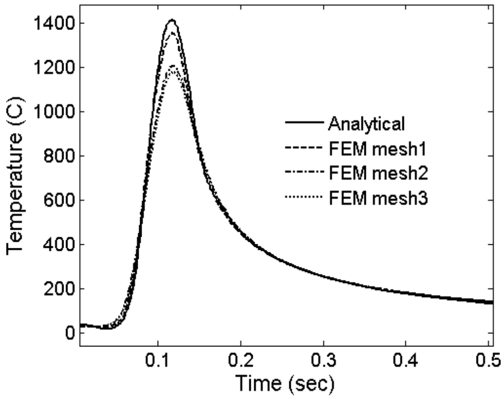

Figure 4: Comparison of 3-D finite element model and analytical model results for laser forming with bimodal distribution

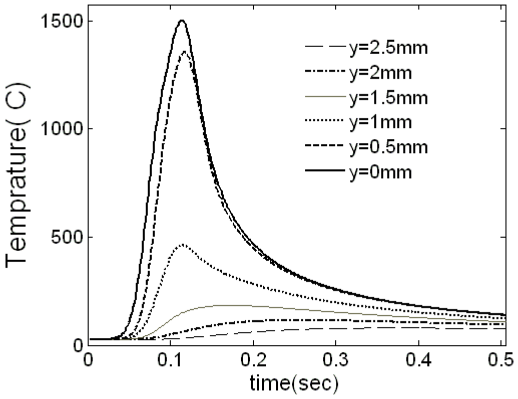

Figure 5: Temperature history at various points on the heated surface

5. CONCLUSIONS

The thermal fields in laser forming with bimodal beam were modeled. Green function method has been employed to derive an analytical solution and also a FEM model has been developed to simulate the body temperature. The FEM results are in reasonable agreement with analytical results. The results can be used to design a laser forming process using bimodal heat distributions. The result can be also used for prediction of process parameters.

REFERENCES

[1] Vollertsen, F., "Mechanism and Models for Laser Forming," Proceedings of LANE'94, Section B, 1, Meisenbach Bamberg, Germany, pp 345-360, 1994

[2] Holzer, S., Arnet, H. and Geiger, M., "Extending Laser Bending for the Generation of Convex Shapes," Proceedings of LANE'94, Section B, 1, Meisenbach Bamberg, Germany, pp. 379-386, 1994

[3] Yongjun Shi, Zhenqiang Yao, Hong Shen, Jun Hu, Research on the mechanisms of laser forming for the metal plate, Int. Journal of Machine Tools & Manufacture 46, pp 1689–1697, 2006

[4] Zhenqiang Yao, Hong Shen , Yongjun Shi, Jun Hu, Numerical study on laser forming of metal plates with pre-loads, Computational Materials Science 40, pp 27–32, 2007

[5] Hong Shen, Yongjun Shi, Zhenqiang Yao, Numerical simulation of the laser forming of plates using two simultaneous scans, Computational Materials Science 37, pp 239–245, 2006

[6] F.R. Liu, K.C. Chan, C.Y. Tang, Numerical simulation of laser forming of aluminum matrix composites with different volume fractions of reinforcement, Materials Science and Engineering A 458, pp 48–57, 2007

[7] Andrei D. Polyanin, Handbook of linear partial differential equations for engineers and scientists, 2002

[8] R. Komanduri, Z.B.Hou, Thermal analysis of laser surface transformation hardening-optimization of process parameters, Int. J. of Machine tools and Manufacturing 44, pp 991-1008, 2004

Proceedings of the 4th BSME-ASME International Conference on Thermal Engineering
27-29 December, 2008, Dhaka, Bangladesh

AIR BUBBLE TRAJECTORIES IN POLYMERIC SOLUTION AND CRYSTAL SUSPENSION

N. M. S. Hassan[1], M. M. K. Khan[2] and M. G. Rasul[2]

[1]Process Engineering & Light Metals (PELM) Centre
Faculty of Sciences, Engineering and Health
Central Queensland University, Rockhampton, QLD 4702, AUSTRALIA

[2]College of Engineering and Built Environment
Faculty of Sciences, Engineering and Health
Central Queensland University, Rockhampton, QLD 4702, AUSTRALIA

E-mail: n.hassan@cqu.edu.au

ABSTRACT

The experimental results of bubble trajectory in xanthan gum solution, xanthan gum crystal suspension and water are presented in this paper. The suspension was made of 0.05% concentration of xanthan gum solution with 1% (by weight) of 0.23 mm polystyrene crystal particle. The characteristic of the air bubble trajectory in these three different liquids is analysed. The influences of the Reynolds number and the Weber number on bubble trajectory are discussed. The results show that the smaller bubbles (0.1mL) experienced more horizontal movement in water than in other two liquids. On the other hand, larger bubbles (>5mL) produced less spiral motion in water than in other liquids. Conversely, the smaller bubbles (0.1mL) followed least horizontal motion and larger bubbles (>5mL) produced more spiral motion for crystal suspension. Path instability occurred at the bubbles of 2mL and 5mL and they induced both zigzag and spiral trajectory for all liquids. At low Re and We, smaller bubble produced a zigzag trajectory while larger bubbles (> 5mL) showed a spiral trajectory at high Re and We.

Key words: *Bubble trajectory, crystal suspension, path instability, zigzag motion, spiral motion*

1. INTRODUCTION

The characteristics of the bubble motion in a gas-liquid system are an important topic due to its vast engineering applications in many process industries. The bubble path instability is one of the most alluring and least understood aspects of bubble dynamics [1]. Usually, the dynamics of bubble rise are complex problem and the extent of the complexity increases with bubble size [2]. A bubble attempts to follow the path of least resistance during its movement. As a bubble ascends through liquid, the most resistance will be imposed directly on top. However, if the bubble moves slightly to one side, less total resistance is experienced. In most cases, bubbles follow a zigzag, or spiral motion when they rise in a column of liquids.

In most reported studies, very small bubbles rise through water retaining their spherical shape and their trajectory follow a straight line until it finishes its journey.

Significant deformations are observed for bubbles with diameter larger than 1 mm [3]. Aybers and Tapucu [4] have reported different types of trajectories such as zigzag, helical or spiral and rocking motions. Haberman and Morton [5] also observed rectilinear ($Re < 300$), spiral and rocking motions. They indicated that the spiral path could be either clockwise or counter-clockwise, depending on the conditions of bubble release. The major axis of the bubble was always directed perpendicular to the direction of motion. Yoshida and Manasseh [6] discussed the trajectory of the larger bubble consisting of primary and secondary structures. Primary structure was defined as the sideway oscillation within the spiral part of the trajectory when bubble was released with greatest kinetic energy. The secondary structure was the particular shape of the trajectory which is a single path up to a critical height, and here bubble splits into a several intertwined spirals. The critical height may occur when the bubble attains a special shape at terminal velocity.

Many researchers have investigated experimentally the path instability of the bubbles. Path instability takes place when a bubble follows both zigzag and spiral trajectory during its rise rather than following only either zigzag or spiral motion. Path instability usually occurred in the intermediate range of bubble size where bubbles were mostly ellipsoidal [4, 5, 7]. The paths of larger bubbles were not stable and started to zigzag while much larger bubbles followed a spiral motion. Spherical and spherical cap bubbles do not exhibit path instability [7, 8]. Wu and Gharib [9] studied the bubble trajectories for spherical and ellipsoidal bubbles in clean water and they showed that the ellipsoidal bubbles exhibited a spiralling path instability, while the spherical bubbles followed a zigzagging path instability when the bubble diameter exceeded $0.15\,\text{cm}$. Saffman [10] observed only the zigzag motions as the bubble rises in water when the radius of the bubble was less than 1 mm but bubbles of larger radius showed either zigzag or spiral motion. Feng and Leal [11] demonstrated various possible trajectories for different shape regimes. A single bubble can pursue a zigzag path at $Re \approx 600$, accompanied with vortex shedding behind the bubble. Under the same experimental conditions, Yoshida and Manasseh [6] reported that the bubbles can also pursue a spiral trajectory without vortex shedding.

Shew and Pinton [12] described that the initiation of path instability for smaller bubble size changed remarkably in the case of polymer solutions and it also appeared that the split to path instability for increasing bubble size was less rapid for the polymer solution in comparison with water. Tsuge and Hibino [13] reported that the trajectories of rising spherical and ellipsoidal gas bubbles at higher Reynolds numbers are identical.

The trajectories of bubbles were strongly dominated by the bubble deformations and the surrounding liquid flow [3]. Bubble deformations and liquid flow could be explained with two independent dimensional groups such as the Reynolds Number (Re) and the Weber number (We). Generally Re controls the liquid flow regime around the bubble and We characterises the bubble deformations. Therefore, the influences of Re and We are the important aspects for elucidation of the bubble trajectories.

A review of the literature indicates several studies on the behaviour of the bubble rise trajectory in water. However, there are no studies available on the bubble trajectory in non-Newtonian crystal suspensions. The main focus of this study is to explore the characteristic of the bubble trajectory in non-Newtonian crystal suspensions and to compare these results with water and 0.05% xanthan gum solutions.

2. EXPERIMENTAL SET-UP AND PROCEDURE

The experimental apparatus is shown schematically in fig. 1. The details of the experimental apparatus and the experimental methods were described elsewhere [14, 15].

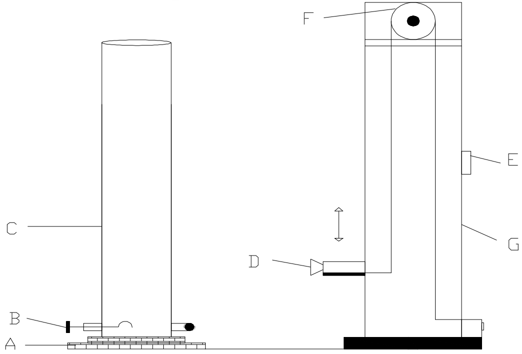

A = Sturdy Base; B = Rotating Spoon; C = Cylindrical test rig (0.125m or 0.40 m diameter), D = Video camera; E = Variable speed motor; F = Pulley; and G = Camera lifting apparatus.

Figure 1: Schematic diagram of experimental apparatus

Trajectory was determined from the still images collected from the digital video camera. Bubble trajectory was analysed from the still frames obtained from the video image. The still frames were then opened in commercial software, “SigmaScan Pro” which revealed the pixel location of an image. The pixel coordinates (X and Y) of the bubbles centre were noted and recorded into spreadsheet. X coordinate corresponds to the distance from the left edge and Y coordinate corresponds to the distance from the top edge respectively. The pixel line running through the centre of the bubble release point was known. The deviation of the bubble centre from the release point was computed by subtracting the X of the bubble centre from the X of the bubble release point.

3. MATERIALS

Water, 0.05% xanthan gun with water and 0.05% xanthan gum and water with 1% polystyrene crystal solutions were tested in this study. The crystals used in this study were Dynoseeds TS 250 type, composed of 95-100% polystyrene crystal. The crystals had a mean particle size of 0.23 mm and density of 1050 kg/m^3. The rheological properties for these solutions were measured by an Advanced Rheometric Expansion System (ARES) with bob and cone geometry.

4. RESULTS AND DISCUSSION

4.1. Bubble Trajectory

The trajectory results of 0.1mL bubble is shown in fig. 2 for different liquids when measured over a height of 1.0 m from the point of air injection. The fig. 2 shows that the smaller bubble of 0.1mL deviates horizontally more in water than in other two liquids and the bubble shows a zigzag motion. The horizontal movement and the zigzag motion in 0.05% xanthan gum solution was observed less than that in water and the least in crystal suspension.

The trajectory results of 2mL, 5mL and 10mL bubbles are shown respectively in fig. 3, fig. 4 and fig. 5 for three different liquids. It can be seen that the fig. 3 and fig. 4 show the similar phenomena as is observed for the same three liquids in fig. 2. For bubbles of sizes 2mL and 5mL, path instability occurred as the bubble size increased. With increasing bubble size, the bubble shape changed from spherical to ellipsoidal, the bubble surface oscillations transformed from a simple oscillation to higher order forms, and the trajectory changed from a simple zigzag to more spiral trajectories. The bubble of 2mL initially followed a spiral motion and finally, attained a zigzag path for water.

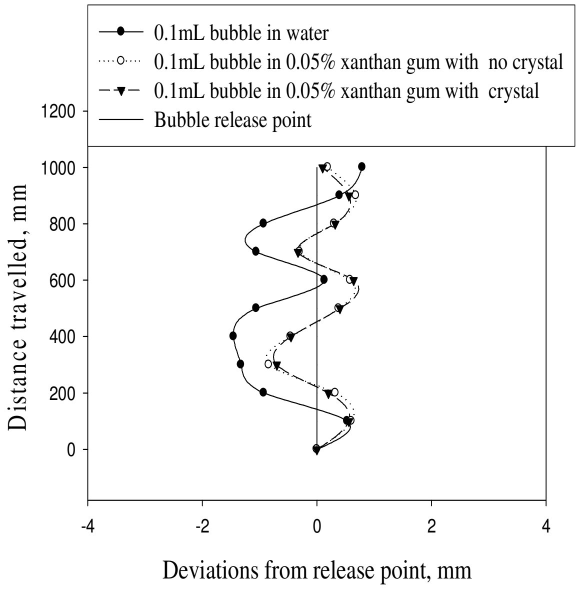

Figure 2: Rise trajectories of 0.1mL bubble in water, 0.05%% xanthan gum without crystal and 0.05% xanthan gum with crystal particle.

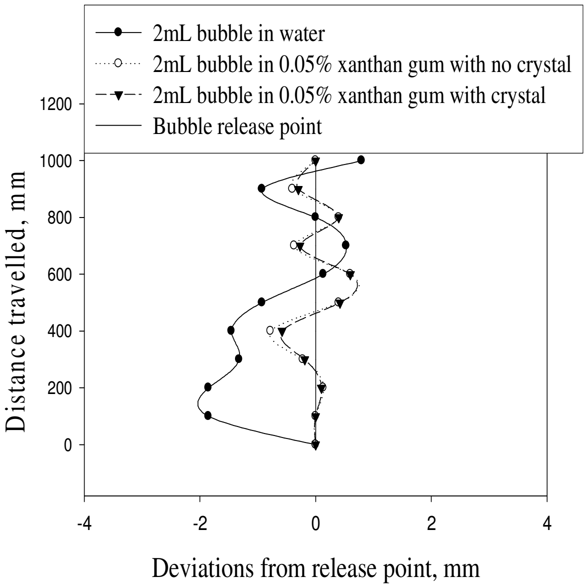

Figure 3: Rise trajectories of 2mL bubble in water, 0.05%% xanthan gum without crystal and 0.05% xanthan gum with crystal particle.

However, 2mL bubble followed only a zigzag motion for xanthan gum and crystal suspension until it finished its journey. On the other hand, the 5mL bubble, initially, choose the zigzag motion and finally, it switched to a spiral path for all liquids. The transition from spiral to zigzag motion was also observed by Aybers and Tapacu [4] as the bubble size increased. The transition from zigzag to spiral was also consistent with observations found in the literature [4, 10].

No zigzag motion was observed for the larger bubble of 10mL as seen in fig. 5 for water. The trajectory totally changed into a spiral motion for larger bubble. It is seen from fig. 5 that the 10mL bubble shows more spiral motion than the 5mL bubble.

The crystal suspended xanthan gum produced more spiral motion in comparison with water and xanthan gum solution. The larger bubbles however experience more resistance on top and deform as their size increases which results in spiral motion. Furthermore, it can be confirmed that the path instability was seen for ellipsoidal bubbles of sizes 2mL and 5mL only and not for larger bubble. This is consistent with the findings by other researchers [4, 5, 7, 8].

4.2. Influences of Re and We on Bubble Trajectory

The effect of Re and We on bubble trajectory are discussed for three regions. The characteristics of bubbles corresponding to Re and We are summarized in Table 1. At low Re and We for smaller bubbles (0.1mL), the rising bubble showed a zigzag trajectory. For the intermediate region, the bubbles of sizes 2mL and 5mL showed both zigzag and spiral trajectory. It is noted that the path instability occurred in this region due to increased in bubble size. At moderate We and Re, the bubbles deformed and changed from spherical to ellipsoidal and experienced more surface tension and inertia force which induced both zigzag and spiral trajectory. At high Re and We, larger bubbles (> 5mL) produced a spiral motion in all liquids as the effect of wake shedding influenced the bubble to induce a spiraling rising motion.

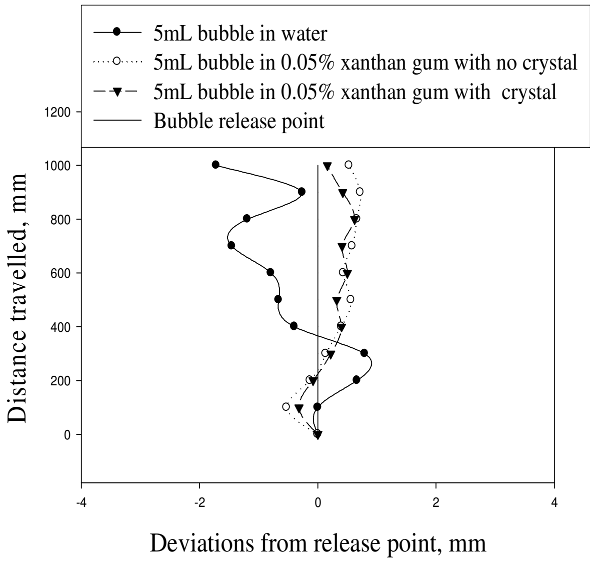

Figure 4: Rise trajectories of 5mL bubble in water, 0.05%% xanthan gum without crystal and 0.05% xanthan gum with crystal particle.

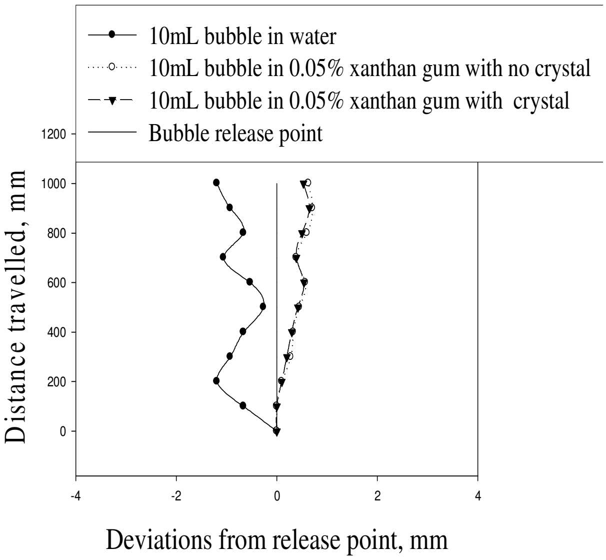

Figure 5: Rise trajectories of 10mL bubble in water, 0.05%% xanthan gum without crystal and 0.05% xanthan gum with crystal particle.

Table 1: The characteristics of bubbles corresponding to Re and We.

Bubble volume, mL	**Reynolds number (Re)**	**Weber number (We)**	**Bubble shape**	**Region**	**Zigzag motion**	**Spiral motion**
0.1	35.86	2.93	Nearly spherical	low	√	×
2	63.4	7.08	Ellipsoidal	Intermediate	√	√
5	88.95	11.82	Ellipsoidal	Intermediate	√	√
10	124.07	19.61	Spherical cap	High	×	√

5. CONCLUSIONS

A comprehensive comparison of the bubble trajectory is made by showing the experimental results for water, polymeric solution and a crystal suspension.

The smaller bubbles (0.1mL) exhibited the most horizontal movement in water and the least in crystal suspension. The least movement is due to increased viscosity of the crystal suspension resulting in higher friction on their surface.The larger bubbles (> 5mL) produced more spiral motion in crystal suspension than in other liquids. Because they experience more resistance on top and deform as their size increases that results in spiral motion. Wake shedding also influences the larger bubbles to induce a spiraling motion.

For bubbles of sizes 2mL and 5mL, path instability occurred and they produced two distinct unstable zigzag and spiral trajectories. This is due to path oscillations caused by wake instability.

At low region of Re and We, smaller bubbles (0.1mL) produced zigzag trajectory. For the intermediate region, bubbles of sizes 2mL and 5mL followed both zigzag and spiral trajectory. At high Re and We, larger bubbles (> 5mL) showed only spiral trajectory.

The dynamics of the bubble trajectories are complex in nature, resulting in interesting trajectories, shapes and motion. Therefore further research is warranted.

ACNOWLEDGEMENTS

The authors gratefully acknowledge the financial support from Sugar Research Institute, Queensland, Australia and the technical assistance provided by Mr. Ray Kearney in the experimental works. N.M.S. Hassan is thankful to Central Queensland University and PELM centre for the award of a research scholarship to pursue this study.

REFERENCES

[1] Magnaudet, J. and Eames, I., The Motion of High-Reynolds-Number Bubbles in Inhomogeneous Flows, *Annu. Rev. Fluid Mech.*, 32, pp. 659-708, 2000

[2] Kulkarni, A. A. and Joshi, J. B., Bubble Formation and Bubble Rise Velocity in Gas-Liquid Systems: *A Review, Ind. Eng. Chem. Res.*, 44, 2005.

[3] Ellingsen, Kjetil and Risso, Frederic., On the rise of an ellipsoidal bubble in water: oscillatory paths and liquid-induced velocity, *J. Fluid Mech.* 440, pp. 235-268, 2001.

[4] Aybers, N. M. and Tapacu, A., The motion of gas rising through a stagnant liquid, Warme-und Stoffubertragung, 2, pp. 118-128, 1969

[5] Haberman, W. L., Morton, R. K., An Experimental Study of Bubbles moving in Liquids, *ASCE,* 387, pp. 227-252, 1954

[6] Yoshida, S. and Manasseh, R., Trajectories of rising bubbles, *The 16th Japanese Multiphase Flow Symposium*, Touya, Hokkaido, 1997

[7] Wegener, P. P. and Parlange, J. Y., Sherical-cap bubbles. *Annu. Rev. Fluid Mechanics*, 5, pp. 680-689, 1973

[8] Shew, W. L., Poncet, S. and Pinton, J. F., Viscoelastic Effects on the Dynamics of a Rising Bubble, *Journal. of Statistical Mechanics*, P01009, 2006

[9] Wu, M. and Gharib, M., Experimental Studies on the Shape and Path of Small Air Bubbles Rising in Clean Water, *Physics of Fluids,* 14 (7), 2002.

[10] Saffman, P. G., On the Rise of small air Bubbles in Water, Trinity College, Cambridge, 1956

[11] Feng, Z. C. and Leal, L. G., Nonlinear Bubble Dynamics, *Annu. Rev. Fluid Mechanics.*, 29, 201, 1997.

[12] Shew, W. L. and Pinton, J. F., Dynamical Model of Bubble Path Instability, PRL 97, DOI: 144508, 2006

[13] Tsuge, H. and Hibino, S., The motion of Single Gas Bubbles Rising in Various Liquids, Kagaku Kogaku, 35 (65), 1971.

[14] Hassan, N. M. S., Khan, M. M. K. and Rasul, M. G., Characteristics of air Bubble Rising in Low Concentration Polymer Solutions, *WSEAS TRANSACTIONS on FLUID Mechanics*, ISSN: 1790-5087, 2 (3), pp. 53-60, 2007.

[15] Hassan, N. M. S., Khan, M. M. K. and Rasul, M. G., An Investigation of Bubble Trajectory and Drag Co-efficient in Water and Non-Newtonian Fluids, WSEAS Transactions on Fluid Mechanics, Special issue: Sustainable Energy and Environmental Fluid Mechanics, ISSN: 1790-5087, 3(3), pp. 261 -270, 2008.

“Proceedings of the 4th BSME-ASME International Conference on Thermal Engineering
27-29 December, 20086, Dhaka, Bangladesh”

CONTROL OF A MOBILE ROBOT THROUGH VOICE USER INTERFACE

S. M. Mahfuzur Rahman[1], M. S. Islam[2], M. S. Arefin[2] and M. T. Islam[1]

[1]Department of Mechanical Engineering, CUET, Bangladesh
[2]Department of Computer Science and Engineering, CUET, Bangladesh
Email: smmrahman@cuet.ac.bd

ABSTRACT

In industrial automation robots play a vital role in a wide range of applications. In this paper, a mobile robot has been designed and fabricated which can perform different tasks according to user’s instruction. The position and movement of the robot are controlled by the human over voice user interface (VUI). A series of experiments have been carried out to evaluate the working ability of the designed robot under different circumstances. Experiments show the effective performance of the robot in real time applications. Another advantage is that this robot can be used effectively in small industries to reduce the manufacturing cost after a little modification.

KEYWORDS: *Mobile robot, robot control, voice user interface.*

1. INTRODUCTION

There is a growing interest worldwide on the concept and possible applications of robots [3, 6]. This interest is motivated by the widespread perception that advances in the development of autonomous or teleoperated machines capable of carrying out useful tasks, thus substantially extending the range of application of current machines and possibly leading to a technological breakthrough whose effects could be comparable to those determined by the Mechatronics revolution [1, 4, 5]. The term “robot” generally connotes some anthropomorphic (human-like) appearance [2]. Brooks [9] research coined some research issues for developing humanoid robot and one of the significant research issues is to develop machine that have human-like perception. The five classical human sensors - vision, hearing, touch, smell and taste; by which they percept the surrounding world. The goal of this work project was to introduce a “hearing” sensor to the mobile robot such that it is capable to interact with human through Spoken Natural Language. Speech recognition (SR) is a prominent technology, which helps us to introduce “hearing” as well as Natural Language interface through Speech for the Human-Robot interaction. So the promise of anthropomorphic robot is starting to become a reality. We have chosen Mobile Robot, because this type of robot is getting popular as a working robot in the social and industrial context, where the main challenge is to interact with human. We chose a Software SR system for Voice User Interface (VUI) implementation. Several SR interface robotic systems have been investigated [10, 11, 12]. Most of the projects emphasize on Mobile Robot. Now a day this type of robot is getting popular as a service robot and working robot at indoor and outdoor applications.

In this work a prototype of mobile robot has been designed and fabricated which can work following the human spoken command. We choose English, because it is most recognized international Language. The robot understands its task from the dialogues has spoken. The system is user independent.

2. SPEECH RECOGNITION AND VUI

Speech Recognition technology promises to change the way we interact with machines (robots, computers etc.) in the future. This technology is getting matured day by day and scientists are still working hard to overcome the remaining limitations. Speech Recognition (SR) is the process of converting an acoustic signal, captured by micro-phone or a telephone, to a set of words [13]. There are two important parts of SR: (a) recognize the series of sound and (b) identify the word from the sound. This recognition technique depends also on many parameters - Speaking Mode, Speaking Style, Speaker Enrollment, Size of the Vocabulary, Language Model, Perplexity, Transducer, etc [13]. There are two types of Speak Mode for speech recognition system - one word at a time (isolated-word speech) and continuous speech. Depending on the speaker enrolment, the speech recognition system can also divide - Speaker dependent and Speaker independent system. In Speaker dependent systems user need to be train the systems before using them, on the other hand Speaker independent system can identify any speaker’s speech. Vocabulary size and the language model also important factors in a Speech recognition system. Language model or artificial grammars are used to confine word combination in a series of words or sounds. The size of the vocabulary also should be in a suitable number. Large numbers of vocabularies or many similar sounding words make recognition difficult for the system.

In Voice user interface (VUI), when the user give the instruction like “Go to office”, then it should understand the object “office”. Actually, the Robot should understand of its environment and its task. User interface is an important component of any product handle by the human user. The concept of robotics is to make an autonomous machine, which can replace human labor. But, to control the robot or to provide guide line for work, human should communicate with the robot and this concept conclude the Roboticists to introduce User Interface to communicate with robot. In the past decades GUI (Graphical User Interface), Keyboard, Keypad and Joystick were the dominating tools for Interaction with machine. Now there are several new technologies are introduced in Human machine interaction filed. One of the important components of spoken interface is microphone. Microphone hears everything. In case of noisy data and an irrelevant instruction for a specific environment, like if the robot stands in front of a wall and it receives the instruction “go ahead”, then it should able to give a message to the user about the situation.

Another component is Speaker (Loud Speaker). If anything goes wrong then the Robot can inform the user through Speaker (Loud Speaker) using Speech synthesizer. For example, if the Robot doesn’t understand the command, then it can give the feedback to user through speech or dialogue - like, “I don’t understand” using Speech synthesizer. Fig.1 shows a general overview of Spoken Natural Language Interface for Robotics Control.

3. ROBOT CONSTRUCTION

The term “robot” generally connotes some anthropomorphic (human-like) appearance; consider robot “arms” for welding [7]. The main goal of robotics is to make Robot workers, which can smart enough to replace human from labor work or any kind of hazardous tasks.

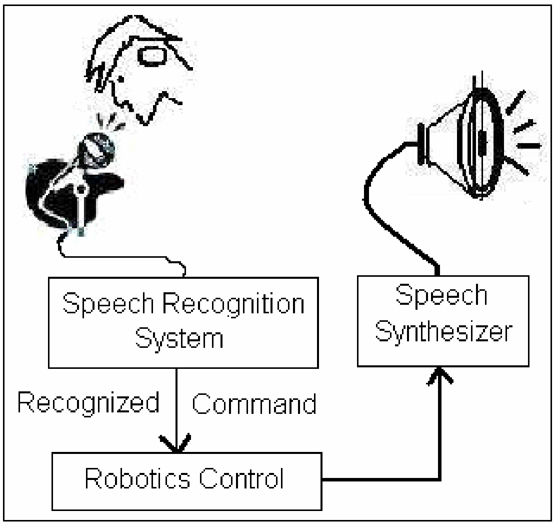

Fig.1 Typical Spoken Natural Language Interface in Robotics [2].

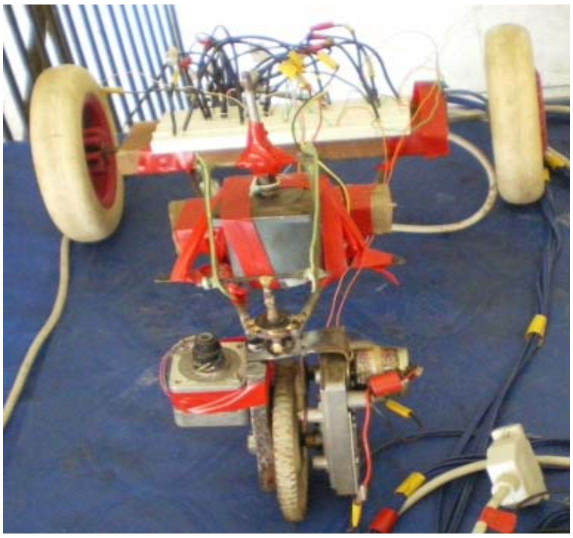

Fig.2 Prototype of the mobile Robot.

The robot system comprises of three parts; designing the mechanical structure, designing the electrical circuitry and developing the software. Three parts have distinct functions.

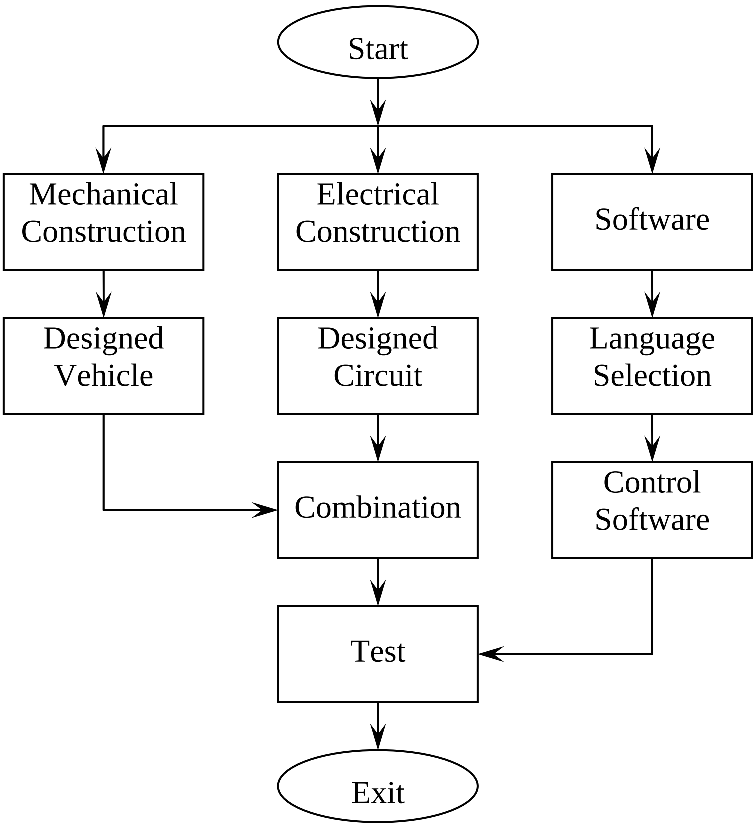

Fig.3 Block Diagram of overall System.

Combining the three parts properly a robot system is constructed that can work properly according to the oral instructions given by human. Human gives oral instructions through a micro-phone. The instructions are processed by the Speech Recognition (SR) system in a computer and then direct the robot controller. The controller then controls the movement of the robot. Both serial and parallel ports are used for communication [8]. A photograph of the prototype mobile robot and the block diagram of the system are shown in Fig. 2 and Fig.3 respectively. Mechanical part connects motors, wheels, gear mechanism and bearings with the body of the robot. Electrical circuitry interconnects ICs, transistors, relays and power unit as per design. We use C language for signal processing and Java scripts for SR system, a flowchart of the software development algorithm is shown in Fig.4. Two motors have been used. A gear motor is used to control the motion and a stepper motor is used to control the steering of the mobile robot.

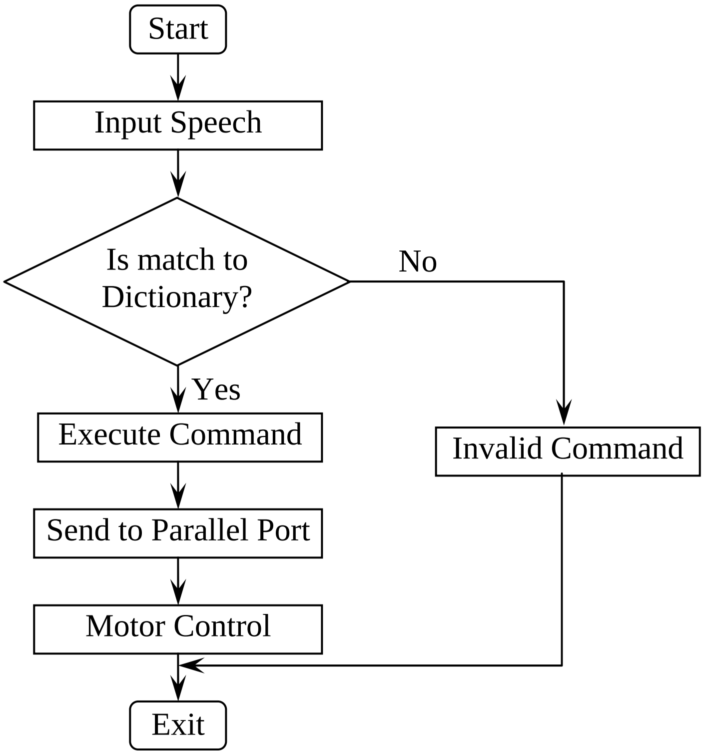

Fig. 4 Flowchart of Software Development Algorithm.

4. EXPERIMENTS AND RESULTS

A series of experiments have been carried out in different test conditions. Experimental results show the effective performance of the robot to follow the instructions given by human over VUI. The robot can do work what is instructed and also capable to cross any obstacles in its way.

5. CONCLUSIONS AND FUTURE RESEARCH

A mobile robot is designed and fabricated which is able to move at any desired direction and able to cross any obstacle in its way. The position and movement of the robot can be controlled by the human over VUI. A gear-wheel mechanism is used to cross the obstacle in its way. The mobile robot can move on the smooth path as well as on the unsmooth path. It can also carry goods on it. Additional advantage is that, after a little modification, this robot can be used effectively in small industries to reduce the manufacturing cost, because the system is user independent. Thus, anyone can give instructions to the robot to perform specific task. In future study we intend to work with the five classical human sensors step by step by which robot could percept the surrounding world.

6. REFERENCES

[1] R. J. Schilling, Fundamentals of Robotics, Prentice-Hall Inc., 1972.

[2] S. Kibria, “Speech Recognition for Robotic Control,” Master’s thesis, Umea University, Sweden, December 2005.

[3] H. Ueno,”A Knowledge Based Information Modeling for Autonomous Humanoid Service Robot” IEICE Trans. on Information & Systems, 2002

[4] Saeed B. Niku, Introduction to Robotics Analysis, Systems & Applications.

[5] E. Dertien. ”Realization of an energy-efficient walking robot “, Master’s thesis, University of Twente, June 2005.

[6] Y Xie ” Dynamic effects of an upper body on a 2D bipedal robot”, University of Twente, EEMCS, Netherlands.

[7] R.R. Murphy, Introduction to AI ROBOTICS. The MIT press, Cambridge, Massachusetts, London,UK, 2000.

[8] Handbook for “Parallel Port Design” by James Baraelo.

[9] R. A. Brooks, C. Breazeal, M. Marjanovic, B. Scassellati, and M.M. Williamson. The cog project: Building a humanoid robot. Lecture Notes in Computer Science, 1562:52–87, 1999.

[10] Guido Bugmann. Effective spoken interfaces to service robots: open problems. In AISB’05:Social Intelligence and Interaction in Animal, Robots and Agents-SSAISB 2005 Convention, pages 18–22, Hatfield,UK, April 2005.

[11] Dominique Estival. Adding lanuage capabilities to a small robot. Technical report, University of Melbourne, Australia, 1998.

[12] P. Nugues, M. Haage, S. Susanne, “A prototype robot speech interface with multimodal feedback” In Proceedings of the IEEE- Int. Workshop Robot and Human Interactive Communication, p247–252, Berlin Germany, Sept 2005.

[13] Survey of the state of the art in human language technology. Cambridge University Press ISBN 0-521-59277-1, 1996.

Proceedings of the 4th BSME-ASME International Conference on Thermal Engineering
27-29 December, 2008, Dhaka, Bangladesh

WGM SENSOR FOR MEASURING THERMAL DEFORMATION IN MEMS APPLICATIONS

Anisur Rahman[1], Md. Mahabubur Rahman[2], and Reginald Eze[3]

[1,3]Thermal Optics Laboratory, Department of Mechanical Engineering
Polytechnic Institute of NYU, 6 MetroTech Center, Brooklyn, NY 11201, USA
[2]Jamalpur Technical School and College, Jamalpur, Bangladesh

ABSTRACT

We have reported a novel optical sensor based on Whispering Gallery Mode (WGM) resonance for measuring thermal deformation in Micro-Electro-Mechanical Systems (MEMS) devices. New asymptotic expressions for Transverse Electric (TE) and Transverse Magnetic (TM) waves are developed based on electromagnetic theory derivations for the large size parameter (pi times diameter divided by wavelength of light) limits. The optical thermal deformation sensor is characterized both theoretically and experimentally by considering the fact that the size parameter of the microspheres is very large at optical wavelengths. As a prototype thermal deformation sensor, an optical fiber experimental setup with tunable laser diode has been used for realizing the effect of WGM resonances due to change in surrounding temperature of a dielectric microsphere made of BK-7 glass. The quality factor of experimental resonance spectra observed in the laboratory is calculated approximately in the order of 10^4 which is sensitive enough for detecting micro or nano level deformation changes in the surrounding medium. The novel optical sensor can measure the thermal deformation in the MEMS devices as small as sub-micron or nano meter level. This sensor could potentially be used for nano technology, MEMS devices, biomedical applications, and other micro devices.

KYEWORDS: *Optical sensors, WGM resonances, Thermal deformation, MEMS, MDR sensors, Temperature sensing.*

1. INTRODUCTION

In recent time, there has been a growing interest in the development of optical sensing in MEMS devices. However, WGM resonators have earned especial attention due to its unique characteristics [1, 2]. Since dielectric microsphere resonators inherent high Q factor and finesse, various potential applications have been reported over the years, e.g., thermo-optical switches [3], accelerating charged particles [4], optical acceleration sensors [5], coupling of optical power between microcavities and waveguides [6], etc.

There are some theoretical approaches based on WGM resonances in dielectric microspheres have been reported in the literatures [7-10]. However, mathematical formulation reported in the literatures using quantum theory have some significant disadvantages which includes difficult to follow, theory can not be used to demonstrate the experimental results and can not give simple usable expression. In this study, we have reviewed our previous publications [11, 12] to design a novel optical thermal deformation sensor in MEMS devices. Complete asymptotic solutions of TE and TM waves in dielectric microspheres for large size parameter are presented in [11, 12], which are simpler and mathematically robust than existing approaches presented in the literatures [7-10]. The developed theoretical formulation has compared with our experimental results for validation purposes.

As a prototype experimental setup, a fiber-sphere coupler is used in the laboratory to detect the thermal deformation using Morphology Dependent Resonance (MDR) shifts in optical wavelengths. Based on the experimental results the proposed optical thermal deformation sensor has been designed for detecting the thermal deformation in MEMS devices. The MDR shift with the variation of surrounding temperature of microspheres reveals the basis of optical thermal deformation sensor which is directly fabricated on silicon wafer as *in-situ* MEMS devices. Since the proposed sensor will be fabricated as *in-situ* MEMS devices, the sensor can directly measure micro level thermal deformation by using WGM based MDR wavelength shifts. The presented optical sensor is novel in comparison of sensors reported in the literatures [13-15]. The sensor could be used to measure the thermal deformation of MEMS devices without even measuring the device temperature. The quality factor of prototype fiber-sphere coupler is calculated approximately in the order of 10^4, which is sensitive enough for detecting micro or nano level thermal deformation. The proposed optical sensor can measure the thermal deformation in the MEMS devices as small as sub-micron or nano meter level.

2. NEW MATHEMATICAL DEVELOPMENT

Complete asymptotic solutions of WGM resonances for TE and TM waves in dielectric microspheres can be found in our previous publications [11] and [12], respectively. In this paper, a brief review of our new mathematical formulations will be highlighted. Figure 1 shows a typical fiber-sphere coupler which could be used in optical setup for sensing sub-micron or nano level changes in surrounding medium.

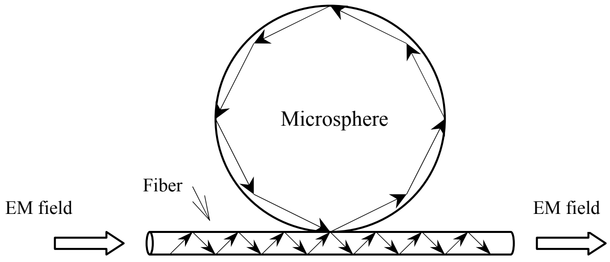

Figure 1: Schematic of a typical fiber-sphere coupler.

In perfect fiber-sphere coupling condition, Electro-Magnetic (EM) field traveling through the optical fiber will couple with microsphere. The light particle also known as photon travels through inner surface of the sphere due to total internal reflection (TIR) when the refractive index of the dielectric microsphere is greater than the refractive index of surrounding medium. While EM wave travels inside the sphere, waves interfere each other in particular wavelength due to circular travel path of the sphere and produce MDR. After circumnavigating the microsphere, the light wave returns to the starting point in phase to interfere constructively with itself and WGM resonance occurs. This constructive interference gives resonance peaks at certain discrete wavelengths and these resonance peaks are known as MDR [9]. In this paper a simple approach has been developed to explain MDR peaks with the variation in surrounding temperatures and that cause thermal deformation in microcavities.

In this analysis we are assuming EM wave modes are existed inside the sphere and excited by the evanescent modes from the fiber optic waveguide. The solutions inside the sphere are matched to the scattered field external to the sphere at the boundaries, where it is expected that the externally scattered field decays rapidly in the radial direction. Maxwell equations [16] can be used to explain the propagation of EM waves in dielectric microspheres also known as microcavities,

$$\nabla \cdot \vec{E} = 0 \quad \& \quad \nabla \times \vec{E} = i\omega\mu\vec{H} \tag{1a}$$

$$\nabla \cdot \vec{H} = 0 \quad \& \quad \nabla \times \vec{H} = -i\omega\varepsilon\vec{E} \tag{1b}$$

It is found that a physically realizable time-harmonic EM field in a linear, isotropic, homogeneous medium will satisfy the vector wave equation [16],

$$\nabla^2 \vec{E} + \omega^2 \varepsilon\mu\vec{E} = 0 \tag{2a}$$

$$\nabla^2 \vec{H} + \omega^2 \varepsilon\mu\vec{H} = 0 \tag{2b}$$

For a given scalar function ψ, vector wave Eq. (2) can be expressed as a scalar wave equation if ψ is a solution to the scalar wave equation,

$$\nabla^2 \psi + \omega^2 \varepsilon\mu\psi = 0 \tag{3}$$

The scalar wave equation in spherical polar coordinates is

$$\frac{1}{r^2}\frac{\partial}{\partial r}\left(r^2\frac{\partial\psi}{\partial r}\right)+\frac{1}{r^2\sin\theta}\frac{\partial}{\partial\theta}\left(\sin\theta\frac{\partial\psi}{\partial\theta}\right)+\frac{1}{r^2\sin\theta}\frac{\partial^2\psi}{\partial\phi^2}+\omega^2\varepsilon\mu\psi = 0 \tag{4}$$

Particular solutions and generating functions to Eq. (4) can be expressed as [16]

$$\psi(r,\theta,\phi) = R(r)\Theta(\theta)\Phi(\phi) \tag{5}$$

2.1 WGM resonances due to TE wave:

When $\vec{E}$ tangential to sphere surface (TE mode), EM field inside the sphere can be expressed as [16]

$$\vec{E}_{in} = \sum_{n=1}^{\infty} E_n c_n \vec{M}_{on}^{(1)} \tag{6a}$$

$$\vec{H}_{in} = -\frac{k_{in}}{\omega\mu}\sum_{n=1}^{\infty} E_n i c_n \vec{N}_{on}^{(1)} \tag{6b}$$

The scattered EM field from the sphere can be expressed as [16]

$$\vec{E}_{out} = -\sum_{n=1}^{\infty} E_n b_n \vec{M}_{on}^{(3)} \tag{7a}$$

$$\vec{H}_{out} = \frac{k_{out}}{\omega\mu}\sum_{n=1}^{\infty} E_n i b_n \vec{N}_{on}^{(3)} \tag{7b}$$

where $E_n = i^n E_0 \left(2n+1\right)/n\left(n+1\right)$, E_0 is amplitude of the EM wave, $k_{in} = \frac{2\pi m_1}{\lambda_0}$, $k_{out} = \frac{2\pi m_2}{\lambda_0}$, m_1 & m_2 are refractive indices of sphere & outside medium, respectively, $m = \frac{m_1}{m_2}$ is relative refractive index.

The necessary boundary conditions for both electric and magnetic fields can be expressed as

$$\vec{E}_{in}\Big|_{\tan gential} = \vec{E}_{out}\Big|_{\tan gential} \qquad \text{at } r=R \tag{8a}$$

$$\vec{H}_{in}\Big|_{\tan gential} = \vec{H}_{out}\Big|_{\tan gential} \qquad \text{at } r=R \tag{8b}$$

Applying Eq. (6) & Eq. (7) into Eq. (8), and expanding the vector spherical harmonics in component form yields:

$$\frac{h_{n+1}^{(1)}(x)}{h_n^{(1)}(x)} = m\frac{j_{n+1}(mx)}{j_n(mx)} \tag{9}$$

Expanding spherical Bessel function of first kind (j_n) and third kind (h_n^1) for large x and performing rigorous mathematical simplification, Eq. (9) will give a simple form for size parameter,

$$x = \frac{\pi}{2m}(n+1+2N)$$

$$x = \frac{\pi}{2m} I \tag{10}$$

where integer I defined as $I = (1+n+2N)$. Equation (10) reveals that size parameter for any MDR wavelength will be the product of an integer and a constant $\left(\pi/_{2m}\right)$. For consecutive MDR peak wavelengths, the right side of Eq. (10) will be multiple of consecutive integer numbers.

2.2 WGM resonances due to TM wave:

When $\vec{H}$ tangential to sphere surface (TM mode), EM fields inside the sphere can be expressed as [16]

$$\vec{E}_{in} = -i\sum_{n=1}^{\infty} E_n d_n \vec{N}_{en}^{(1)} \tag{11a}$$

$$\vec{H}_{in} = -\frac{k_{in}}{\omega\mu}\sum_{n=1}^{\infty} E_n d_n \vec{M}_{en}^{(1)} \tag{11b}$$

The scattered EM fields from the micro-sphere can be expressed as [16]

$$\vec{E}_{out} = i\sum_{n=1}^{\infty} E_n a_n \vec{N}_{en}^{(3)} \tag{12a}$$

$$\vec{H}_{out} = \frac{k_{out}}{\omega\mu} \sum_{n=1}^{\infty} E_n a_n \vec{M}_{en}^{(3)} \tag{12b}$$

Applying boundary conditions (Eq. (8)) into Eq. (11) & Eq. (12), and simplifying further yields,

$$\frac{h_{n+1}^{(1)}(x)}{h_n^{(1)}(x)} = \frac{1}{m}\frac{j_{n+1}(mx)}{j_n(mx)} + \frac{1}{x}(n+1)\left(1 - \frac{1}{m^2}\right) \tag{13}$$

After expanding spherical Bessel function of first kind (j_n) and third kind (h_n^1) for large x, Eq. (13) will be simplified to

$$x = \frac{\pi}{2m} I \tag{14}$$

where I is an integer, $I = (n + 2N)$. As expected, similar to TE mode, Eq. (14) shows that size parameter for any TM-MDR wavelength will be the product of an integer 'I' & a constant $\left(\pi/2m\right)$. This fact reveals that MDR shifts will be same for both TE and TM modes, i.e., regardless of polarization in EM waves MDR shifts remain same. According to WGM concepts, for consecutive MDR peak wavelengths, the right side of Eq. (10) and Eq. (14) will be multiple of consecutive integer numbers. The expression of size parameter in Eq. (10) and Eq. (14) are also valid for varying surrounding temperature which could be used to design WGM thermal deformation sensors in MEMS devices.

3. EXPERIMENTAL PROCEDURE

The new mathematical approach presented in previous section needed to be verified with experimental and published results and which has already reported in [11, 12]. The schematic of the prototype experimental setup is shown in Fig. 2, where a BK-7 glass microsphere (refractive index = 1.517) held by tweezer is coupled with eroded fiber (not shown in the figure). The detail of the experimental procedure can be found in [11].

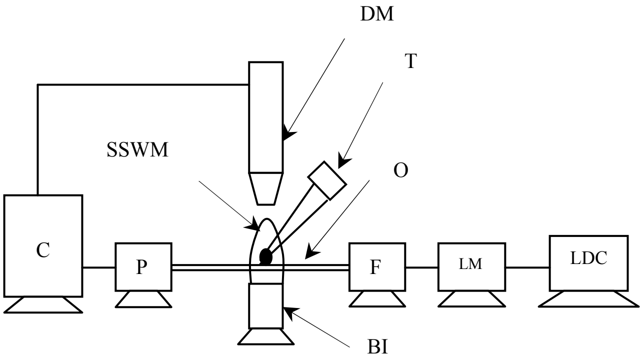

Figure 2: Schematic of the experimental setup. Where, the abbreviation represents: BI=Back Illuminator, C=Computer, DM=Digital Microscope, F=Fiber coupler, LDC=Laser Diode Controller, LM=Laser Diode Mount, O=Optical Fiber, P=Photodiode, T=Tweezer, SSWM=Sphere-Submerged in Water Meniscus.

Optical coupling requires exposing the evanescent field in a fiber optic [18]. The experiment is done on a single mode optical fiber for which the refractive index of the core and cladding are respectively $n_{core} = 1.462$ and $n_{clad} = 1.457$. Hydrofluoric acid (HF) is used to etch the fiber chemically. A digital microscope is used to monitor the etching and capture the images. Some captured images of eroded fiber are presented in Fig. 3.

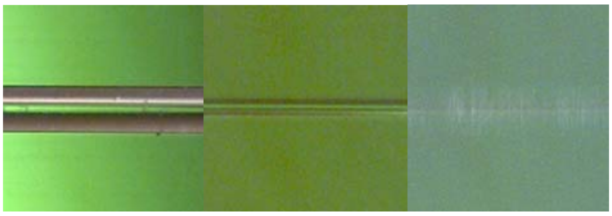

(a) (b) (c)

Figure 3: Single mode optical fiber: (a) Exposed cladding (≈125µm), (b) Diameter is eroding away during HF etching, (c) Exposed core (≈5µm) & laser beam is scattering from exposed core showing the glow which is the proof of evanescent field around the exposed core [11].

4. SENSOR DESIGN

Measuring the thermal deformation of MEMS devices is a real challenge. In this paper, we have tried to show a model, first to our knowledge, to detect/measure thermal deformation in MEMS devices. Silicon microdisk-waveguide coupler has been reported to capture WGM effects [2]. The Morphology Dependent Resonance (MDR) shift with the variation of surrounding temperature of microspheres reveals the basis of optical thermal deformation sensor which could be directly fabricated on silicon wafer as *in-situ* MEMS devices.

Figure 4 shows the schematic of a typical micro-chip of MEMS devices where a silicon microdisk-waveguide coupler will capture the WGM resonance effects due to thermal deformation in the microdisk. When the surrounding temperature of the micro-chip will change, there will be a thermal deformation in the microdisk that causes the MDR shifts in optical wavelengths. Since the proposed sensor will be fabricated as *in-situ* MEMS devices, the sensor can directly measure micro level thermal deformation by using WGM based MDR wavelength shifts. The sensor could be used to measure the thermal deformation of MEMS parts (as shown in Fig. 4) in the microchip without even measuring the microchip temperature. The quality factor of prototype fiber-sphere coupler is calculated approximately in the order of 10^4, which is sensitive enough for detecting micro or nano level thermal deformation.

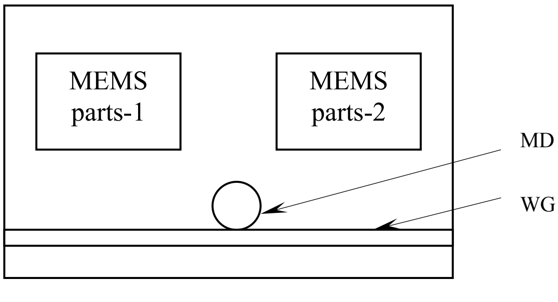

Figure 4: Schematic of a typical micro chip with silicon microdisk-waveguide coupler. Where WG = wave guide, MD = Microdisk.

As a prototype experimental setup, a fiber-sphere coupler is used in the laboratory to detect the thermal deformation using MDR shifts in optical wavelengths. Based on the experimental results the proposed optical thermal deformation sensor has been designed for detecting the thermal deformation in MEMS devices. Conventional MEMS fabrication process can be used to fabricate the proposed optical sensor [2].

5. RESULTS AND DISCUSSION

An experiment has been conducted as a prototype thermal deformation sensor using fiber-sphere coupler. Wavelength of the laser diode varies with the change of laser current. A laser diode controller is used for tuning the laser current from 61 mA to 65 mA at constant temperature of 19^{o}C. The output optical signal is captured by a photodiode. As laser wavelength depends on laser current, the current vs wavelength calibration gives the corresponding wavelength with respect to current. WGM resonances occur in a particular wavelength, known as resonance wavelength, while wavelength is changing with respect to current, MDR peak is also shifting. The MDR peaks are almost equally spaced with the change of wavelength. The quality factor *Q* of observed resonance spectra shown in Fig. 5 is calculated as 3.9×10^4 [11].

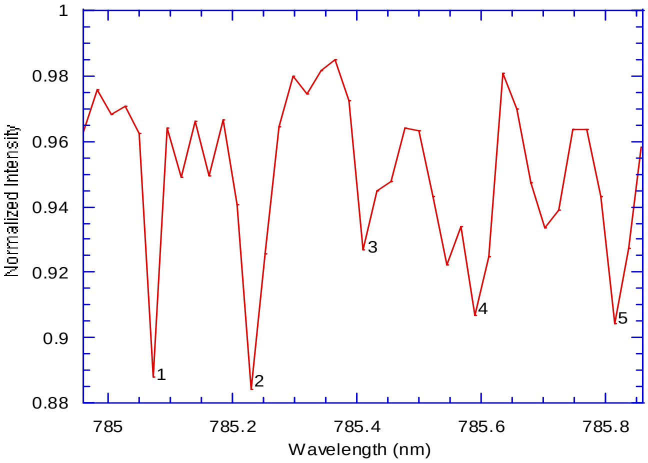

Figure 5: MDR peaks shifted as wavelength varies at 19^{o}C.

Table 1: Comparison between our experimental results and calculated values based on new mathematical formulation (Eq. (10) & Eq. (14)).

MDR peak	MDR wavelength (nm), λ_{exp}	Size parameter at resonance wavelength $x_{exp}=\frac{2\pi R}{\lambda_{exp}}$ (R = 500μm)	Acceptable integer, *I* $I=\frac{4mR}{\lambda_{exp}}$	Calculated size parameter with acceptable integer $x_{cal}=\frac{\pi}{2m}I$ (m = 1.517)	Error (%) $\varepsilon=\frac{\lvert x_{cal}-x_{exp}\rvert}{x_{cal}}$
1	785.07	4001.67	3865	4002.06	0.0097
2	785.23	4000.86	3864	4001.03	0.0042
3	785.41	3999.94	3863	3999.99	0.0013
4	785.60	3998.97	3862	3998.96	0.0003
5	785.81	3997.90	3861	3997.92	0.0005

Here we reviewed our previous results [11] for validating the developed mathematical formulation. Table 1 contains the comparison between developed theoretical model and experimental results found in the laboratory. The error between experimental result and calculated results are in the negligible range ($\sim 10^{-3}$ %) which supports the validation of developed theory.

It is necessary to derive a mathematical expression for calculating acceptable integer *I*. From Eq. (10) and Eq. (14), a simple expression for *I* can be found as,

$$x = \frac{2\pi R}{\lambda_{\exp}} = \frac{\pi}{2m} I$$

$$I = \frac{4mR}{\lambda_{\exp}} = \frac{2mD}{\lambda_{\exp}} \tag{15}$$

Solving Eq. (15) will give a real number and rounding it to nearest integer will give an acceptable integer *I* for each MDR peak wavelength. It reveals that consecutive MDR peak wavelengths give consecutive integer numbers (Table 1).

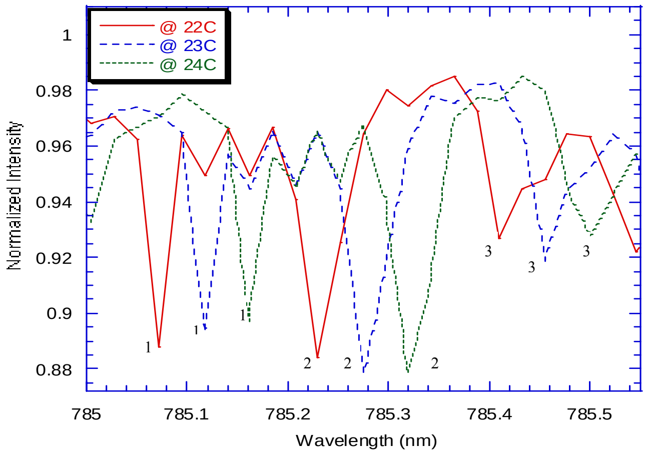

Figure 6: MDR peaks for three different surrounding temperatures as wavelength varies with current at constant laser diode temperature of 19^0C.

Figure 6 shows the spectrum plots of MDR peaks for three different surrounding temperatures of fiber-sphere coupler. When temperature of the fiber-sphere varied to 1^0C from 22^0C to 23^0C & 23^0C to 24^0C, there are shifts in resonance wavelengths (Fig. 6). For each temperature, we have three MDR peaks at 0.5 nm wavelength range. It is verified that size parameters corresponding to these three consecutive peaks at different temperatures are multiple of consecutive integers.

To design the proposed optical thermal deformation sensor for MEMS devices based on WGM resonances, we will use our experimental facts. In Fig. 6 it is evident that resonance wavelengths are shifted with the variation of surrounding temperatures of WGM resonators due to thermal deformation in micro resonators, i.e., changes in microsphere's diameter due to thermal expansion. The diameter of microcavity (BK-7 glass microsphere) is calculated by using Eq. (15) for each MDR wavelength at three different temperatures: 22^0C, 23^0C & 24^0C which are tabulated in Table 2. Similarly, we are expecting that the diameter of the microdisk as shown in Fig. 4 will change with the change in surrounding temperature [2, 19]. More details parametric and experimental studies will be presented in future publication.

Table 2 contains the calculated results of thermal responses of dielectric WGM resonators. The analysis of results (Table 2) with the variation of temperature shows that the new mathematical expressions for size parameter (Eq. (10) & Eq. (14)) are effectively described the effect of temperature in dielectric microspheres made of BK-7 glass. Shift in resonance wavelengths (Fig. 6) due to thermal deformation in microsphere can be used to demonstrate a novel optical thermal deformation sensor for measuring sub-micron or nano-meter or Angstrom level thermal deformation in MEMS devices.

Table 2: Comparison of microsphere diameter for different temperatures at each MDR wavelength.

Temperature (^{0}C)	Diameter of microsphere (BK-7) for different temperatures at each MDR wavelength,($\times 10^{-3}$ m)		
	Peak 1	Peak 2	Peak 3
	$D_1 = \frac{I_1 \lambda}{2m}$ ($m = 1.517,\ I_1 = 3865$)	$D_2 = \frac{I_2 \lambda}{2m}$ ($m = 1.517,\ I_2 = 3864$)	$D_3 = \frac{I_3 \lambda}{2m}$ ($m = 1.517,\ I_3 = 3863$)
22	1.00009971	1.0000414	1.00001203
23	1.00015805	1.000099736	1.000074048
24	1.000214484	1.000156155	1.00012688

Table 3 contains calculated thermal deformation in microsphere with the variation of temperature from 22^{0}C to 23^{0}C and 23^{0}C to 24^{0}C. The results show that nano meter level deformation can be effectively measured by proposed optical thermal deformation sensor. Similarly, we could expect that thermal deformation in MEMS devices can be detect /measure by using WGM microdisk resonators (Fig. 4).

Table 3: Thermal deformation of prototype microresonator (BK-7 glass) between two consecutive MDR peaks.

Temperature difference (^{0}C)	Thermal deformation of microsphere (BK-7 glass) between two consecutive MDR peaks, $\Delta\delta$ (nm/^{0}C)			
	Peak 1	Peak 2	Peak 3	Average
22 to 23	58.34	58.29	58.42	58.35
23 to 24	56.43	56.42	56.40	56.42

The sensitivity of prototype optical thermal deformation sensor based on WGM resonance is measured to be 57 nm/^{0}C i.e., molecular level (Angstrom, Å) deformation in MEMS devices due to one degree centigrade temperature change in the surrounding can be detected with proposed optical thermal deformation sensor.

6. CONCLUSION

We have presented a novel application of our newly developed theoretical model TE and TM modes based on WGM resonances [11, 12]. In this paper, a novel optical thermal deformation sensor for MEMS devices is presented with theoretical and experimental results. A laser based experiment has successfully been conducted as a prototype thermal deformation sensor to verify the thermal effect in WGM resonators and comparison between experimental results & calculated results based on developed theoretical approach yields negligible error ($\sim 10^{-3}$ %) which supports the validation of new approach. The new mathematical formulation successfully explains the effect in temperature variation in the dielectric microspheres and error level is very small. The quality factor, Q of resonance spectra observed in the laboratory is in the order of 10^4 which is sensitive enough to detect sub-micron or nano or Angstrom level thermal deformation in MEMS devices. Since the proposed sensor will be fabricated as *in-situ* MEMS devices, the sensor can directly measure micro level thermal deformation by using WGM based MDR wavelength shifts. The sensitivity of prototype optical thermal deformation sensor based on WGM resonance is measured to be 57 nm/^{0}C which means molecular level (Angstrom, Å) deformation in MEMS devices due to one degree centigrade temperature change in the surrounding can be directly detected/measured with proposed optical thermal deformation sensor. The present theoretical and experimental approaches can potentially be used in wide variety of areas which include electronic industries, MEMS, biosensors, nano technology research, and other micro/nano applications.

7. NOMENCLATURE

a	Arbitrary constant	l	Integer
b	Arbitrary constant	m	Relative refractive index
c	Arbitrary constant	$\vec{M}$	Vector spherical harmonic
d	Arbitrary constant	$\vec{N}$	Vector spherical harmonic
$\vec{E}$	Electric field vector	n	Integer
$\vec{H}$	Magnetic field vector	Q	Quality factor
h_n^1	Spherical Bessel function of third kind	R	Radius of the microsphere, (m)
I	Integer	r	Radial polar coordinate
j_n	Spherical Bessel function of first kind	x	Size parameter
k	Wave number		

Greek Symbols

θ	Zenith polar coordinate	ε	Complex permittivity
ϕ	Azimuth polar coordinate	ω	Angular frequency
λ	Wavelength of light, (m)	ψ	Given scalar function
μ	Permeability		

Subscripts

0	Free space	o	Odd
1	Inside sphere	in	Inside the sphere
2	Outside sphere	out	Outside the sphere
e	Even		

8. REFERENCES

[1] Matsko, A., and Ilchenko, V, 2006, “Optical Resonators with Whispering-Gallery Modes – Part II: Applications,” IEEE J. of Selected Topics in Quantum Electronics, **12**(1), pp. 15-32.

[2] Vahala, K., 2003, “Optical Microcavities,” Nature, **424**(6950), pp. 839-846.

[3] Tapalian, H. C., Laine, J. P., and Lane, P. A., 2002, “Thermooptical Switches Using Coated Microsphere Resonators,” IEEE Photonics Technology Letters, **14**(8), pp. 1118-1120.

[4] Zakowicz, W., 2005, “Whispering-Gallery-Mode Resonances: A New Way to Accelerate Charged Particles,” Physical Review Letters, **95**, pp. 114801-4.

[5] Laine, J. P., Tapalian, C., Little, B., and Haus, H., 2001, “Acceleration Sensor Based on High-Q Optical Microsphere Resonator and Pedestal Antiresonant Reflecting Waveguide Coupler,” J. Sensors and Actuators A, **93**(1), pp. 1-7.

[6] Yariv, A., 2000, “Universal Relations for Coupling of Optical Power between Microresonators and Dielectric Waveguides,” IEEE Electrons Letters, **36**(4)**,** pp. 321–322.

[7] Gumprecht, R. O., and Sliepcevich, C. M., 1953, “Scattering of Light by Large Spherical Particles,” J. Physical Chemistry, **57**, pp. 90-95.

[8] Teraoka, I., Arnold, S., and Vollmer, F., 2003, “Perturbation Approach to Resonance Shifts of Whispering-Gallery Modes in a Dielectric Microsphere as a Probe of a Surrounding Medium,” J. Opt. Soc. of Am. B, **20**(9), pp. 1937-1946.

[9] Johnson, B., 1994, “Morphology-Dependent Resonances of a Dielectric Sphere on a Conducting Plane,” J. Opt. Soc. of Am. A, **11**(7), pp. 2055-2064.

[10] Messica, A., Greenstein, A., and Katzir, A., 1996, “Theory of Fiber-Optic, Evanescent-Wave Spectroscopy and Sensors,” Applied Optics, **35**(13), pp. 2274-2284.

[11] Rahman, A., and Kumar, S., 2006, “An Asymptotic Approach for Radiation Resonance in Dielectric Microspheres,” 13th International Heat Transfer Conference (IHTC-13), Australia, Paper # RAD-16, Annals AIHTC, **13.**

[12] Rahman, A., and Kumar, S., 2007, “Effect of Radiation Resonances for Transverse Magnetic Wave in Dielectric Microspheres,” Proc. of 5th International Symposium on Radiative Transfer (ICHMT-RAD-07), Bodrum, Turkey, June 17-22.

[13] Cahill, D. G., Goodson, K., and Majumdar, A., 2002, “Thermometry and Thermal Transport in Micro/Nanoscale Solid-State Devices and Structures,” J. Heat Transfer, **124**(2), pp. 223-241.

[14] Gorecki, C., de Labachelerie, M., and Spajer, M., 2002, “The Role of Fiber Sensing Technologies in MEMS/MOEMS,” Proc. 15th Optical Fiber Sensors Conference, Oregon, USA, pp. 339-342.

[15] Yi, T., and Kim, C. J., 1999, “Measurement of Mechanical Properties for MEMS Materials,” J. Measurement Science & Technology **10**, pp. 706-716.

[16] Bohren, C., and Huffman, D., 1983, Absorption and Scattering of Light by Small Particles, John Wiley & Sons, Inc., NY, USA, pp. 82-94, Chap. 4.

[17] Abramowitz, M., and Stegun, I. A., 1965, Handbook of Mathematical Functions, Dover Publications, Inc., NY, USA, pp. 358-385, Chap. 9, 1965.

[18] Laine, J. P., Little, B. E., and Haus, H. A., 1999, “Etch-Eroded Fiber Coupler for Whispering-Gallery-Mode Excitation in High- Q Silica Microspheres,” IEEE Photonics Technology Letters, **11**(11), pp. 1429-1430.

[19] Quan, H., Guo, Z, and Pau, S., 2004, “Parametric Studies of Whispering-Gallery Mode Resonators,” Proc. of SPIE, Islam, S., et al., eds., **5593**, pp. 593-602.

Proceedings of the 4th BSME-ASME International Conference on Thermal Engineering
27-29 December, 2008, Dhaka, Bangladesh

TOWARD THE EXACT ELASTICITY SOLUTION OF A DEEP BEAM WITH GUIDED ENDS

M. Muzibur Rahman, S. Reaz Ahmed

Department of Mechanical Engineering
Bangladesh University of Engineering and Technology, Dhaka 1000, Bangladesh
E-mail: muzib1061@yahoo.com, reaz207@yahoo.com

ABSTRACT

An analytical investigation of the elastic field of a guided deep beam is carried out using displacement potential boundary modeling approach. The problem is formulated here in terms of a single function of space variables, defined in terms of displacement components, which has to satisfy a single partial differential equation of equilibrium. The relevant displacement and stress components are derived into infinite series using Fourier integral with coincided boundary conditions along with the physical boundary conditions. A comparative study shows that the analytical and numerical solutions are in good agreement but they differ considerably from that of the elementary beam theory.

KEYWORDS: *Analytical solution, Deep beam, Guided boundary, Displacement potential*

1. INTRODUCTION

A beam is said to be a deep one when the depth is comparable to its span. The design of deep beams based on classical Euler theory can be of serious error, as it takes no account of the effect of normal pressures on top and bottom edges of the beam caused by loads and reactions [1]. In an attempt to make up the limitation, different theories as well as their modifications have been reported in the literature [1-5]. However, each solution possesses certain limitations, and eventually none of the solutions are found to conform to all the physical characteristics of the problem appropriately. Even, photoelastic studies [6] as well as finite element analysis [7] have also been carried out for deep beams on two supports, mainly because all the physical conditions imposed on the beam could not be fully taken into account in the analytical methods of solution. Among the existing mathematical models of elasticity for the plane boundary-value stress problems, the stress function approach and the displacement formulation are noticeable [8]. The shortcoming of the stress function approach is that it accepts boundary conditions in terms of loading only; boundary restraints cannot be satisfactorily imposed on the stress function. Again, the displacement formulation involves finding two displacement functions simultaneously from two second-order elliptic partial differential equations, which is extremely difficult especially when the boundary conditions are a mixture of restraints and stresses. As a result, serious attempts had hardly been made in the past for stress analysis of practical elastic problems using this formulation. As stated above, neither of the existing formulations is suitable for solving problems of mixed boundary conditions.

Further, structures with guided boundaries are receiving increased importance in order to satisfy highly economic and precise design criteria in many of the engineering applications. In the solution of guided structures, the physical conditions of guided boundaries are mathematically modeled in terms of a mixed mode of boundary conditions. Since the exact analytical solution of mixed-boundary-value elastic problems is beyond the scope of existing mathematical models of elasticity, the use of a new formulation, namely, the displacement potential formulation [9-11] is investigated here to analyze the elastic behavior of a guided deep beam under uniform loading with two simple supports.

2. DISPLACEMENT POTENTIAL FORMULATION

With reference to a Cartesian coordinate system, in absence of body forces, the conditions of equilibrium for an isotropic elastic solid under plane stress condition can be written in terms of displacement components (u_x and u_y) as follows [8]:

$$\frac{\partial^2 u_x}{\partial x^2}+\left(\frac{1+\mu}{2}\right)\frac{\partial^2 u_y}{\partial x \partial y}+\left(\frac{1-\mu}{2}\right)\frac{\partial^2 u_x}{\partial y^2}=0 \tag{1a}$$

$$\frac{\partial^2 u_y}{\partial y^2}+\left(\frac{1+\mu}{2}\right)\frac{\partial^2 u_x}{\partial x \partial y}+\left(\frac{1-\mu}{2}\right)\frac{\partial^2 u_y}{\partial x^2}=0 \tag{1b}$$

where μ is Poisson's ratio. The stress displacement relations for plane stress problems are obtained from Hook's law as follows [9]:

$$\begin{bmatrix}\sigma_{xx}\\ \sigma_{yy}\\ \sigma_{xy}\end{bmatrix}=\frac{E}{1-\mu^2}\begin{bmatrix}1 & \mu & 0\\ \mu & 1 & 0\\ 0 & 0 & (1-\mu)/2\end{bmatrix}\begin{bmatrix}\dfrac{\partial u_x}{\partial x}, & \dfrac{\partial u_y}{\partial y}, & \left(\dfrac{\partial u_x}{\partial y}+\dfrac{\partial u_y}{\partial x}\right)\end{bmatrix}^T \tag{2}$$

Here, E is Young's modulus of the material. Instead of solving for two displacement components satisfying the two elliptic partial differential equations (1), in the present displacement potential approach, attempt is made to formulate the problem in terms of a single function of space variables. The displacement components are thus expressed in terms of a function, $\psi(x, y)$ as follows [11]:

$$\begin{bmatrix}u_x\\ u_y\end{bmatrix}=\begin{bmatrix}\alpha_1 & \alpha_2 & \alpha_3\\ \alpha_4 & \alpha_5 & \alpha_6\end{bmatrix}\begin{bmatrix}\dfrac{\partial^2\psi}{\partial x^2}, & \dfrac{\partial^2\psi}{\partial x\partial y}, & \dfrac{\partial^2\psi}{\partial y^2}\end{bmatrix}^T \tag{3}$$

where α's are material constants. For isotropic materials the values of α's are obtained as [11]

$$\left[\alpha_{i,}\ i=1,2,3,..,6\right]=\left[0,\ 1,\ 0,\ -2/(1+\mu),\ 0,\ -(1-\mu)/(1+\mu)\right]^T \tag{4}$$

Replacing the displacement components in Eq. (1) by Eqs. (3) and (4), it is found that Eq. (1a) is an identity, and eventually Eq. (1b) gives the only condition that $\psi(x, y)$ has to satisfy. The single governing equation of equilibrium thus becomes [10]

$$\frac{\partial^4\psi}{\partial x^4}+2\frac{\partial^4\psi}{\partial x^2\partial y^2}+\frac{\partial^4\psi}{\partial y^4}=0 \tag{5}$$

Combining Eqs. (2), (3), and (4), the expressions of displacement and stress components in terms of function $\psi(x, y)$ are obtained as follows [10]:

$$\begin{bmatrix}u_x(x,y)\\ u_y(x,y)\end{bmatrix}=-\begin{bmatrix}0 & -1 & 0\\ 2/(1+\mu) & 0 & (1-\mu)/(1+\mu)\end{bmatrix}\begin{bmatrix}\dfrac{\partial^2\psi}{\partial x^2}, & \dfrac{\partial^2\psi}{\partial x\partial y}, & \dfrac{\partial^2\psi}{\partial y^2}\end{bmatrix}^T \tag{6}$$

$$\begin{bmatrix}\sigma_{xx}(x,y)\\ \sigma_{yy}(x,y)\\ \sigma_{xy}(x,y)\end{bmatrix}=-\frac{E}{(1+\mu)^2}\begin{bmatrix}0 & 1 & 0 & -\mu\\ 0 & 2+\mu & 0 & 1\\ 1 & 0 & -\mu & 0\end{bmatrix}\begin{bmatrix}\dfrac{\partial^3\psi}{\partial x^3}, & \dfrac{\partial^3\psi}{\partial x^2\partial y}, & \dfrac{\partial^3\psi}{\partial x\partial y^2}, & \dfrac{\partial^3\psi}{\partial y^3}\end{bmatrix}^T \tag{7}$$

3. GEOMETRY AND LOADING OF THE BEAM

A rectangular section simply supported beam subjected to a uniformly distributed load at its top boundary, as shown in Fig. 1, is considered in this study. Beam length, depth and width are denoted by L, D and W, respectively. Since the plane stress is assumed here, the beam is considered to be of unit thickness. The two lateral ends of the beam are guided, where the axial displacements are restrained, but the lateral displacements are free to presume any value. The physical conditions at the boundaries of the beam are expressed mathematically as follows:

(a) Guided end, EF: $u_x(0,y)=0$ and $\sigma_{xy}(0,y)=0\ [0 \le y \le D]$

(b) Guided end, HG: $u_x(L,y)=0$ and $\sigma_{xy}(L,y)=0\ [0 \le y \le D]$

(c) Loaded boundary, EH: $\sigma_{xy}(x,D)=0\ [0 \le x \le L]$ and $\sigma_{yy}(x,D)=P/W\ [0.1L \le x \le 0.9L]$

(d) Supporting end, FG: $\sigma_{xy}(x,0)=0\ [0 \le x \le L]$ and $\sigma_{yy}(x,0)=4P/W\ [0 \le x \le 0.1L\ \&\ 0.9L \le x \le L]$

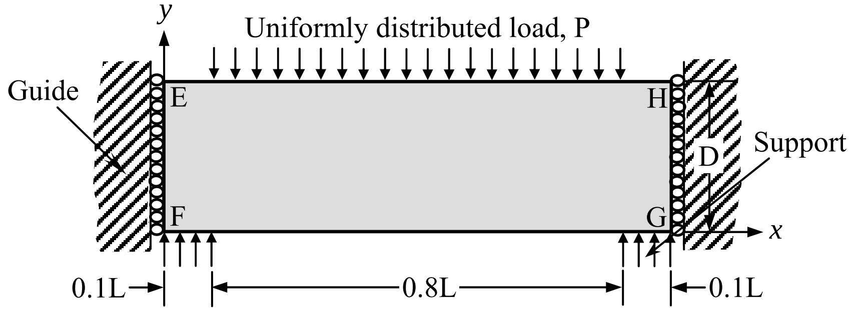

Fig. 1 Geometry and loading of the guided beam

4. SOLUTION PROCEDURE

For the present beam problem, the potential function ψ(x, y) is assumed at first in a way so that the physical conditions of the two opposing guided ends are automatically satisfied. The solution of the governing equation (5) is thus approximated as

$$\psi(x,\ y)\ =\sum_{m=1}^{\infty} Y_m(y)\cos\alpha x + K\,y^3 \tag{8}$$

where, $\alpha = (m\pi/L)$, K is an arbitrary constant and m = 1, 2, 3, ……..∞. When the governing equation (5) is satisfied by Eq. (8), we obtain the following ordinary differential equation:

$$Y_m^{////} - 2\alpha^2 Y_m^{//} + \alpha^4\,Y_m = 0 \tag{9}$$

This ordinary differential equation has the complementary function of repeated roots, and the general solution of Eq. (9) can be written as

$$Y_m = (A_m + B_m y)\,e^{\alpha y} + (C_m + D_m y)\,e^{-\alpha y} \tag{10}$$

where A_m, B_m, C_m and D_m are arbitrary constants. Combining Eqs. (6), (7), (8) and (10), the expressions of displacement and stress components are obtained as follows:

$$u_x(x,\ y) = -\sum_{m=1}^{\infty}\left[A_m\alpha e^{\alpha y} + B_m(\alpha y+1)e^{\alpha y} - C_m\alpha\,e^{-\alpha y} - D_m(\alpha y-1)e^{-\alpha y}\right]\alpha\sin\alpha x \tag{11a}$$

$$u_y(x,\ y) = -\frac{1}{(1+\mu)}\left[\sum_{m=1}^{\infty}\left\{\begin{matrix}-A_m(1+\mu)\alpha^2e^{\alpha y} + B_m(-\alpha y-\mu\alpha y-2\mu+2)\alpha e^{\alpha y}\\ -C_m(1+\mu)\alpha^2e^{-\alpha y} + D_m(-\alpha y-\mu\alpha y+2\mu-2)\alpha e^{-\alpha y}\end{matrix}\right\}\cos\alpha x + 6K(1-\mu)y\right] \tag{11b}$$

$$\sigma_{xx}(x,\ y) = -\frac{E}{(1+\mu)^2}\left[\sum_{m=1}^{\infty}\left\{\begin{matrix}A_m\alpha(1+\mu)e^{\alpha y} + B_m(\alpha y+\mu\alpha y+3\mu+1)e^{\alpha y} -\\ C_m\alpha(1+\mu)e^{-\alpha y} + D_m(-\alpha y-\mu\alpha y+3\mu+1)e^{-\alpha y}\end{matrix}\right\}\alpha^2\cos\alpha x + 6\mu K\right] \tag{11c}$$

$$\sigma_{yy}(x,\ y) = -\frac{E}{(1+\mu)^2}\left[\sum_{m=1}^{\infty}\left\{\begin{matrix}A_m\alpha(-1-\mu)e^{\alpha y} + B_m(-\alpha y-\mu\alpha y-\mu+1)e^{\alpha y} +\\ C_m\alpha(1+\mu)e^{-\alpha y} + D_m(\alpha y+\mu\alpha y-\mu+1)e^{-\alpha y}\end{matrix}\right\}\alpha^2\cos\alpha x + 6K\right] \tag{11d}$$

$$\sigma_{xy}(x,\ y) = -\frac{E}{(1+\mu)^2}\left[\sum_{m=1}^{\infty}\left\{\begin{matrix}A_m(1+\mu)\alpha e^{\alpha y} + B_m(\alpha y+\mu\alpha y+2\mu)e^{\alpha y} +\\ C_m(1+\mu)\alpha e^{-\alpha y} + D_m(\alpha y+\mu\alpha y-2\mu)e^{-\alpha y}\end{matrix}\right\}\alpha^2\sin\alpha x\right] \tag{11e}$$

Now, the loading (reaction) on the bottom boundary (y = 0) can be taken as Fourier series in the following manner:

$$\sigma_{yy}(x,0) = 4P/W = E_0 + \sum_{m=1}^{\infty} E_m \cos \alpha x \quad \text{for } \; 0 \le x \le 0.1L \; \text{ and } \; 0.9L \le x \le L \qquad (12)$$

where, $E_0 = \frac{4}{5}(P/W)$ and $E_m = \frac{8(P/W)}{m\pi}\left\{\sin\left(\frac{m\pi}{10}\right) + \sin(m\pi) - \sin\left(\frac{9m\pi}{10}\right)\right\}$; m = 1,2,3, ……. ∞

Similarly, the uniform loading on the top boundary (y = D) can also be expressed by the following Fourier series:

$$\sigma_{yy}(x, D) = (P/W) = I_0 + \sum_{m=1}^{\infty} I_m \cos \alpha x \,; \quad \text{for } \; 0.1L \le x \le 0.9L \qquad (13)$$

where, $I_0 = \frac{4}{5}(P/W)$ and $I_m = \frac{2(P/W)}{m\pi}\left\{\sin\left(\frac{9m\pi}{10}\right) - \sin\left(\frac{m\pi}{10}\right)\right\}$; m = 1,2,3, ……… ∞

Now, attempt is made to satisfy the boundary conditions of the top and bottom boundaries of the beam. Substituting the appropriate values for σ_{yy} and σ_{xy} in Eqs. [11(d) and (e)] for the boundaries, y = 0 and D, we obtain the following four equations in terms of the four unknowns, as

$$\frac{E\alpha^2}{(1+\mu)^2}\left[(1+\mu)\,\alpha A_m + 2\mu B_m + (1+\mu)\,\alpha C_m - 2\mu D_m\right] = 0 \qquad (14a)$$

$$\frac{E\alpha^2}{(1+\mu)^2}\left[A_m(1+\mu)\alpha + B_m(-1+\mu) - C_m(1+\mu)\alpha + D_m(-1+\mu)\right] = E_m \qquad (14b)$$

$$\frac{E\alpha^2}{(1+\mu)^2}\left[A_m(1+\mu)\alpha e^{\alpha D} + B_m(\alpha D + \mu\alpha D + 2\mu)e^{\alpha D} + C_m(1+\mu)\alpha e^{-\alpha D} + D_m(\alpha D + \mu\alpha D - 2\mu)e^{-\alpha D}\right] = 0 \qquad (14c)$$

$$\frac{E\alpha^2}{(1+\mu)^2}\left[A_m(1+\mu)\alpha e^{\alpha D} + B_m(\mu\alpha D + \alpha D + \mu - 1)e^{\alpha D} - C_m(1+\mu)\alpha e^{-\alpha D} - D_m(\mu\alpha D + \alpha D - \mu + 1)e^{-\alpha D}\right] = I_m \qquad (14d)$$

From Eqs. (11d) and (12), it is found that $K = -\left\{2(P/W)(1+\mu)^2\right\}/(15E)$

The above four algebraic equations (14) can readily be solved simultaneously to obtain the four unknowns , namely, A_m, B_m, C_m and D_m, which are then substituted in Eqs. (11) for subsequent finding of stresses and displacements in the beam.

5. RESULTS AND DISCUSSION

The analytical solutions of displacement and stress components are obtained for various aspect ratios (L/D) of the beam. The result presented here is of a guided steel beam (μ = 0.3 and E = 209 GPa) having L/D = 3 and the uniform loading parameter, P = 40 N/mm. The displacement potential solutions are then compared with those of the classical bending theory as well as finite element method (FEM).

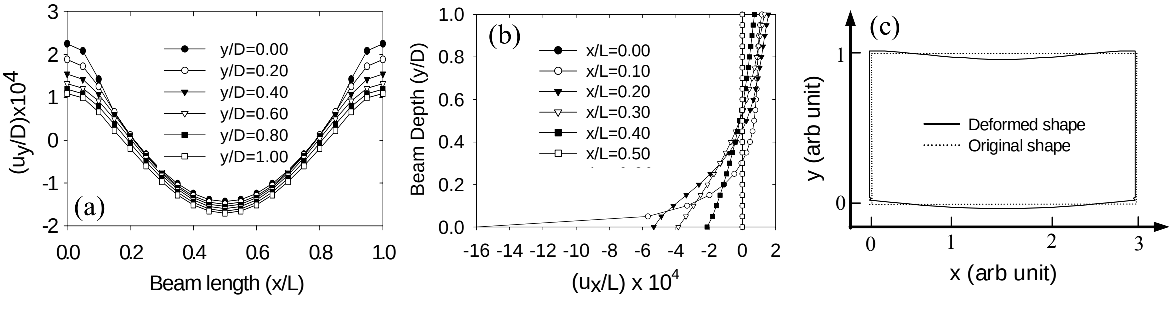

Fig. 2 Displacements and deformed shape of the deep beam, L/D = 3: (a) lateral displacement, (b) axial displacement, (c) deformed shape (magnification factor ×100)

5.1 Solution of Displacements

Axial displacements (u_x) are found negative for sections $0<x/L< 0.5$ and positive for $0.5<x/L<1.0$ with the maximum magnitudes at $x/L = 0.1$ and 0.9, where the loads terminate from both sides of the beam [see Fig. 2(a)]. Axial displacements are found to be symmetric about the mid-horizontal plane, where the displacements are zero, as shown in Fig. 2(a). As appears from Fig. 2(b), lateral displacements (u_y) near the two lateral ends are found to take positive value because of the supports at the bottom boundary, and for the region $0.2<x/L< 0.8$, displacements are negative, which conforms to the physical model of the beam. Fig. 2(c) presents the deformed shape of the beam together with the original shape, which is again in excellent agreement with the applied loading and support of the beam.

5.2 Solution of Stresses

Bending stress distribution is more or less non-linear over the whole span (Fig. 3(a)). This non-linearity increases towards the guided ends. The stress (σ_{xx}) maximizes at the top and bottom edges of the beam but carries opposite sign. Near the guided ends, σ_{xx} is positive for the upper half and negative for the lower half of the beam, but the opposite is observed for sections away from the support. Fig. 3(b) reveals that the normal stress (σ_{yy}) gets its highest value around the position of supports on the bottom edge. For the loaded region, normalized value of the normal stress varies from zero to unity, which is in agreement with the applied loading. Four edges and mid-span section are found free from shearing stress [see Fig. 3(c)]. The distributions of shearing stress (σ_{xy}) conform to the standard parabolic profile except that at sections x/L= 0.1 and 0.9, *i.e.*, the termination point of loading (see Fig. 1).

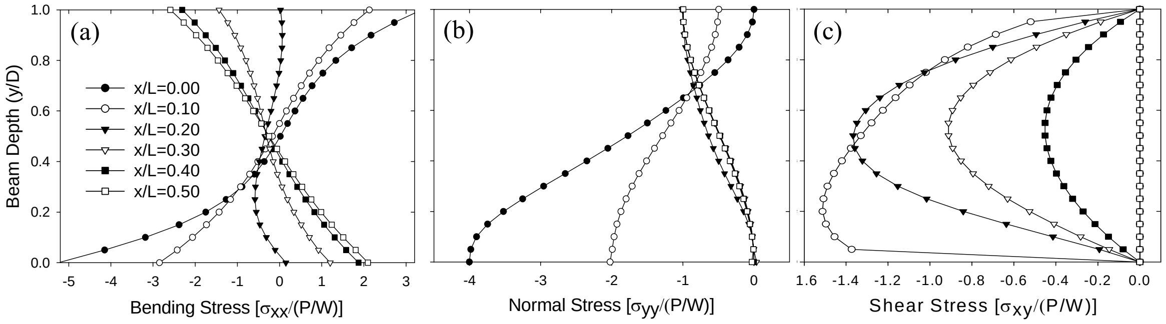

Fig. 3 Distribution of different stress components at different sections of the beam (L/D=3): (a) bending stress, (b) normal stress and (c) shear stress

5.3 Comparison of Results

The present beam problem with its guided ends cannot be solved by the classical beam theory. However, for the sake of comparison, the elementary solutions are obtained for the unguided deep beam. Since the distribution of reaction at the bottom surface cannot be addressed appropriately using the elementary theory, the beam is considered here to be simply supported taking the resultant of the reaction forces. The solutions for the lateral deflection, bending stress and shear stress as obtained by the elementary theory are as follows:

$$u_y(x) = \frac{x}{2E}\left(\frac{P}{W}\right)\left(\frac{L}{D}\right)^3\left[2\left(\frac{x}{L}\right)^2 - \left(\frac{x}{L}\right)^3 - 1\right] \tag{15}$$

$$\sigma_{xx}(x) = 6\left(\frac{P}{W}\right)\left(\frac{L}{D}\right)^2\left[\left(\frac{x}{L}\right)^2 - \left(\frac{x}{L}\right) + \frac{1}{25}\right]\left(\frac{1}{2} - \frac{y}{D}\right) \tag{16}$$

$$\sigma_{xy}(x) = 6\left(\frac{P}{W}\right)\left(\frac{L}{D}\right)\left[\frac{1}{4} - \left(\frac{y}{D} - \frac{1}{2}\right)^2\right]\left(\frac{1}{2} - \frac{x}{L}\right) \tag{17}$$

Figure 4 presents the comparison of the present ψ-solution with those obtained by the elementary theory and finite element method (FEM). FEM solutions are obtained using the standard facilities of the commercial software ANSYS. As appears from Fig. 4(a), the deflection is over predicted by the elementary, whereas that of FEM is very close to the present solution. The bending stress distribution obtained by the elementary theory gives a linear variation over the beam depth. The bending stress is also over predicted by the elementary theory from those of the ψ-solution and the corresponding FEM solution [Fig. 4(b)]. The shear stress distribution at section of x/L = 0.25 [Fig. 4(c)] obtained by the three approaches is found to be very close to each other. But the solutions differ at section x/L = 0.1, where the loadings on the two boundaries terminate. The elementary theory cannot address the local effect of load termination on shear stress, whereas the present ψ-solution is free from such limitations and provides reliable and accurate results at any section of the guided beam.

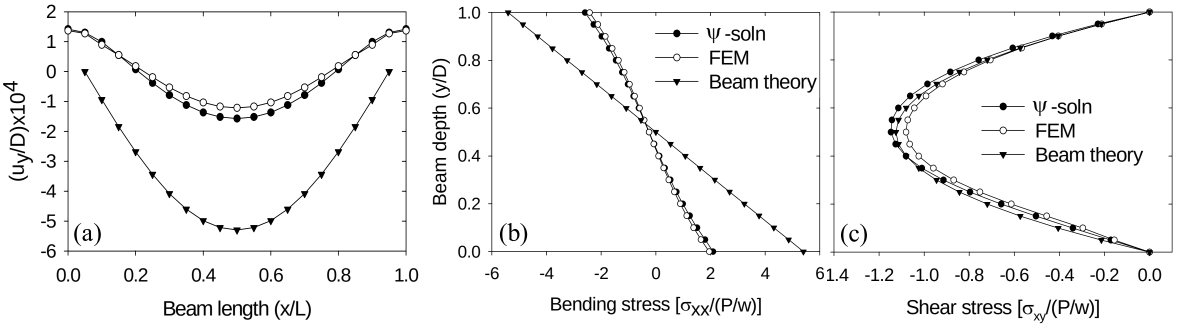

Fig. 4 Comparison of present solutions with those of classical beam theory and FEM: (a) lateral displacement [y/D=0.5], (b) bending stress [x/L=0.5], (c) shear stress [x/L=0.25]

6. Conclusions

Analytical solution of the elastic field of a guided deep beam is investigated using displacement potential approach. The solution of the present mixed boundary-value elastic problem is obtained by satisfying all the physical conditions of the beam appropriately. The guided ends of the beam are identified to be the most critical sections in terms of stresses, although the shear stress field of the beam is found to be similar to that of the corresponding unguided beam. The comparative study reveals that the classical theory of bending is simply inadequate to predict the stress and displacements fields of the guided beam, however, the solutions obtained by FEM are found to approach towards the analytical solution far better than that of classical theory.

References

[1] Chow, L., Conway, H.D., and Winter, G., Stresses in Deep Beams, Trans ASCE, 2557, (1952).

[2] Conway, H.D., Chow, L., and Morgan, G.W., Analysis of deep beams, J. of Applied Mechanics, Trans ASME 18(2), 163–172 (1951).

[3] Parker, D.F., The role of Saint-Venant’s Solutions in rod and beam theories, J. of Applied Mechanics, Trans ASME 46, 861–866 (1979).

[4] Murty, A.V.K., Towards a consistent beam theory, AIAA Journal, 22, 811–816 (1984).

[5] Suzuki, S., Stress analysis of short beams, AIAA Journal, 24, 1396–1398 (1986).

[6] Durelli A.J., and Ranganayakamma, B., Parametric solution of stresses in beams, J. of Engineering Mechanics 115(2), 401–414 (1989).

[7] Hardy, S.J., and Pipelzadeh, M.K., Static analysis of short beams, J. of Strain Analysis, IMechE, 26, 15-29 (1991).

[8] Timoshenko, S.P., and Goodier, J.N., Theory of Elasticity, 3rd ed., McGraw-Hill (1970).

[9] Ahmed, S.R., Idris, A.B.M., and Uddin, M.W., Numerical solution of both ends fixed deep beams, Computers & Structures 61(1), 21–29 (1996).

[10] Ahmed, S.R., Khan, M.R., Islam, K.M.S., and Uddin, M.W., Investigation of stresses at the fixed end of deep cantilever beams, Computers & Structures 69, 329–338 (1998).

[11] Ahmed, S.R., Nath, S.K.D., and Uddin, M.W., Optimum shapes of tire treads for avoiding lateral slippage between tires and roads, Int. J. Numer. Meth. Engng., 64, 729-750 (2005).

Proceeding of the 4th **BSME-ASME** International Conference on Thermal Engineering
27-29 December, 2008, Dhaka, Bangladesh

THE ANALYSIS OF THE BEHAVIORS OF A CIRCULAR ARCH

Jaegwi Go, Jeong Il Song

School of Mechatronics
Changwon National University
#9 Sarim-dong, Chagnwon
641-773, GeyoungNam, Korea(ROK)
e-amil:jggo@changwon.ac.kr

ABSTRACT

The balance of forces of an elemental length is considered to establish the governing equation. Equilibrium states are investigated numerically for various opening angles and boundary conditions. The boundary problem is solved by shooting method using iteration based on the Runge-Kutta, and some of equilibria are displayed. Using the pressure-base angle and pressure-base curvature plots the variations of angle and curvature versus pressure are visualize.

KEYWORDS: *Buckling, Equilibrium state, Non-uniqueness, Snap-through.*

1. INTRODUCTION

We concern with the nonlinear equations governing the buckled states of elastic, inextensible, and thin circular arches subjecting a uniform normal pressure. The arches are restrained at the bases(Fig. 1), which could represent a cross section of a thin shell. With the pressure larger than a critical pressure the arches may buckle or deviate from its circular shape. If the pressure is further increased, large nonlinear deformations of the arches occur.

The buckling of such a classical arch has been studied by Timoshenko and Gere[4], Vlasov[5], and Simitses[3]. They found that the buckling pressure depends on the flexural rigidity, the opening angle, and bases conditions(hinged or clamped). Dickie and Broughton[1] performed the buckling of shallow circular fixed and pin-ended arches and used a series method to obtain approximate numerical method. An energy method was used by Pi, Bradford, and Uy[2] to derive analytical solutions for the buckling load and proposed approximations for symmetric buckling of shallow circular fixed and pin-ended arches. In the present paper we observe the buckling pressures and the bifurcation curves for symmetrically and anti-symmetrically deformed shapes. The variations of angle and curvature versus pressure are displayed for various opening angles and general bases conditions.

2. DERIVATION OF GOVERNING EQUATION

The balance of the forces in the normal and tangential directions (Fig. 2) gives

$$Tdg - dS - q'_n \, ds' = 0, \qquad (1)$$

$$dT + Sdg = 0, \qquad (2)$$

$$dM - Sds' = 0. \qquad (3)$$

Now, we assume that the thickness of arches is thin enough such that the local curvature is proportional to the local moment. The elastica assumption thus gives

$$M = EI\frac{dg}{ds'}$$

(4)

The combination of the equations (1), (2), (3), and (4) provides

$$EI\frac{d^4g}{ds'^4}\frac{dg}{ds'} - EI\frac{d^3g}{ds'^3}\frac{d^2g}{ds'^2} - q_n'\frac{d^2g}{ds'^2} + EI\frac{d^2g}{ds'^2}\left(\frac{dg}{ds'}\right)^3 = 0\,. \qquad (5)$$

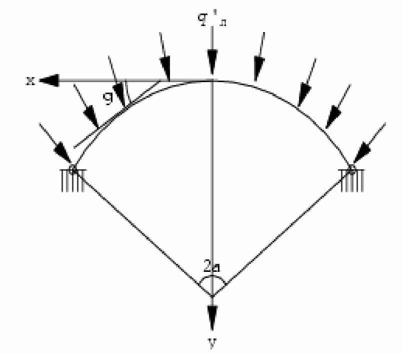

Fig. 1 Uniform normal load around arch.

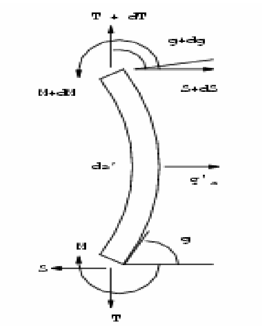

Fig. 2 An elemental length.

Using the non-dimensional variables: $s = \frac{s'}{R}$, $q_n = \frac{q_n'}{EI}R^3$, the following normalized nonlinear equation is obtained:

$$g_{ssss}g_s - g_{sss}g_{ss} - q_n g_{ss} + g_{ss}{g_s}^3 = 0. \qquad (6)$$

For the general boundary conditions, we assume that the bases of the arch are restrained with torsional spring. Then the total angle change is resisted by an additional moment at the bases with torsional spring constants, that is,

$$\tau'(g(-a)+a) - EI(g_s'(-a) - \frac{1}{R}) = 0$$

$$\tau'(g(a)-a) + EI(g_s'(a) - \frac{1}{R}) = 0\,. \qquad (7)$$

Again using the non-dimensional variables; $s = \frac{s'}{R}$, $q_n = \frac{q_n'}{EI}R^3$, the normalized boundary conditions are given by

$$(g(0)+a) - \tau(g_s(0) - 2a) = 0$$

$$(g(1)-a) + \tau(g_s(1) - 2a) = 0\,, \qquad (8)$$

where $\tau = \frac{EI}{\tau' R}$. The condition $\tau = 0$ implies the fixed bases condition, and $\tau = \infty$ implies the hinged bases condition. We note that the normalized Cartesian coordinates (x, y) are related to g by

$$\frac{dx}{ds} = x_x = \cos g(s)\,, \qquad \frac{dy}{ds} = y_x = \sin g(s)\,. \tag{9}$$

3. NMERICAL RESULTS AND DISCUSSION

We solve the boundary problem by shooting method using iteration. Figure 3 shows slight deflection for small loads. Stable equilibrium positions for various angles with large pressure are displayed in figure 4. The shapes are squeezed up under the slight pressure and the arches are bent down with large loads. In figure 5, equilibrium shapes for arches with hinged bases are displayed. The solutions are found only in the first bifurcation state.

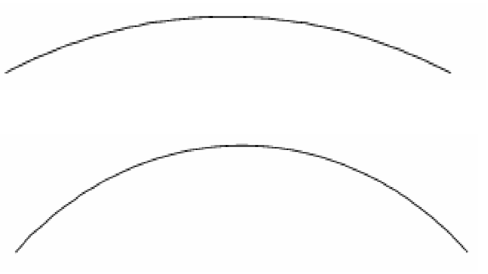

Fig. 3 Slight deflection with clamped bases.

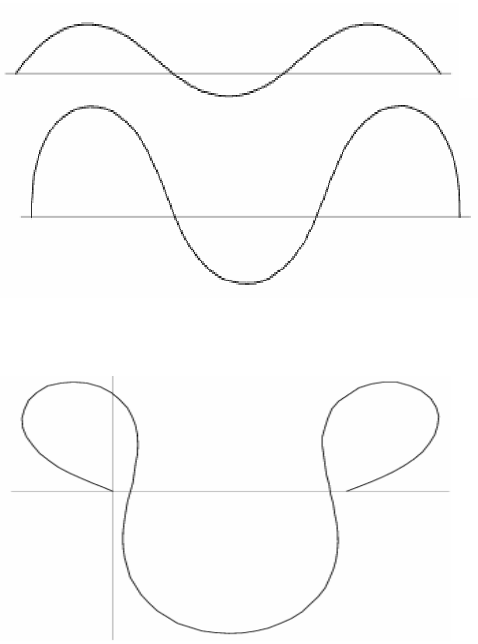

Fig. 4 Large deflection with clamped bases.

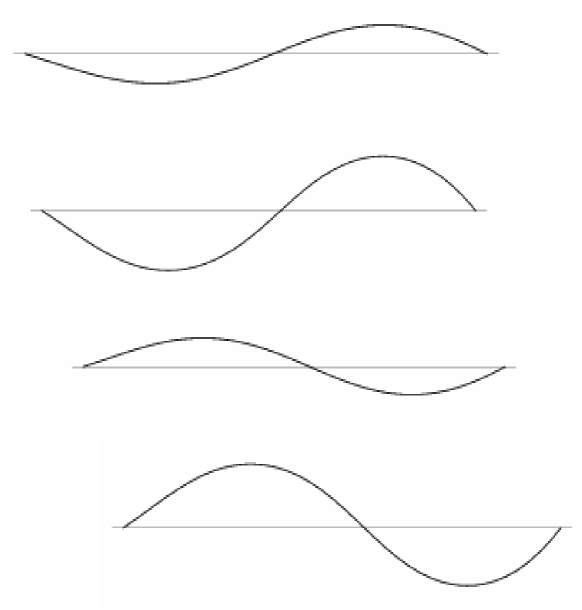

Fig. 5 Large deflection with hinged bases.

Figure 6 shows the variation of a base's angle versus the uniform pressure p to the hinged bases arch. The figure displays a pressure-base angle plot. For the angle $a = \frac{\pi}{4}$, *snap-trough* phenomenon appears. In the figure, the branches ***C*** and ***E*** represent symmetrically deformed shapes and the branches ***D*** and ***F*** represent anti-symmetrically deformed shapes. Figure 7 shows the variation of a base's curvature to the arch with clamped bases displaying a pressure-base curvature plot. The angle $a = \frac{\pi}{2}$ is used and similar results to hinged bases arch are obtained. The open curve implies the symmetrically deformed shapes while closed curve represents the anti-symmetrically deformed shapes.

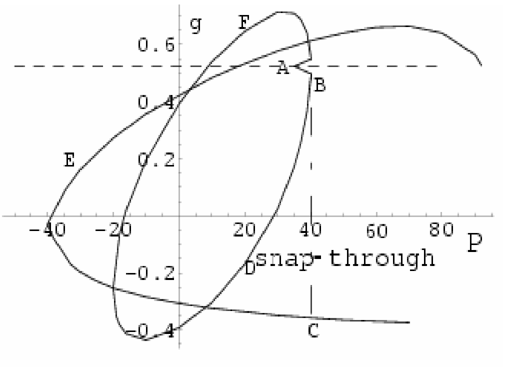

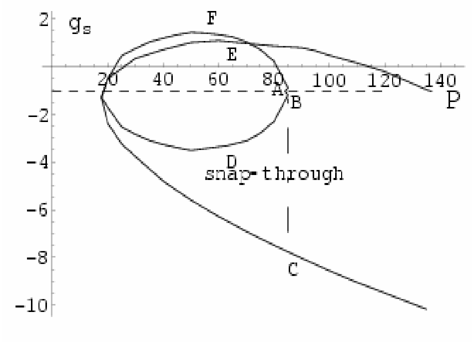

Fig. 6 The variation of angle : $a = \frac{\pi}{4}$, $\tau = \infty$. **Fig. 7 The variation of curvature** : $a = \frac{\pi}{2}$, $\tau = 0$.

4. CONCLUSION

Many previous works showed the shape of bifurcation curve for an arch was a pitchfork. But, the development of deflection in practice is discontinuous and the arch is abruptly turned inside out at some large load in symmetric mode. Y.-L. Pi, M.A. Bradford, and B. Uy [2] improved previous work investigating the process of angle change at the middle point of arch. However, it is still hard to explain the discontinuous change of angle with their results even though our results agree partially with previous result of Y.-L. Pi, M.A. Bradford, and B. Uy. The figures displayed the variations of angle and curvature illustrated the discontinuity through the snap-through phenomenon.

The buckling of a thin circular arch is complex. In this thesis we have advanced in some areas and in depth interesting problems such as bifurcation, non-uniqueness, and snap-through. In spite of these results, some extensions of the thesis by relaxing the assumption of inextensibility need to be necessary to approach practical physical problem.

5. NOMENCLATURE

T	: tension	S	: shear stress
s'	: arch length	τ'	: spring constant
M	: bending moment	q'_n	: normal stress
EI	: flexural rigidity	$2a$	: opening angle
R	: radius of arch	g	: local angle of inclination

6. REFERENCES

[1] R.W. Dickey and P. Broughton, Stability Criteria For Shallow Arches, Journal of Engineering Mechanics Division ASCE 97. (EM3), PP.951-965, 1971.
[2] Y.L. Pi, M.A. Bradford, and B. Uy, In-Plane Stability Of Arches, Inter. J. Solids and Structures, Vol. 39, 2002, pp. 105-125, 2002.
[3] G.J. Simitses, Elastic Stability Of Structures, Prentice-Hall, New Jersey, 1976.
[4] S.P. Timoshenko and J.M. Gere, Theory Of Elastic Stability, McGraw-Hill Second Edition, 1961.
[5] V.Z. Vlasov, Thin-Walled Elastic Beams, 2nd Edition, Israel Programme For Scientific Translation, Jerusalem, Israel, 1963.

Proceedings of the 4th BSME-ASME International Conference on Thermal Engineering
27-29 December, 2008, Dhaka, Bangladesh

ELECTRICAL PROPERTIES OF PALM FIBER REINFORCED PVC COMPOSITES

Halima Akter[1], M. A. Gafur[2], and Md. Abu Hashan Bhuiyan[1]
[1]Dept. of Physics, BUET, Dhaka-1000, and [2]PP&PDC, BCSIR, Dhaka-1205, Bangladesh

ABSTRACT

PVC-Palm fiber reinforced composites were fabricated using a simple hot press molding method. The effect of fiber addition on electrical properties were evaluated. The DC electrical measurements on PVC and PVC-palm fiber composites were performed as functions of voltage, temperature and palm fiber addition. The current-voltage characteristics of all the composites show an ohmic behavior. Resistivity decreases with the increase of fiber addition and temperature. Activation energy increases with the increases of fiber addition.

Key words: Composites, Resistivity, PVC

INTRODUCTION

Over about three decades composite materials, plastics and ceramics have been the dominant emerging new materials. The volume and number of applications of composite materials have grown steadily by penetrating new markets relentlessly. Modern composite materials constitute a significant proportion of the engineered materials, market ranging from everyday products to sophisticated high-tech applications. While composite have already proven there worth as weight saving material, the current challenge is to make them cost effective. The efforts to produce economically attractive composite components have resulted in several innovate manufacturing techniques currently being used in the composites industries.

Governmental regulations and growing environmental awareness throughout the world have triggered a paradigm shift towards designing materials compatible with the environment. The use of palm fiber, derived from annually renewable source, as reinforcing fibers in both thermoplastic and thermosetting matrix composites provides positive benefits with respect to ultimate disposability and raw material utilization [1]. Recently natural fibers have been used as reinforcement-filler in low melting thermoplastic. Because of lower density, easy processibility, biodegradability and availability in nature, combined with a better cost-performance ratio, cellulosic materials show bright potentiality as a filler in thermoplastics [2,3]. The composites of engineering polymers combined with natural components like wood, flax, hemp, jute etc. are intensively studied due to the ecology and interesting physical properties of such natural cellulosic materials[4,5]. Natural fibers such as jute, coir, palm, wood fiber palm fiber, banana etc. are used as an alternative to synthetic fibers e.g. glass, aramid, carbon, etc. These fibers are used due to : their renewable character, acceptable specific strength properties, low cost, enhanced energy recovery, and biodegradability. Natural fiber reinforced polymer combine good mechanical properties with low specific mass. The palm fiber can be used as reinforcing agent in thermoplastics like polyethylene (PE), polypropylene (PP), poly vinyl chloride(PVC), etc. The use of palm fiber and their effects on properties are not well documented. The objective of the study is to find the effect of palm fiber addition on the properties of PVC-Palm fiber composites.

2. EXPERIMENTAL PROCEDURE

2.1 Raw Materials

Palm fiber were colleted in the following way – the palm leaves were cut from the tree, then the diving end of the middle hard part of the leaf are hammered, kept in water for 20 days. After that the rotten materials are washed and fibers are collected and sun dried. From these fibers, short fibers having size of 2 mm are taken for composite preparation. Table 1 shows chemical composition of palm fiber.

Table 1 Chemical Composition of Palm Fiber

Contents	Amount (wt%)
Lignin	27.30
Hemicellose	30.9
Alpha celluose	38.4
Others (wax, Pectin, etc.)	3.4

2.2 Fabrication

The composite preparation was done using a 450 KN Weber-Press. The press is consisted of pressing, heating and cooling system. Palm fiber and polymer are kept at 105^0C for 24 hours for drying . A blender was used to mix the PVC and palm fiber for 2 minute at 400 rpm. The mixtures were taken in die after using a little amount of mold releasing agent. The heating temperatures and initial pressure were set at 120^0 C and 50KN, respectively. After reaching the set temperature, the holding time was taken 1 hour 45 minutes. Then pressure was increased up to 100KN and stopped the heating system. Then the system was allowed to cool.

2.3 Measurement of properties

2.3.1 Electrical measurements

Silver paste coated sample was placed in between the electrodes inside the specimen chamber. The chamber was evacuated using a rotary vacuum pump to about 10^{-2}Pa. Then a 614 Keithley electrometer, Microvolt meter (MVM) (Model197A) and stabilized D.C. Power supply were connected in series with the specimen to record the D.C. current through the sample, the electrometer was set to current mode. The meter was warmed up to one hour.

2.3.1.1 Current –Voltage (I – V) measurement

A Keithley 614 electrometer for different sample and an MVM keithley (Model 197A) was set in the current mode for recording the current through the sample at different applied voltages at a constant temperature. In this case the voltage was varied from 0 to 120 V. The current was recorded every 5 V intervals.

2.3.1.1 Current –Temperature (I – T) measurement

The electrometer was set in current mode for the direct measurement of current at different temperatures at a constant voltage. To raise the temperature, the specimen chamber was heated by a heating coil, which can be easily wrapped around the specimen chamber. The sample current was measured at every 0.1 volt increase of thermocouple reading. The above procedures of I-T measurement were applied for every sample to investigate the current change.

3. RESULTS AND DISCUSSION

3.1 Electrical Properties:

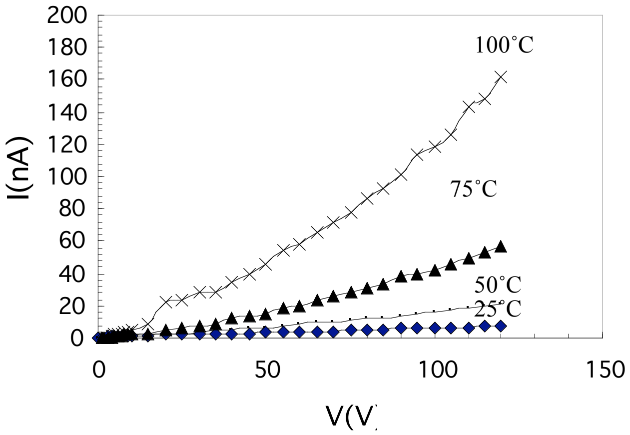

Figure 1 Effect of temperature on I-V characteristics of PVC.

Figure 1 to .4 show the effect of temperature on I-V characteristics of PVC-Palm fiber composites having 0, 5, 10, and 15(wt %) palm fiber respectively. Here with the increases of voltage and temperature, current increases almost linearly. For room temperature the value of

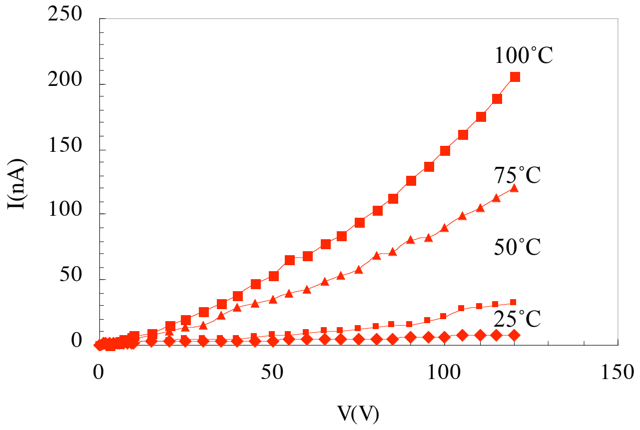

Figure 2 Effect of temperature on I-V characteristics of PVC-palm fiber 5(wt.%) composites.

n is 0.70 (0% sample), 0.78 (5% sample), 0.92 (10% sample), 0.94 (15% sample). So it is observed that the slope is found to be 0.70-0.94. This can be roughly taken in unity. So the contact does not have any effect on the measured electrical properties. Similar results were found on PP-bijoypur white clay composites [6].

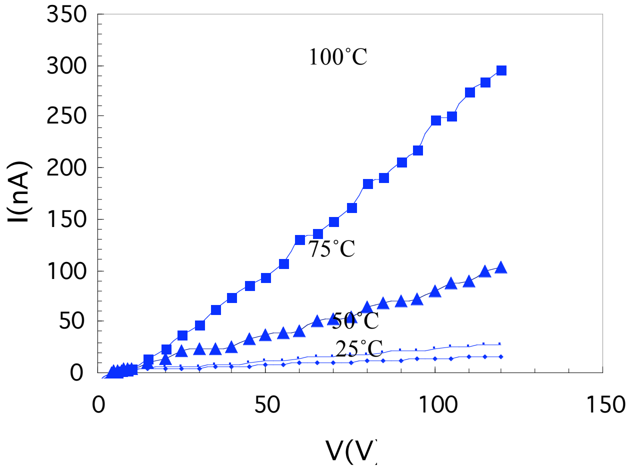

Figure 3 Effect of temperature on I-V characteristics of PVC-palm fiber 10(wt.%) composites.

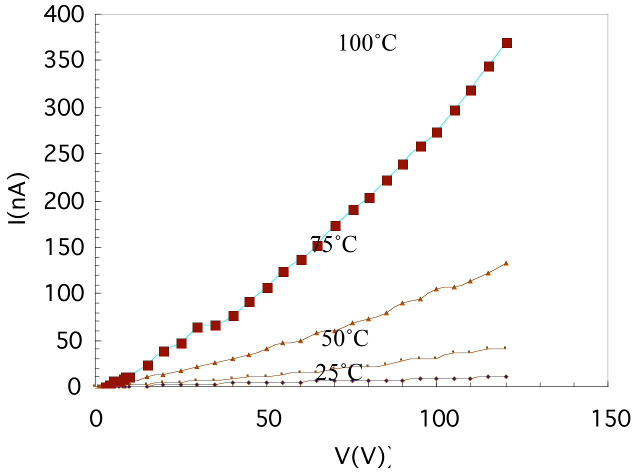

Figure 4 Effect of temperature on I-V characteristics of PVC-palm fiber 15(wt.%) composites.

Figure 5 shows the effect of temperature on current of PVC-Palm fiber composites with an applied voltage of 100V. It reveals that with the increase of both temperature and fiber addition, current increases. It is noted that the current increases rapidly as temperature rises. The addition of palm fiber in PVC may significantly increase the electrical conductivity. It is seen that the dc electrical conductivity of the composites increases as the concentration of fiber increases. It might be due to increase of polar groups in the composites, dipole

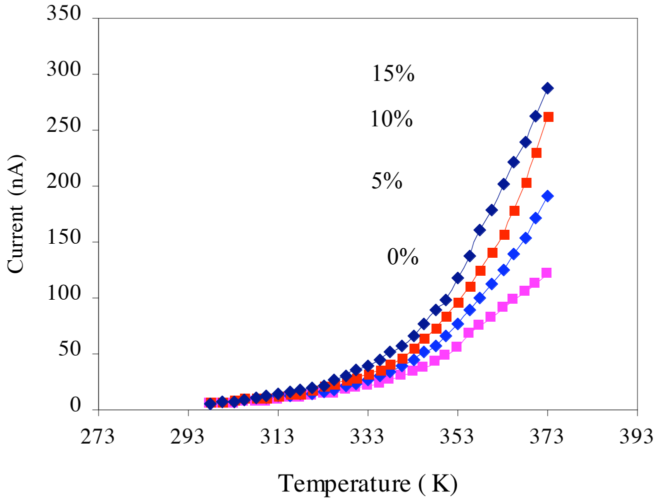

Figure 5 shows the effect of temperature on current of PVC-Palm fiber composites.

originating from the presence of asymmetric excess electron in the polymers. So it is obvious that as the polar molecules concentration increases, the number of electrical charge carriers increase resulting in higher conductivity [7].

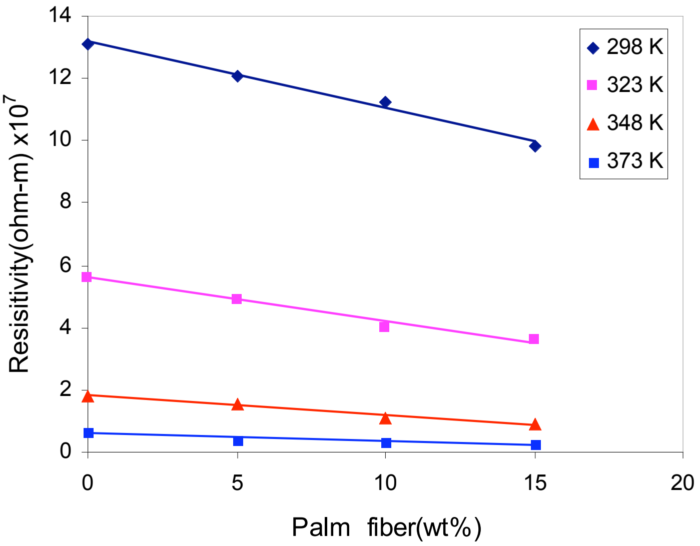

Figure 6 Effect of fiber loading on resistivity.

Figure 6 shows the effect of palm fiber loading on the resistivity of the composites. It reveals that with the increase of fiber addition and temperature resistivity decreases. Because of more ionic mobility, resistivity of the composite decreases as palm fiber content increases. Introduction of palm fibers in PVC creates lot of defects in PVC-palm fiber composites. These defects help electronic movement in the composite.

Figure 7 shows the LogI-1/T for PVC-Palm fiber composites. The activation energy is calculated from this graph. Activation energy increases with the increase of fiber content. For 0% fiber addition, activation energy is 0.42eV. 5% fiber addition activation energy is 0.45eV. 10% fiber addition activation energy is 0.47eV. 15% fiber addition activation energy is 0.51eV. The increase of the activation energy of the composites with increases palm fiber content may be due to the restriction of ion jump for higher concentration of fiber in PVC. The conduction in these materials may be due to ionic motion.

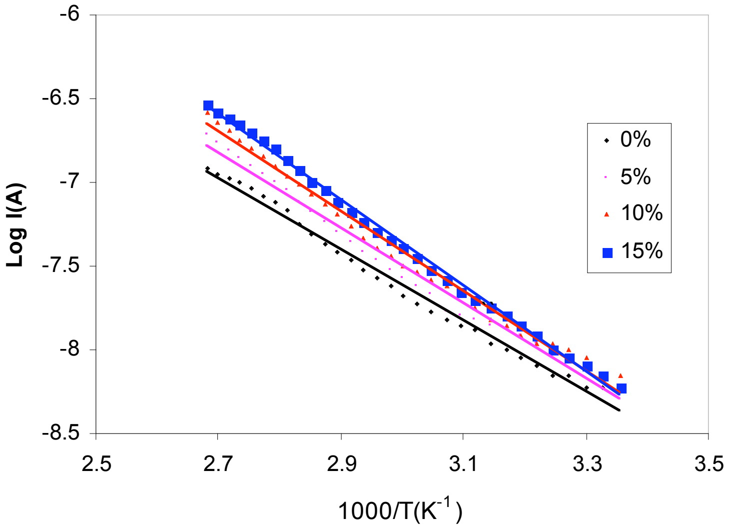

Figure 7 LogI-1/T for PVC-palm fiber composites.

Table 1 Activation energy (eV) for different PVC-palm fiber composites

Composite samples Palm fiber (wt %)	Activation energy (eV)
0	0.42
5	0.45
10	0.47
15	0.51

CONCLUSIONS

From the I-V characteristics it is evident that the contact behavior is ohmic. Resistivity decreases with the increase of fiber content and temperature. The Electronic conduction in these materials may be due to inonic motion. The activation energy increases with the increases of fiber addition.

REFERENCES

[1] Mohanty, A. K. , Mubarak, A. Khan, Shaoo, S. and G. Hinrichen, Effect of chemical Modification on the performance of Biodegradable jute yarn-Biopol composites, J. Material Science 35 (2000)2598.

[2] Woodhams, R.T., Thomas, G.and Rodgeers, D.K, Polym.Engi.Sci 24(15).1166-1171(1984).
[3] Mckenjie, A.W.and Yuritta ,J.P., Appita, 32(6), 460-465(1979).
[4] Bledzki, A.K., and Gassan, J., Natural fiber reinforced plastics in Handbook of Advanced Polymeric materials, Marcel Dekker Publishers, New Jersey(USA)1997.
[5] Quillin, D.T., Caulfield, D.F., and Koulsky, J.A, .J. Appl.Polym.Sci,(1993),50,1187
[6] Razzak A. Bhuiyan A. H.,"DC electrical conduction mechanism in polypropylene bijoypur white clay (PP-BWC) composites", Ind. J. Phys. 77A (4), 353-357, 2003.
[7] Islam M. N., Bagom J., Gafur M. A. and Khan A. H., "Development, structure and strength properties of PP/jute blends", Jahangirnagar University, J. Sci., 30, 89-106, 2007.

Proceedings of the 4th BSME-ASME International Conference on Thermal Engineering
27-29 December, 2008, Dhaka, Bangladesh

COMPUTAIONAL STUDY OF DIFFERENT FACTORS IN NO_X FORMATION

Waseem Amjad[1],Imtiaz Hussain[1] and In-Lim Gweon[1]

[1]Combustion Engineering Lab. Mechanical Department Myong-Ji University South-Korea

Email: shah_waseem@hotmail.com

ABSTRACT

NOx formation during the combustion process occurs mainly through the oxidation of nitrogen in the combustion air (thermal NOx) and through oxidation of nitrogen with the fuel (prompt NOx). In this paper a numerical simulation is carried out to investigate one of the way to reduce the thermal NOx by the increase of the flame lift-off length for the lowering of peak flame temperature which is considered the main cause of thermal NOx. The flame lift-off length was analysed by temperature contours and this length is influenced by the here studied factors, fuel injection velocity, gas pressure, air temperature,fuel type. Different orifice diameters (1.0,0.85,0.65mm) of a injection nozzle used for this purpose using software "FLUENT".The fuel injection velocities were 150,100, 80,50 m/sec. It was observed that the NOx reduced as the flame lift-off length increases with increased injection pressure, decreased orifice diameter, decreased gas pressure (back pressure).

Keywords: *flame lift-off length, NOx formation,high temperature*

1. INTRODUCTION

There are three main resources of its formation during the combustion: prompt NO, fuel NO, and thermal NO. The last one is considered the main source of NOx production. The thermal NO emission mainly caused by the high temperature in the combustion process. So to control the NO, the control of combustion peak temperature at ignition of fuel is key factor. It has been known that the formation of NOx is strongly influenced by the gas temperature so that many attempts to reduce the emission of NOx have been closely related to the reduction of flame temperatures.The fuel spray (in case of oil fuel) and mixing processes (caused by the fuel injection) governs the emission formation[1].Besides the spray formation and ignition, the combustion of the spray is also important. A certain time after start of combustion the diffusion (or mixing controlled) flame will stabilize at a constant distance from the fuel injector nozzle. This distance, from the nozzle orifice to the start of the flame, is called the flame lift-off length. Within this distance, a substantial amount of air is entrained into the spray. Since more entrained air provides locally leaner conditions within the spray [1], less fuel-rich zones that can form soot are created. Hence, the larger the distance, the leaner the spray and less soot formed. A larger flame lift-off length should thus be beneficial.With respect to diesel injection, one of the first flame lift-off length investigations was made in a numerical study in 1994 [2].The flame lift-off length has been investigated in the case of gas jets by several researchers described in [3,4].The results show that, with increased gas injection velocity, the flame lift-off length increases approximately linearly with the velocity.

Some later experimental investigations [5] have used a constant volume chamber in which a premixed gas is combusted in order to generate a hot diesel-like environment into which the diesel fuel is injected and ignited. This paper reports on furnaces, a numerically study of different parameters influencing the flame lift-off length using a constant pressure chamber.

2. COMPUTATIONAL MODEL

Computational model was set up in CFD software FLUENT version 6.3.21 and mesh of the geometrical model was created in GAMBIT 2.2.30 Fig1.Constructal furnace shown in Fig.1 used for analysis having fuel entrance at middle with combustion air entering around it.This feature has two advantages: first, it eliminates the longitudinal temperature increase and second it increases the heat transfer coefficient. Nonpreheated methane/air are fed to their inlets and hot product gases exit the furnace. Due to the aspect ratio, the system is simplified to a 2D one and the plane of symmetry between the two halves of furnace allows simulations of only half of the furnace. A schematic of the system is below,

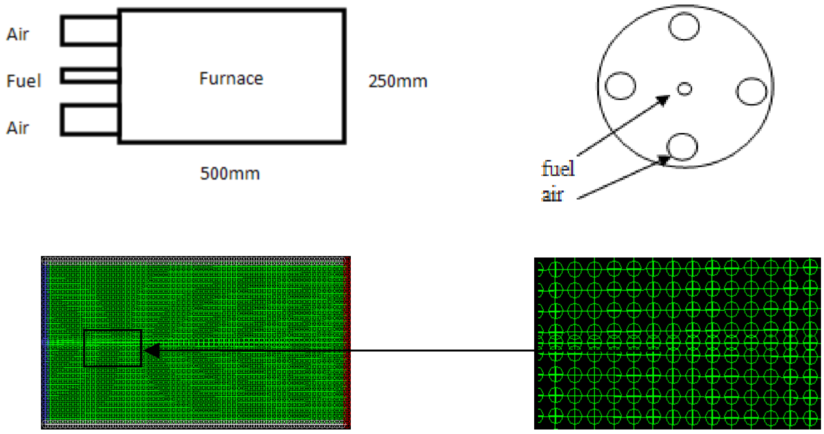

Fig:1 Schematic of the computational domain (2-D) and computational mesh.

3. GRID INDIPENDENCE

In order to assess the effect of number of mesh points on the accuracy of results grid independency done means all three structures of different diameter nozzle having the same configuration of the mesh, as below

Grid Size

Level	Cells	Faces	Nodes	Partitions
0	2100	4295	2196	1

1 cell zone, 6 face zones.

Reordering domain using Reverse Cuthill-McKee method [6].

Bandwidth reduction = 60/35 = 1.71

The steady-state governing equations are solved using a segregated solver, which means that temperature and flow fields are segregated from each other and are solved separately using FLUENT 6.3 software. The conservation equations were solved implicitly with a 2D steady-state segregated solver using an under-relaxation method. The segregated solver first solves the momentum equation, then the continuity equation. As required by problem physics the following equations were introduced and solved using first order upwind discretization scheme (The main advantages are that it is easy to implement and that it results in very stable and also here is no flow gradient).

- Continuity equation
- Energy transport equation
- Turbulence model two transport equation

Tubulence flow was modelled by two equations k-w model [7].This model is advantageous due to its stability during computation [8]. All temperature- dependent properteis of fluids, i.e fuel and air , such as density are avaluated at local temperature by using the least-squrefit equations The intial guesses for temperature and viscosity fields were set to constant value over the entire computaional domain.Boundry conditions were set up as follows:

- Velocity inlet for fuel,
- Velocity inlet for combustion air,
- Pressure out let at the flue gas out let,
- Temperature of combustion air.

The boundary conditions used in this model are as follows. At the inlet of air a fixed flat velocity profile is assumed.For the species and energy equations, Danckwerts boundary conditions are employed [6] i.e., the convective portions of the equations are fixed, A symmetry boundary condition is applied at the centerline between the two halves. At the exit, the pressure is specified and the remaining variables are calculated assuming far-field conditions, i.e., zero diffusive flux of species or energy normal to the exit. Non-uniform node spacing is employed with more nodes in the reaction zone. The number of nodes varies depending on dimensions, but the simplest one consists of 60 axial nodes by 35 transverse nodes, totaling approximately 2100 nodes.One-step chemistries, determined from flame speeds, are a useful tool for describing flame dynamics and flame responses to external perturbations[2].Here a reduced one-step methane combustion chemistry is used that assumes the irreversible combustion of methane:

$$CH4 + 2O2 \rightarrow CO2 + 2H2O$$

Consequently five species, namely CH4, O2, N2, CO2, and H2O, are modeled with corresponding conservation equations. Specifically, the mechanism used is the one proposed by Westbrook and Dryer[9]. We should remark that the one-step approximation fails to describe several aspects, such as the possibility for formation of partial oxidation products CO and H2 and the resulting superadiabatic flame temperature, or the ignition temperature when ignition is kinetically controlled etc. As a result of this approximation, the flame location may be somewhat inaccurate.Therefore, the results presented here should be used as a guide to understand trends rather than an accurate prediction. After an acceptable level of convergence computation of NOx production took place based on the obtained results. As the fact that fuel does not contain any chemically bounded nitrogen, all of the NOx produced is accounted by the two following formation mechanism [10]:

- Thermal (Zeldovich) mechanism and
- Promt mechani

4. RESULTS AND DISCUSSION

4.1 INJECTION VELOCITY

Here the effect of injection velocity has studied. High fuel injection velocity leads to increased kinetic energy. So fuel will penetrate longer in the furnace for certain time [11] during which the fuel evaporates, mixes with the surrounding hot gas and ignite. The diffusion flame will be located further away from the nozzle tip, resulting in a longer flame lift-off length than would be the case with a low injection velocity and cosequently this has effect on lowering NOx value with increase of velocity as in (Fig: 2).

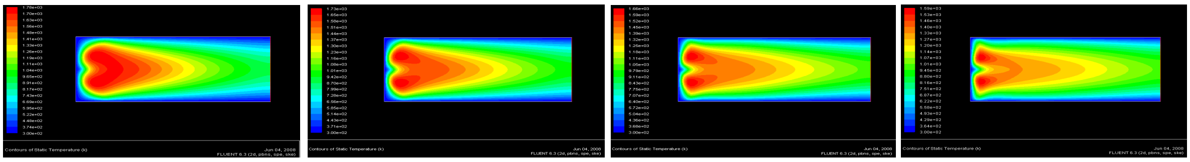

Fig:2 All 1.0mm nozzle diameter flame length can be observed,by increasing velocity the distance of flame start point increase from nozzle. left 50,80, 100,150 m/sec respectively.

Similarly the distribution of EINOX production at different velocities (fig:3). By the rise of injection velocity the most of NOx form forahead from start of furnace than at lower one.The beginning position of NOx formation with different injection velocities, it can see that distance

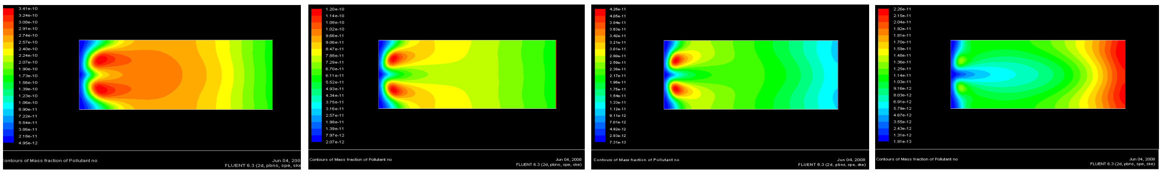

Fig:3 All 1.0mmND (nozzle diameter) NOx distribution can be observed at different velocities. Left side, 50,80,100,150m/sec respectively.

from nozzle for the NO formation is higher for relatively high velocity this leads to avoid the locally rise-up of temperature. So no abruptly rise of temperature not suddenly high formation of NOx, but linearly along the furnace as combustion proceed and then decreasing. These results can also be observed in Fig:4. NOx in the interior of furnace at varying velocity is presented.The maximum(with50m/sec) and minimum (with 150m/sec) value of its formation along the length of furnace can be seen

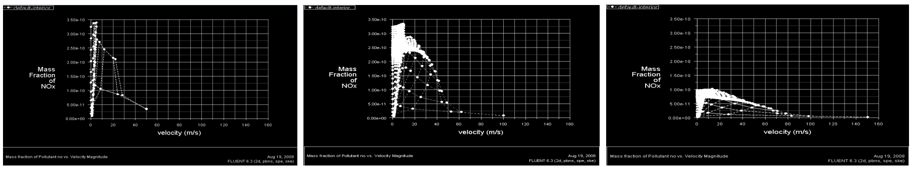

Fig:4 From left side, Distribution of NOx at 50m/sec,at 100m/sec,at 150m/sec

4.2 AIR TEMPERATURE

Results show (Fig.5) that increasing the combustion air temperature cause decrease of flame length as spontaneous burning occur just near the tip of nozzle increasing high locally temperature which is the main cause of NOx formation. Also the density of fuel affected by increasing the temperature of atmosphere around it. The lift off length (of the far-lifted flame is equal or greater than the attached flame length which implies that the local equivalence ratio at the flame base is below unity (fuel lean zone) and all the fuel mixed with the entrained air so no locally high temperature zone occur and for attached flame it is higher than unity (fuel rich zone) [14].

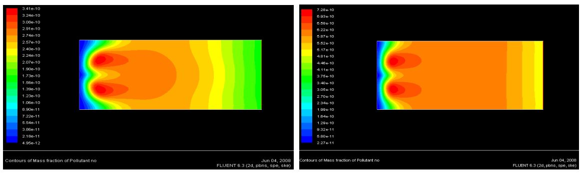

Fig:5 NOx distribution with air temperature 300k(L) air at 600k(R) with 50m/sec,1mm

4.3 FUEL TYPE

Another effect of increased gas density (pressure) is that the ratio between gas density and fuel density increases. So a fuel with a comparative low density will be overcome by that high rise of gas density (pressure), this leads to a wider spray angle that gives the fuel greater exposure towards the surrounding gas (air) [13] and increases the mixing rate between gas and fuel [10]. It also increases the entrainment of gas into the fuel rich spray [10, 15], which leads to shorter ignition delay and which would also result in a shorter flame lift-off length. Velocity contours in the Fig:6 illustrate the penetration of methane and deisel fuel with same injection velocity and nozzle diameter, this support the truth of reduction in thermal NOx with far penetration of fuel into the gas pressure of the furnace. Similerly in the figure distribution of thermal NOx near the nozzle can be compare even in deisel case,the value of NOx with high velocity is lower than that of with low one.

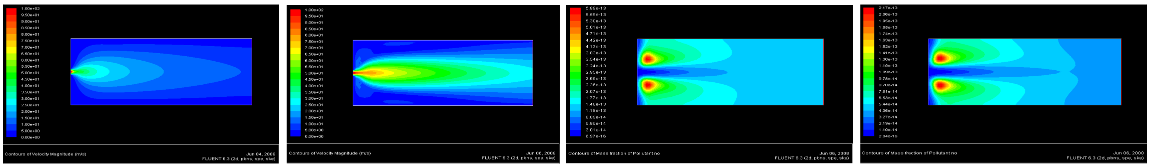

Fig:6 From left first two,Velocity profile of methane and deisel fuel at 100m/sec and nozzle diameter 0.85mm respectively next two for only Deisel,NOx (thermal) with Injection Velocity 50m/sec and 100m/sec with dia.0.65mm respectively.

The results obtained are adding the more facts to the work of Lille [16] to examin of flame length for a gas jet in an industrial furance showing the impact of gas temperature, here the results also obtained by liquid fuel, deisel as the ignitability properties of the deisel fuel can also contribute to a difference in absolute number for the flame lift-off length. In this study fuel is used at its normal temperature as the higher temperature of the surrounding gas leads to an increased enthalpy transport to evaporate and ignite the fuel and results in shorter flame length, so in this sence if we apply this work on deisel engine then it will provide a longer flame lif-off length as compared with the results of Siebers[5] who used a higher fuel temperature 463k and higher gas temperature 800K to 1300K.

CONCLUSION

- Increasing the combustion air temperature cause decrease of flame length as high ignition temperature is provided near the nozzle to the fuel to burn quickly even some time in case of high fuel flow rate.
- Increasing the injection pressure (injection velocity) decreases the NOx. The higher injection pressure leads to a higher kinetic energy that sends the fuel gas farther from the nozzle and during the time required for the injected fuel (oil) to be evaporated and ignited [5]. Relating with velocity an increase in the size of the orifice the kinetic

energy of the spray increases with the increase of fuel mass flow leading to longer fuel penetration and flame liftoff.
- Fuel with a comparative low density less penetrate into the burnt gases so less flame length while reduction in thermal NOx with far penetration of fuel into the gas pressure of the furnace occur with high density.

REFERENCES

Conference

[1] Ishiyama, T.,Ihara, T.Prediction of Ignition Processes in Fuel Sprays 6th international symposium of transport phenomenon in thermal engineering 9-13 May Seoul korea
[2] Karlsson,J.A.J.,Modeling of Ignition and Combustion of High Pressure Small Orifice diesel prays Using Chemical Model. COMODIA 94,Yokohama,Japan,11-14July 1994

Books

[3] Turns, S., An Introduction to Combustion – Concepts and Applications, ISBN 0-07-114783-7, McGraw-Hill,1996.
[4] Glassman, I. Combustion, 3rd edition, ISBN 0-12-285852-2, Academic Press, 1996.

Report

[5] Siebers, D., and Higgins, B., .Flame Lift-Off on Direct-Injection Diesel Sprays under Quiescent Conditions., SAE Paper 2001-01-0530, 2001.

Journals

[6] Dandy, D.S., and Vosen, S.R., "Numerical and Experimental Studies of Hydroxyl Radical ChemiluminescenceinMethane-Air Flames",Combust.Sci.Tech.,Vol.82,pp.131-150, 1992.
[7] F.R Menter, two equation eddy-viscosity turbulence models AIAA J.32(1994) 1589-1605
[8] L.Agarwal,J.C.Mandal,A.G.Marathe,comput. Fluids 30(2001) 607-620
[9] C.K.Westbrook, F.L. Dryer, Combust. Sci. Technol. 27
[10] Ishiyama, T., Shioji, M., and Ihara, T., .Prediction of Ignition Processes in Fuel Sprays Including Turbulent, Combustion Science and Technology, Vol. 130, pp. 350-358, 1997.
[11] Abraham, J., and Venkatraman, I., .Penetration and Dispersion of Transient Gas Jets and Sprays., Combustion Science and Technology, Vol. 130, pp. 315-334, 1997.
[12] C.Nicoli, effect of substituting fuel spray for fuel gas on flame stability in lean premixtures, combustion and flame 149(2007) 295-313

Reports

[13] Bergstrand, P., and Denbratt, I., .Diesel Combustion with Reduced Nozzle Orifice Diameter., SAE Paper 2001-01-2010, 2001.
[14] Kobori, S., Kamimoto, T., and Kosaka, H., .Ignition, Combustion and Emissions in a DI Diesel Engine Equipped with a Micro-Hole Nozzle., SAE Paper 960321, 1996
[15] Ishikawa, N., and Zhang, L., .Characteristics of Air-Entrainment in a Diesel Spray SAE Paper 1999-01-0522, 1999.
[16] Lille,S Experimental study of dingle fuel jet combustion, ISBN 91-7283-300-9,Royal Institute of Technology, Stockholm 2002.

Proceedings of the 4th BSME-ASME International Conference on Thermal Engineering
27-29 December, 2008, Dhaka, Bangladesh

STEADY STATE MODEL OF A BIMODAL SPACE AUXILIARY ELECTRIC POWER SYSTEM USING SIMULINK

M. Ruhul Amin and Stephen Astling

Department of Mechanical and Industrial Engineering, Montana State University, Bozeman, MT 59717, USA
(ramin@me.montana.edu)

ABSTRACT

This paper describes a model which has been created using Simulink^{TM}, a software package extension of MATLAB^{TM}, to simulate the steady-state performance of a closed loop Brayton cycle. The model allows the user to configure the individual Brayton cycle components including the turbomachinery, a recuperator heat exchanger, and a heat rejection radiator. The model takes into account non-ideal conditions such as friction losses, inefficiencies in the heat exchangers, and off-design performance characteristics of the turbomachinery. Each of the components was coded using program files called S-Functions. These functions are represented as blocks in a graphical block diagram and are connected together to represent the flow of data through the program. To run a simulation, the user is required to specify geometrical and thermophysical property values for each of the model components. The program then iteratively solves for the unknown parameters and the overall system efficiency. The model is useful for conducting parametric studies by running the model over a range of values for any parameter of interest. A parametric study was conducted by varying the radiator panel area to demonstrate this functionality.

Key words: *Brayton Cycle, Simulink, Power System, Thermal Performance.*

1. INTRODUCTION

Bi-modal space nuclear reactors are a topic of significant interest for use in future space exploration missions. A promising option for the auxiliary electric power generation system of these reactors is a direct gas-cooled reactor coupled to a closed loop Brayton cycle. This report describes a thermodynamic model that has been created using Simulink^{TM} a software package extension of MATLAB^{TM} [1] to simulate the steady-state performance of the coupled closed loop Brayton cycle in order to aid in the design and analysis of such a system. Work for this project was conducted as a follow on to a model originally created by Longhurst [2].

The model includes a reactor and reactor shield, turbomachinery, a recuperator heat exchanger, a waste heat rejection radiator, and interconnecting ductwork. Non-ideal conditions are taken into account such as friction losses, inefficiencies in the heat exchangers, and off-design performance characteristics of the turbomachinery. Inputs to the model include details about the geometry of each of the components and the thermophysical properties of the working fluid. The model then utilizes Simulink's block diagramming features to iteratively solve for the unknown model parameters so that the performance characteristics and overall efficiency of the system can be determined.

2. MODEL DESCRIPTION

The system modeled for this project is a direct gas cooled closed loop Brayton cycle. A diagram representing the top level of the model is shown in Figure 1. The working fluid was taken to be a gas mixture of helium and xenon, although other mixtures can be used. The gas passes directly through the reactor core where heat is added before being expanded through the turbine. The turbine produces work to drive the compressor and generator. After leaving the turbine, the gas passes through the recuperator heat exchanger where heat is recovered to improve the cycle efficiency. The gas then passes directly through a heat pipe radiator where the waste heat is rejected. The gas continues around the loop through the compressor, the cold side of the recuperator, the reactor shield, and finally back to the reactor.

Major inputs to the model include the required electrical power output by the generator, the reactor exit gas temperature and pressure, the thermophysical properties of the working fluid, and the geometry and performance characteristics of each of the components. The user must also specify an initial guess for some of the unknown parameters. During a simulation, each block executes in sequence, calculating its output conditions given an input temperature, pressure, and mass flow rate. Built in constraints for the steady-state model require that the calculated temperature and pressure of the working fluid at the end of the loop matches the temperature and pressure specified by the user at the beginning. The model also requires that the system produces the net amount of output power specified by the user.

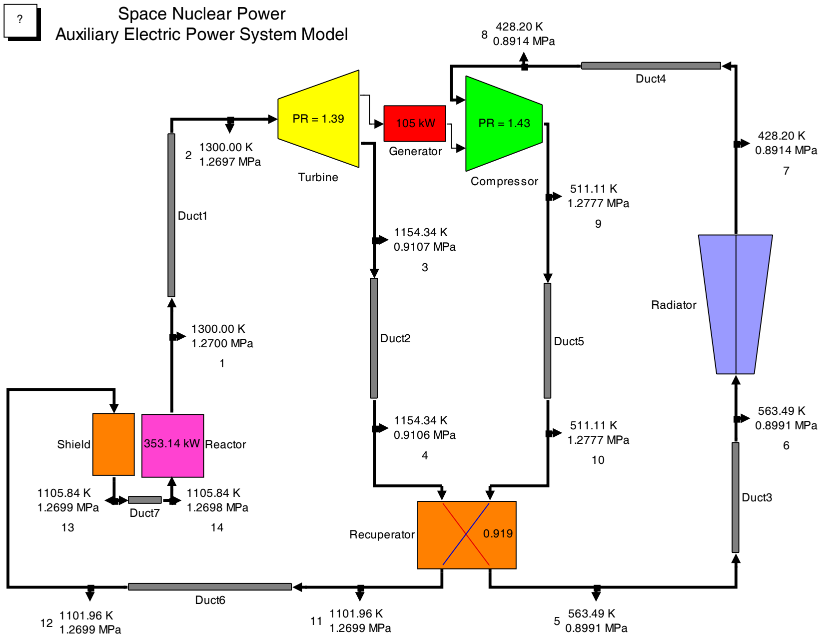

Figure 1. Block diagram for MATLAB Simulink Auxiliary Electric Power System Model

With these inputs and constraints, the model is then able to calculate the required reactor power and the resulting pressure ratio of the turbine and compressor. To solve for the unknown parameters, Simulink^{TM} starts with the initial guesses and then iterates using a robust version of Newton's method until a solution is found. Once this is done, the resulting intermediate loop temperatures and pressures are displayed on the block diagram along with the required reactor power, turbomachinery pressure ratios, and recuperator efficiency.

2.1 Turbomachinery

The turbomachinery components consist of the turbine, compressor, and the generator. Prior to running the model, the user must specify a performance map for both the turbine and compressor. The performance map relates the inlet mass flow rate, temperature, and pressure of the gas to the machine shaft speed, pressure ratio, and efficiency, Munson [3]. The performance maps are specified in a separate file as lookup tables and are read into the model automatically during the initialization phase of the model execution. Each time the turbomachinery blocks are called, the model determines the pressure ratio and efficiency based on the inlet conditions. The outlet temperatures and pressures are then found using equations (1)-(4) below. The generator, in turn, determines the net electrical power output based on the work of the turbine and compressor and includes a term for the mechanical to electrical efficiency, as shown in equation (5).

$$PR_t = \frac{P_{t1}}{P_{t2}} \tag{1}$$

$$PR_c = \frac{P_{c2}}{P_{c1}} \tag{2}$$

$$\frac{T_{t2}}{T_{t1}} = 1 - \eta_t \cdot \left(1 - PR_t^{\frac{k-1}{k}}\right) \tag{3}$$

$$\frac{T_{c2}}{T_{c1}} = 1 - \frac{1}{\eta_c} \cdot \left(1 - PR_c^{\frac{k-1}{k}}\right) \tag{4}$$

$$\frac{W_g}{\eta_g} = \dot{m}_t \cdot c_{pt} \cdot \left(T_{t1} - T_{t2}\right) - \dot{m}_c \cdot c_{pc} \cdot \left(T_{c1} - T_{c2}\right) \tag{5}$$

2.2 Recuperator

The recuperator S-Function solution method follows the format presented by Shah and Sekulic [4] for the rating problem of a single-pass counterflow or crossflow heat exchanger. In the rating problem, it is assumed that an existing heat exchanger has been selected and that the purpose of the analysis is to rate the exchanger performance so that the exchanger efficiency and fluid outlet temperature and pressure can be determined. The analysis assumes that the exchanger is operating under steady-state conditions, has negligible heat loss to the surroundings, and no flow misdistribution [4]. Prior to running the model, the user must specify various parameters such as the heat exchanger construction type, flow arrangement, and overall dimensions. Nondimensional heat transfer and pressure drop characteristics as well as details about the surface geometry are specified in a separate input file in the form of a lookup table. Each time the recuperator block is called, the heat transfer and flow friction factors are looked up in the table based on the calculated Reynolds number. The heat transfer and pressure drop equations are listed in equations (6)-(9).

$$\frac{1}{UA} = \frac{1}{\left(\eta_o hA\right)_h} + \frac{1}{\left(\eta_o h_f A\right)_h} + R_w + \frac{1}{\left(\eta_o h_f A\right)_c} + \frac{1}{\left(\eta_o hA\right)_c} \tag{6}$$

$$T_{h2} = T_{h1} - \varepsilon \frac{C_{\min}}{C_h}\left(T_{h1} - T_{c1}\right) \tag{7}$$

$$T_{c2} = T_{c1} - \varepsilon \frac{C_{\min}}{C_c}\left(T_{h1} - T_{c1}\right) \tag{8}$$

$$\Delta p = \frac{G^2}{2g_c\rho_i}\left[\left(1-\sigma^2+K_c\right)+2\left(\frac{\rho_i}{\rho_o}-1\right)+f\frac{L}{r_h}\rho_i\left(\frac{1}{\rho}\right)_m-\left(1-\sigma^2+K_e\right)\frac{\rho_i}{\rho_o}\right] \tag{9}$$

The overall thermal conductance *UA* is used to find the exchanger effectiveness ε using the appropriate ε-NTU relationship based on the selected flow arrangement. The outlet temperatures and pressure drops for both sides can then be found using equations (7)-(9).

2.3 Radiator

The radiator configuration consists of a heat rejection heat exchanger coupled to a heat pipe radiator in which the working fluid flows directly over heat pipes. The heat pipes in turn extend laterally into the radiator panel sections. This configuration was based on a key trades and analysis study by Frye et al. [5]. The heat exchanger manifold is assumed to be a square duct containing cylindrical sleeves in which the heat pipes are contained. Fins are included on the heat pipe sleeves to enhance heat transfer between the gas and the heat pipes. A schematic drawing of the manifold duct and finned heat pipe sleeves is shown in Figure 2.

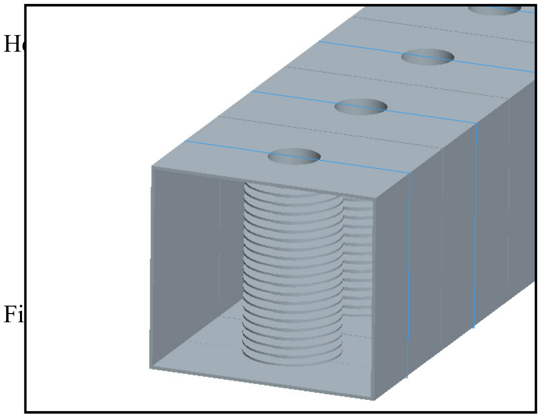

Figure 2. Heat rejection heat exchanger manifold and finned heat pipe sleeves

The radiator panels are based on a configuration discussed by Siamidis [6]. The two sided panel surface is assumed to be constructed of thin facesheets having high thermal conductivity. The facesheets in turn are thermally connected to square saddles containing the cylindrical heat pipes. The radiator is modeled using three separate S-Functions representing the heat rejection heat exchanger, the heat pipes, and the radiator panel. The first S-Function models the heat transfer between the working fluid and the heat pipes within the heat rejection heat exchanger and calculates the outlet temperature and pressure drop of the working fluid. Prior to running the model, the user must specify various parameters including the manifold length, width, and height. As with the recuperator, nondimensional heat transfer and pressure drop characteristics as well as details about the surface geometry are specified in a separate input file in the form of a lookup table. The solution method follows the format presented by Shah and Sekulic [4] for the rating problem of a single-pass tube-fin heat exchanger and assumes that the heat pipe evaporator section is of uniform temperature. The equations used are nearly identical to those used for the recuperator analysis.

The second S-Function models heat transfer through the heat pipes and accounts for a temperature drop between the evaporator and condenser sections. The user must specify parameters such as the heat pipe wall thickness, wick structure, and heat pipe length. The heat transfer is modeled as a thermal circuit and only includes the significant thermal resistances of the heat pipe wall and wick. The resistances were found using correlations by Peterson [7] based on the heat pipe wick structure selected. The resistances are summed in series as shown in equation (10). The heat transfer rate is then found using equation (11). During post processing, the user must verify that the heat transfer rate through the heat pipe does not exceed the limits dictated by its geometry and fluid properties.

$$R_{tot} = R_{pe} + R_{we} + R_{wc} + R_{pc} \tag{10}$$

$$q = \frac{T_e - T_c}{R_{tot}} \tag{11}$$

The third S-Function used in the radiator accounts for conduction from the heat pipe condenser section to the radiator panel facesheets and radiation to space. The user must specify various parameters including the panel length, facesheet thickness, emissivity, and a sink temperature. The heat pipe condenser section is assumed to be of uniform temperature. The panel fin effectiveness is calculated using a correlation found in the literature Gilmore [8] and was verified by Siamidis [6] for the assumed panel configuration using a finite difference model. The resulting heat transfer rate from the radiator panel is found using equation (12).

$$Q = A \cdot \varepsilon \cdot \eta \cdot \sigma \cdot T_c^{\,4} \tag{12}$$

For steady-state operation, the model requires that the heat transfer rate q is the same for the heat rejection heat exchanger, the heat pipes, and the radiator panel. The radiator is divided into a user specified number of sections and the above constraint is applied separately to each section. The model solves for the gas outlet temperature and pressure drop for each section until the final stream properties are found. An estimation of the overall radiator structure mass is also made.

2.4 Ducts

Ducts are included in the model to account for frictional losses in the pipes which connect the various system components. The flow in the pipes is assumed to be adiabatic and incompressible. This assumption is justified so long as the Mach number is less than about 0.3 [3]. The pressure drop is calculated based on frictional losses due to wall shear stress along the length of the pipe and also through minor losses as shown in equation (13).

$$\Delta p = \frac{1}{2} \rho \cdot v^2 \left(\frac{f \cdot L}{d} + K_L \right) \tag{13}$$

For turbulent flow, the friction factor f is calculated iteratively using an implicit form of the Colebrook formula [3]. Minor losses are accounted for using a user specified loss coefficient K_L, which could include effects from sudden pipe expansion or contraction, bends, tees, or valves. The user must specify parameters for each duct block including the pipe length, pipe diameter, pipe roughness, a loss coefficient, and an initial guess for the friction factor. The duct mass is calculated using a thin wall pressure vessel assumption and a user specified safety factor.

2.5 Reactor and Shield

The reactor and shield are currently the lowest fidelity model components. Both are modeled as ducts with uniform heating. The user must specify parameters including the duct diameter, length, and an initial guess for the friction factor. The stagnation temperature change of the working fluid is related to the reactor power using equation (14).

$$Q = \dot{m} c_p \left(T_2 - T_1\right) \tag{14}$$

The pressure drop is calculated using equation (13) in the same manner as for the ducts. The reactor shield solution method is identical to the reactor except that a user specified fraction of the reactor power Q_r is instead used. The reactor power is found by requiring that the calculated outlet temperature is equal to the exit temperature specified by the user.

3. MODEL DEMONSTRATION

To demonstrate functionality of the model, a test case was performed for a 100 kWe system to examine the effect of the radiator panel area on the overall efficiency of the system. The working fluid was taken to be a mixture of helium and xenon with a molecular weight of 40 and a mass flow rate of 3.5 kg/s. Because an accurate performance map for the turbomachinery was not available, the turbine and compressor efficiencies were instead input as fixed values of 0.9 and 0.85 respectively. The recuperator was assumed to be an offset strip-fin single pass counterflow heat exchanger with fin geometries and nondimensional heat transfer and pressure drop characteristics taken from Kays and London [9]. The radiator was divided into 10 sections. The radiator duct walls and heat pipe sleeves were assumed to be made of titanium. The heat pipe sleeve fin geometries and heat transfer characteristics were also taken from Kays and London [9]. The heat pipes used water and titanium walls and had a single-layer wire mesh wick structure with rectangular grooves. Properties for the radiator panels were taken from Siamidis [6]. The diameters of the interconnecting ductwork were sized to achieve a reasonable pressure drop. The model was run over a range of radiator panel areas while holding a set of predetermined parameters fixed. The radiator panel area was plotted versus the total radiated thermal power, the required reactor power, the overall system efficiency, and the amount of radiated power per unit mass of the radiator. These plots are shown in Figure 3.

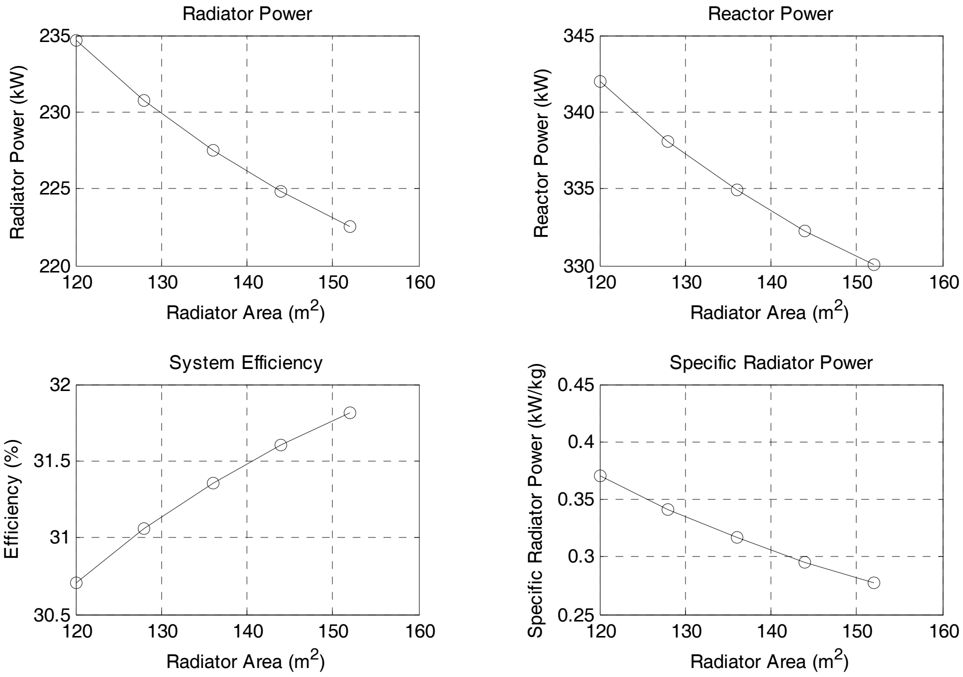

Figure 3. Selected model output values versus radiator panel area

The top two plots show that as the radiator panel area increases, both the required reactor power and the amount of radiated power decrease. The second row of plots show that while the overall efficiency of the system increases for larger radiator areas, the amount of power radiated per unit mass of the radiator decreases. We can conclude from this result that while the overall system power efficiency would be better for larger radiator areas, the corresponding increase in the radiator mass would at some point become too great a penalty. The above results agree qualitatively with those of more simplified models and with those reported by Longhurst [2]. While the input parameters are very different, the general trends and relationships between the radiator panel area and the other system parameters remains the same. This lends confidence that the model is behaving correctly and that it is indeed a more accurate representation of the actual system than previous model versions.

4. CONCLUSIONS

The model was created to simulate the performance characteristics of a closed loop Brayton cycle auxiliary electric power system. The model was developed using Simulink^{TM} to take advantage of its block diagramming features and iterative solution capabilities. S-Functions were written for each of the system components including the turbomachinery, a recuperator heat exchanger, a heat pipe radiator, the reactor and reactor shield, and for the interconnecting ductwork. Each of the model components were programmed to provide a high level of configurability which allow the user to conduct detailed parametric studies.

The highest fidelity components of the model were the recuperator and the radiator. The solution method for each followed the steps for a heat exchanger rating problem. The user was able to specify details about the geometry and performance characteristics including nondimensional correlations for the heat transfer and pressure drop coefficients. The radiator model included a calculation for the thermal resistance of the heat pipes and an accurate calculation of the effectiveness of the radiator panel fins. The ductwork components accounted for friction losses caused by wall shear stress along the length of the pipes and for minor losses due to pipe bends and other flow obstructions. The reactor and shield were the lowest fidelity components and only assumed uniform heating of a strait duct.

A parametric study was conducted for a 100 kWe system to demonstrate the functionality of the model. For the study, the model was run for radiator panel areas varying from 120 to 150 m^2 and compared to the resulting radiated power, reactor power, overall system efficiency, and specific power of the radiator. Plots were generated for each of the variables considered in order to visualize their general trends. Similar parametric studies can be conducted for any parameter of interest.

ACKNOWLEDGEMENTS

This work was partly supported by the Idaho National Laboratory.

NOMENCLATURE

A	Area
C	Heat capacity rate
c_p	Specific heat at constant pressure
d	Diameter
f	Fanning friction factor
ε	Effectiveness
η	Efficiency
η_o	Extended surface efficiency
ρ	Density
σ	Ratio of minimum free flow area to

G	Fluid mass velocity
g_c	Gravitational proportionality constant
h	Convective heat transfer coefficient
h_f	Fouling heat transfer coefficient
k	Specific heat ratio
K_c	Entrance loss coefficient
K_e	Exit loss coefficient
K_L	Pipe loss coefficient
L	Length
$\dot{m}$	Mass flow rate
P	Pressure
PR	Pressure ratio
Q	Power
R	Thermal resistance
r_h	Hydraulic radius
T	Temperature
UA	Overall thermal conductance
v	velocity
W	Work rate

	frontal area
σ	Stefan-Boltzmann constant

Subscripts

1	inlet state
2	outlet state
c	compressor (turbomachinery)
c	cold side (recuperator)
c	condenser section (heat pipe radiator)
e	evaporator section
g	generator
h	hot side
i	inlet state
m	mean of inlet and outlet state
o	outlet state
p	pipe
t	turbine
w	wall

REFERENCES

[1] MATLAB, www.mathworks.com, Trademark of Mathworks, Inc., 1994-2004.

[2] Longhurst, G. R., "Space Nuclear Power Auxiliary Electric Power System Model", INL/INT 05-00317, May 2005.

[3] Munson, B. R., *Fundamentals of Fluid Mechanics (4th edition)*, John Wiley & Sons, Hoboken, NJ, 2002.

[4] Shah, R. K., and Sekulic, D. P., *Fundamentals of Heat Exchanger Design*, John Wiley & Sons, Hoboken, NJ, 2003.

[5] Frye, P. E, and Allen, R., and Delventhal, R., "Brayton Power conversion System Study to Advance Technology Readieness for Nuclear Electric Propulsion – Phase I", in *Proceedings of Space Technology and Applications International Forum* (STAIF-2005), February, AIP Conference Proceedings, Albuquerque, NM, February 2005.

[6] Siamidis J, "Heat Rejection Concepts for Brayton Power Conversion Systems," Prepared for the Second International Energy Conversion Engineering Conference, Providence, Rhode Island, Aug. 16-19, 2004.

[7] Peterson, G. P., *An Introduction to Heat Pipes: Modeling, Testing, and Applications*, Wiley-Interscience, 1994.

[8] Gilmore, D.G. ,ed. *Spacecraft Thermal Control Handbook*, The Aerospace Press, El Segundo, CA, 1994.

[9] Kays, W. M., and London, A. L. *Compact Heat Exchangers*, Krieger Publishing Company, Malabar, Florida, 1984.

"Proceedings of the 4th BSME-ASME International Conference on Thermal Engineering
27-29 December, 2008, Dhaka, Bangladesh"

A NEW CORRELATION OF SINGLE-PHASE FRICTION FACTOR FOR HELICAL MICROFIN TUBES

Hasan M.M. AFROZ[1], Akio MIYARA[2]

[1]Department of Mechanical Engineering, Dhaka University of Engineering & Technology,
Gazipur-1700, Bangladesh, Email: hafroz@yahoo.com
[2]Department of Mechanical Engineering, Saga University, 1 Honjomachi, Saga-Shi, 849-8502, Japan, Email: miyara@me.saga-u.ac.jp

ABSTRACT

Single-phase pressure drop of eight helical microfin tubes with different fin dimensions have been measured experimentally with the aim of developing a generalized correlation of single-phase friction factor for helical microfin tubes. Water has been used as working fluid and the Reynolds number has been varied from 2×10^3 to 1×10^5. The experimental results show that higher helix angle, higher augmentation ratio and higher fin height to average inner diameter ratio cause more friction loss inside helical microfin tubes. The friction losses of helical tubes are around 1.05 to 2.2 times higher than that of a smooth tube depending on the fin geometric parameters and mass velocity of the working fluid. With the aid of present experimental data a new correlation of single-phase friction factor for helical microfin tubes has been proposed incorporating the effects of fin geometric parameters. The proposed correlation can predict the experimental data within ±20% for different helical microfin tubes with different fin dimensions.

KEYWORDS: *Helical microfin tube, Single-phase pressure loss, Single-phase friction factor, Correlation.*

1. INTRODUCTION

Microfin tubes are playing the important role for the single-phase and two-phase heat transfer enhancement of most heat exchangers of today's refrigeration and air-conditioning systems but at the same time they introduce an increment in pressure drop. In air conditioning and refrigeration applications, single-phase flow in microfin tubes is encountered in the superheated and subcooled regions of condensers and evaporators as well as in single-phase heat exchangers such as water cooling/heating fan-coil unit commonly used in ventilators and package air conditioners. Hence, it is of value to clarify the single-phase pressure drop characteristics and to obtain single-phase friction factor correlation of microfin tubes for the optimized design of heat exchangers. Moreover, prediction method of pressure drop and heat transfer during condensation and evaporation inside microfin tubes often incorporate single-phase friction factor correlation. Several researchers have reported experimental results and prediction method of single-phase friction factor inside microfin tubes. Wang and Rose [1] compared experimental single-phase friction factor results of 21 microfin tubes with the six earlier friction factor correlations. He reported that none was found to be in good agreement with all of the data but the Jensen and Vlakancic [2] correlation was found to be best and represent their database within ±21%. Inoue and Goto [3] measured single-phase friction factor of turbulent flow inside fourteen helical microfin tubes using water as test fluid and proposed a correlation of single-phase friction factor which can predict their data within

±10%. They have also checked the validity of Jensen and Vlakancic correlation with their data which shows under prediction by 40%. So it is difficult to find a generalized single-phase friction factor correlation for helical microfin tube which shows good response to the variation of fin geometric parameter. In this paper, experimental results of single-phase friction factor inside eight helical microfin tubes have been reported and a new correlation of single-phase friction factor for the helical microfin tubes has been proposed incorporating the effects of fin geometric parameters together with necessary comparisons with the existing correlations.

2. EXPERIMENTAL METHODOLOGY

The copper test tubes are of 7.0mm outer diameter and about 1 m of length and the test fluid, water is supplied to the test section from a supply tank by a pump. Water from the outlet of the test section is collected in another tank to calculate the flow rate by measuring the weight and time of the collection. Temperature of the outlet has been measured by copper-constantan thermocouple. The pressure drop of around 0.22m length of the test section has been measured by a differential pressure transducer. Accuracy of the measurements of the pressure difference and outlet temperature were within ±0.05 kPa and ±0.1 K, respectively. Configurations of the helical tubes are illustrated in Fig.1 and dimensions of all the test tubes are shown in Table 1. One smooth tube has been used to check the reliability of the experimental setup. The experimental results of single-phase friction factor of that smooth tube have been compared with the Blasius friction factor equation in Fig.2, which shows good agreement.

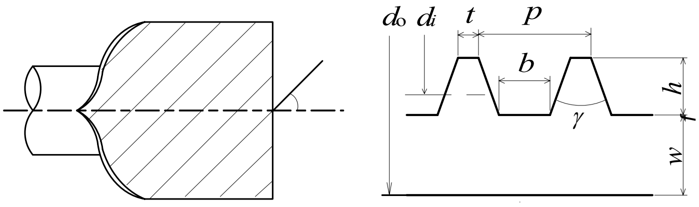

Fig.1 Configuration of helical microfin tube

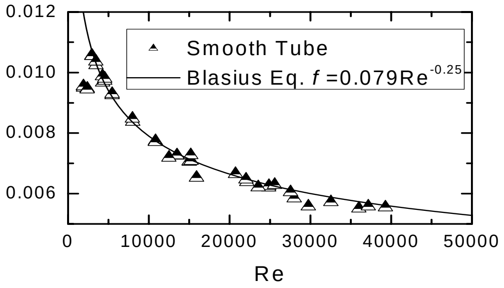

Fig.2 Experimental friction factor of smooth tube vs. Blasius equation

Table.1 Specification of test tubes

Tubes	d_o mm	d_i mm	p mm	h mm	h/d_i -	b mm	t mm	γ deg	β deg	w mm	n -	η -
Smooth	7.00	6.40	—	—		—	—	—	—	0.30	—	1.00
S-1	7.00	6.32	0.36	0.16	0.0253	0.11	0.07	58	18	0.27	60	1.70
S-2	7.00	6.36	0.36	0.21	0.0330	0.18	0.06	30	9	0.25	60	2.06
S-3	7.00	6.35	0.36	0.19	0.0299	0.18	0.07	28	18	0.26	60	2.00
S-4	7.00	6.35	0.35	0.22	0.0346	0.16	0.07	30	30	0.24	60	2.27
S-5	7.00	6.41	0.71	0.19	0.0296	0.54	0.07	27	18	0.26	30	1.53
S-7	7.00	6.25	0.30	0.22	0.0352	0.14	0.08	30	10	0.28	70	2.32
S-9	7.00	6.27	0.25	0.20	0.0318	0.10	0.06	27	7	0.28	85	2.46
S-10	7.00	6.36	0.41	0.21	0.0330	0.20	0.07	41	18	0.25	50	1.83

3. DATA REDUCTION

The single-phase friction factor value can be obtained from the experimental results of single-phase pressure drop inside helical microfin tubes by the following equation:

$$f = \frac{d_i \rho}{2G^2} \frac{\Delta P}{\Delta z} \tag{1}$$

where $d_i = d_0 - 2[w + h(p + t - b)/(2p)]$ is the average inner diameter of the helical tube.

The thermophysical properties of water are obtained from property table of water by using the temperature at outlet of the test section.

4. EXPERIMENTAL RESULTS AND PREDICTION

4.1 Experimental results

Figure 3 shows the single-phase friction factor of eight helical microfin tubes and one smooth tube that have been obtained from the experimental results of single-phase pressure drop. All the helical microfin tubes show higher friction loss than that of the smooth tube and the friction factor of helical tubes are around 1.05~2.2 times higher than that of the smooth tube depending on the mass velocity of the working fluid and the fin geometric parameters.

Helical tubes S-3 and S-5 have same helix angle β and almost same h/d_i value. Due to higher augmentation ratio η tube S-3 shows higher friction factor than the S-5 tube. Higher augmentation ratio represents more inner surface area which causes more wall shear stress. Tube S-4 shows higher friction factor than other tubes due to its higher helix angle. Higher helix angle causes more turbulence in the microfin tubes. Comparison between S-1 and S-10 tubes reveals that higher h/d_i value causes more friction loss. Higher h/d_i represents more roughness to the axial flow. In general, higher h/d_i, higher helix angle β and higher augmentation ratio η cause higher friction loss inside a helical microfin tube.

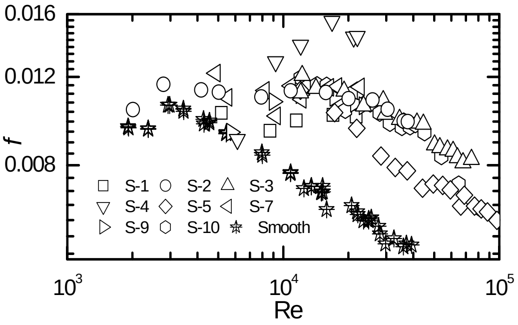

Fig.3 Experimental results of single-phase friction factor of helical microfin and smooth tubes

4.2 Comparison of experimental data with that of existing correlations

Fig. 4 shows the comparison of predicted friction factors by three earlier correlations with the present experimental data of helical microfin tubes against Reynolds number. For the comparison, the definition of the experimental friction factor Eq. (1) has been changed according to the definition of the used correlations [2, 3, and 4]. The prediction by Jensen and Vlakancic [2] correlation does not show good agreement which may be due to their correlation confinement for large inner diameter tubes (21.18~24.41 mm) while the present tubes are of 6.44~6.52 mm and also their correlation is valid for $2h/d_n$ value upto 0.06 but most of the present tubes are beyond of that. Carnavos's correlation [4] stands for relatively high fins so it does not predict the present experimental data of helical microfin tubes. Comparison between Inoue's correlation [3] and the present experimental data also do not show good agreement.

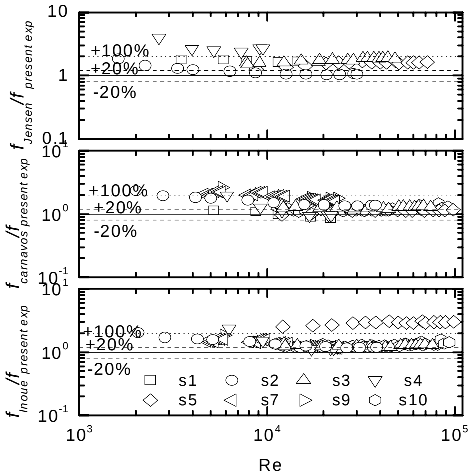

Fig.4 Ratio of predicted to measured friction factors of helical microfin tubes

4.3 Proposed correlation of friction factor for helical microfin tubes

According to the Prandtl's analysis [5] the mean velocity in turbulent motion through smooth tube can be expressed by the following equations

$$\bar{u} = 5.76\sqrt{\frac{\tau_0}{\rho}}\log_{10}\frac{0.1115d}{y_0} \tag{2}$$

where $\bar{u}$ is mean velocity, τ_0 is the shear stress at the wall and d is the inner diameter of the tube. The distance y_0 from the wall is of the order of magnitude of the thickness of the viscous sub-layer and depends on the condition of the wall. Colebrook [6] expressed y_0 as follows:

$$\frac{y_0}{d} = \alpha\frac{k}{d} + \varsigma\frac{\nu}{\upsilon_{*0}d} \tag{3}$$

where k is the roughness of the wall, ν/υ_{*0} is the ratio of the kinematic viscosity and the friction velocity, α and ς are two empirical constants to be found by experiments. Eqs. (2) and (3) can also be used for microfin tubes. For the helical microfin tube, k and d can be replaced by fin height h and average inner diameter d_i, respectively. From the experimental results of single-phase pressure drop inside helical microfin tubes and necessary manipulation, it has been found that modification of the $0.1115d$ term in the mean velocity expression of Eq.(2) by $0.078d_i$ and using y_0 for helical tubes give best agreement with the experimental result so the Eqs. (2) and (3) can be re-arranged for the helical microfin tubes as-

$$\bar{u} = 5.76\sqrt{\frac{\tau_0}{\rho}}\log_{10}\frac{0.078d_i}{y_0} \tag{4}$$

$$\frac{y_0}{d_i} = \alpha\frac{h}{d_i} + \varsigma\frac{\nu}{\upsilon_{*0}d_i} \tag{5}$$

Introducing friction factor in the Eq. (4) from the relation $\tau_0 = f\rho\bar{u}^2/2$ and using Nikurads's experimental value of ς as $1/10$ for the smooth tubes [6] in the Eq. (5), the following form of the single-phase friction factor inside helical microfin tubes can be obtained-

$$\frac{1}{\sqrt{f}} = -4.5 - 4.0\log_{10}\left(\alpha\frac{h}{d_i} + \frac{0.1414}{\mathrm{Re}\sqrt{f}}\right) \tag{6}$$

Now using the experimental results of friction factor in the Eq. (6) the values of α for eight different helical tubes have been calculated. The constant α depends on the geometry of the tube wall and it has been correlated in terms of the augmentation ratio η and the helix angle β of the fin of the helical microfin tubes by considering $\alpha = g(\beta)f(\eta)$ and $f(\eta) = \eta^a$. So $\alpha/\eta^a = g(\beta)$ should be constant for same helix angle tube.

Therefore, $\log\alpha = \log(g(\beta)) + a\log\eta$ represents a straight line with slope 'a'. Plotting the graph of $\log\alpha$ versus $\log\eta$ and linear fitting of the same helix angle tube data as shown in the Fig. 5 we have obtained the value of the exponent, 'a' as 3.7 and then plotting the graph of $\alpha/\eta^{3.7}$ versus $\cos\beta$ we have obtained the expression of α, Eq. (7) as shown in the Fig. 6.

$$\alpha = \eta^{3.7}\left[0.0019\left\{1 - 0.92(\cos\beta)^{3.8}\right\}\right] \tag{7}$$

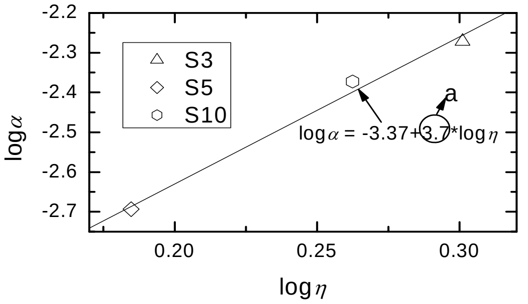

Fig. 5 $\log\eta$ **versus** $\log\alpha$ **(β = 18°)**

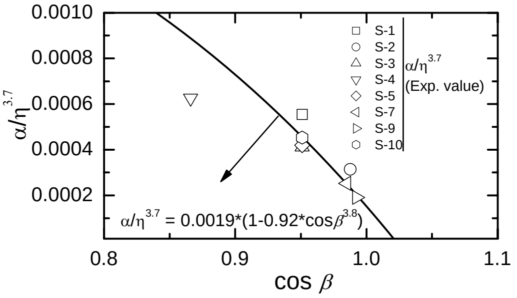

Fig.6 Graphical representation of Eq.(7)

So the final form of the friction factor of helical microfin tubes becomes

$$\frac{1}{\sqrt{f}} = -4.5 - 4.0\log_{10}\left(\alpha\frac{h}{d_i} + \frac{0.1414}{\mathrm{Re}\sqrt{f}}\right) \tag{8}$$

where the value of α can be obtained from the Eq. (7).

Fig. 7 shows that the proposed correlation can predict our present experimental data within ±20% and the experimental results of three microfin tubes of Jensen and Vlakancic [2] within around ±20%. Since the proposed friction factor correlation for turbulent flow is asymptotic in nature it may also be used for larger Reynolds number though it has been verified upto Reynolds number 1×10^5.

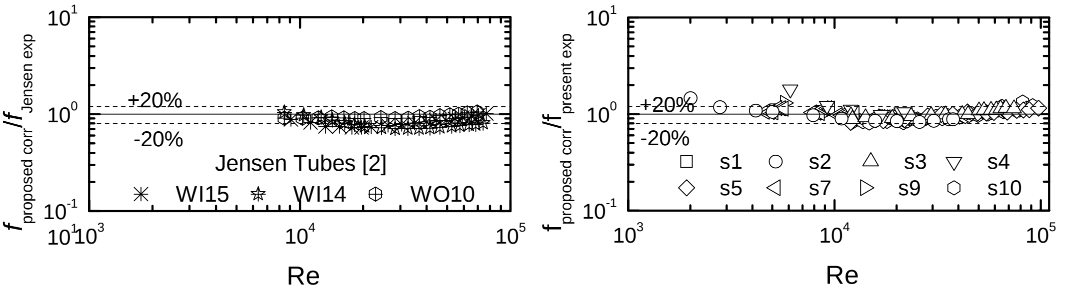

Fig. 7 Comparison of friction factor predicted by the proposed correlation with that of present experiment and Jensen experiment.

5. CONCLUSIONS

An experimental study has been carried out for the single-phase pressure drop inside eight different helical microfin tubes with different fin dimensions and a smooth tube. The experimental results show that higher helix angle, higher augmentation ratio and higher fin height to average inner diameter ratio cause more friction loss inside helical microfin tubes and friction factors of helical tubes are around 1.05 to 2.2 times higher than that of smooth tube depending on the fin geometric parameters and mass velocity of the working fluid. A generalized prediction correlation of single-phase friction factor for helical microfin tubes has been proposed including the effects of fin geometric parameters which can predict experimental data within ±20%.

6. NOMENCLATURE

A_m	inner surface area of fin tube, m^2	A	inner surface area of smooth tube ($d=d_i$), m^2
b	distance between fins at base, m	d	inner diameter of smooth tube, m
d_i	average inner diameter of fin tube , m	d_o	outer diameter, m
f	single-phase friction factor	G	mass velocity, $kg/(m^2{\cdot}s)$
h	fin height, m	k	roughness of wall, m
n	number of fins	p	fin pitch, m
ΔP	pressure drop, kPa	Re	Reynolds number = Gd_i/μ
t	fin tip thickness, m	$\bar{u}$	mean velocity, m/s
w	tube wall thickness, m	y	distance from wall, m
y_0	viscous sublayer, m	z	axial distance, m
Δz	pressure drop length, m		

Greek letters

α	constant	ς	constant
β	helix angle, ^{0}	γ	apex angle, ^{0}
μ	dynamic viscosity, Pa s	ρ	density, kg/m^3
η	augmentation ratio (A_m/A)	ν	kinematic viscosity, m^2/s
τ_0	wall shear stress, (N/m^2)	υ_{*0}	friction velocity ($\sqrt{\tau_0 / \rho}$), m/s

7. REFERENCES

[1] Wang, H.S., Rose, J.W., Prediction of effective friction factors for single-phase flow in horizontal microfin tubes, Int J Refrigeration, 2004, 27, p. 904-13.

[2] Jensen, M.K., Vlakancic, A., Experimental investigation of turbulent heat transfer and fluid flow in internally finned tubes, Int J Heat Mass Transfer, 1999, 42, p.1343–51.

[3] Inoue, N., Goto, M., Development of general correlations for pressure drop in single-phase turbulent flow inside internally helically grooved tubes, Proc. The 3rd Asian Conf. on Refr. and Air-cond., Gyeongu, Korea, 2006, p. 521-4.

[4] Carnavos, T.C., Heat transfer performance of internally finned tubes in turbulent flow, Heat Transfer Engineering, 1980, 1(4), p. 32-37.

[5] Schlichting, H., Boundary-layer theory, 7th edition, Mc Graw-Hill, 1979, p. 587-589.

[6] Colebrook, C.F., Turbulent flow in pipes, with particular reference to the transition region between the smooth and rough pipe laws, Journal of Institute of Civil Engineers, 1939, 11, p. 133-156.

Proceedings of the 4th BSME-ASME International Conference on Thermal Engineering
27-29 December, 2008, Dhaka, Bangladesh

CONTROL OF THE GAS FLOWS WITH OFFENSIVE ODOR IN A FACTORY

Lijo Vincent[a], Dong Sun Kim[b] and Heuy-Dong Kim[a]

[a] School of Mechanical Engineering, Andong National University, Andong, 760-749, Korea.
[b] FMTRC, Daejoo Machinery Co., Daegu, Korea.

(lijovincent@rediffmail.com)

ABSTRACT

Liquid crystal displays (LCD's) are continuously coated with some chemicals in the clean room of a factory. Spreading of these chemicals is causing serious problems both in controlling clean room quality as well as to the workers inside the factory. It is required to alleviate or properly control the offensive odor which is mainly composed of propylene glycol mono ethyl acetate, novolak resin and photo active compound. The control strategy employed is to bleed the offensive odor gas out the clean room. A full scale 3D Computational Fluid Dynamics (CFD) model was created with anisotropic porous media, chemical species transport with no volumetric reaction, and thermal diffusion with propane gas (tracer gas) to simulate the odor spreading. A segregated implicit solver with standard k- ε model is employed. The detailed CFD analysis made it possible to develop an effective method of ventilating the coater room and optimizing their capacities.

Key words: *LCD, Coater Room, bleed ratio, CFD.*

1. INTRODUCTION

A properly designed ventilation system is critical for any factory. Precise airflow and balance are required to prevent and to contain the spread of offensive odor, to maintain a uniform, optimal fresh air and to minimize the power requirements by optimizing recirculation air quantity.

The construction and testing of a full-scale physical model consisting of air supply and exhaust configurations to optimize ventilation design is very expensive and time consuming [1]. One of the best tools to evaluate smoke management system performance more accurately for large-volume spaces involves computer simulations based on CFD. With a CFD model, the computational region is divided into many sub-domains in which the fundamental equations of fluid flow and heat transfer are solved. The use of CFD models allows the building designers to evaluate various ventilation designs and provide for an optimum solution. Many configurations of supply and exhaust arrangements may be evaluated rapidly and more economically compared to typical physical models.

2. SIMULATION

The actual coating process is not as important as predicting the spreading of odious gases in the clean room and how to best manage it. Therefore, CFD models represented the coating process as a volumetric heat source with a soot emission rate. It is common practice to ignore radiation heat transfer and conduction heat transfer through all surfaces, but it is important for the modeler to develop methods to correctly predict odor growth rates [2].

Fig.1 shows the CFD domain with boundary conditions. Air enters from the ceiling of the coater room with a velocity of 0.35 m/s downwards. A large number of LCD panels are continuously coated on the coater table. From the coater surface chemicals (mainly composed of propylene glycol mono ethyl acetate, novolak resin and photo active compound) are propagating into the room, which is the source of odor inside the clean room. A perforated access floor is provided below the coater table. The access floor also helps to maintain unidirectional flow in the coater room, to prevent further mixing of chemicals inside the room.

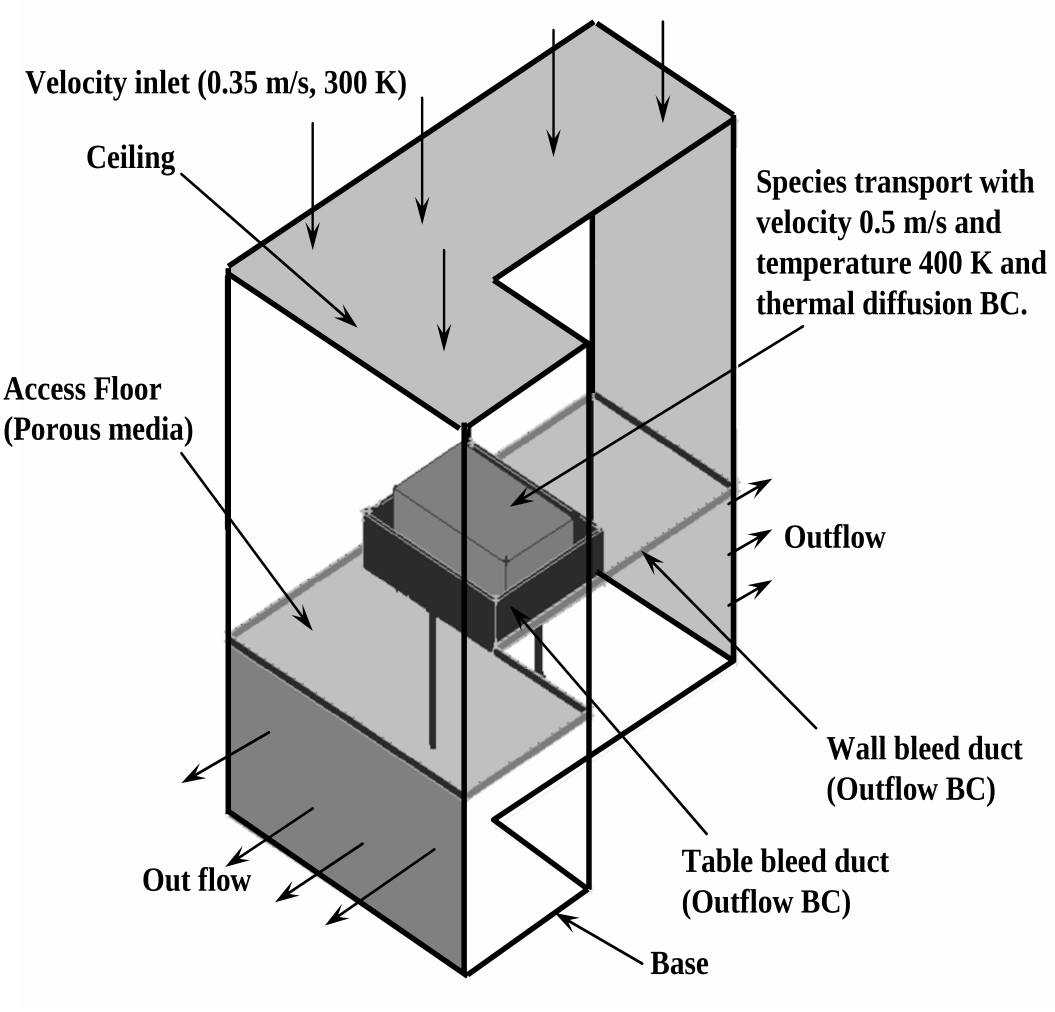

Fig. 1. Schematic of the coater room with boundary conditions

Fig.2 shows the bleed ducts around the coater table and wall of the room with detailed dimensions. It was found that table bleed duct is having more effect on the odious gas flows since it is nearer to the source of odor. Hence it was decided to optimize the table duct geometry with a fixed wall duct of 0.04 m bleed duct gap (W_2) and a height of 0.2 m (H_2). Mass split between table and wall duct were fixed in such a way that each combination gives identical bleed duct inlet velocity. Tab. 1 gives the details of test cases for 1m/s bleed duct inlet velocity for different table and wall duct geometries.

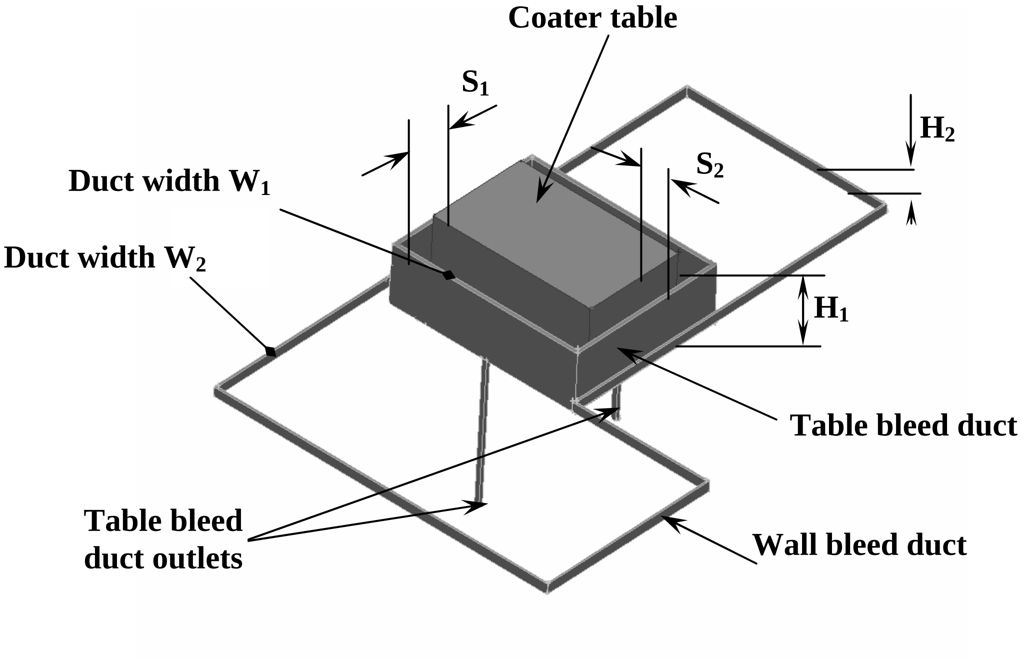

Fig. 2 Wall and table duct geometries

Tab. 1 Computational conditions

Test Cases	S_1 (m)	S_2 (m)	H_1 (m)	W_1 (m)	Table-duct Outflow (%)	Wall-duct Outflow (%)	Air Outlet (%)
I	0.2	0.2	0.35	0.04	3.5	12	84.5
II	0.2	0.2	0.35	0.08	7	12	81
III	0.2	0.2	0.7	0.04	3.5	12	84.5
IV	0.2	0.2	0.7	0.08	7	12	81
V	0.3	0.3	0.35	0.04	4	12	84
VI	0.3	0.3	0.35	0.08	8	12	80
VII	0.3	0.3	0.7	0.04	4	12	84
VIII	**0.3**	**0.3**	**0.7**	**0.08**	**8**	**12**	**80**
IX	0.6	0.3	0.35	0.04	4	12	84
X	0.6	0.3	0.35	0.08	8	12	80
XI	0.6	0.3	0.7	0.04	4	12	84
XII	0.6	0.3	0.7	0.08	8	12	80

3. CFD METHODOLOGIES

The general conservation (transport) equation for mass, momentum and energy is given by (1)

$$\frac{\partial}{\partial t}\int_V \rho\phi \, dV + \int_A \rho\phi V.dA = \int_A \Gamma\nabla\phi.dA + \int_V S_\phi \, dV \qquad (1)$$

where $\phi = 1$ for continuity equation,

ϕ = u, v and w for x, y and z momentum equations and

ϕ = h for energy equation.

The domain is discretized into finite sets of control volumes or cells. All partial difference equations are discretized into a system of algebraic equations and then solved numerically to render the solution field.

A full scale three dimensional, steady, segregated implicit solver with standard k- ε viscous model and species transport having no volumetric reactions was used. Interpolation scheme for the face pressure was standard and first order upwind scheme was used for all convection terms. SIMPLE pressure velocity coupling was enabled.

Porous media is modeled as a fluid cell zone with 60% porosity and viscous and inertial resistance in the flow direction is considerably lower than that in other directions.

Ideal gas equation is used to calculate density where as Cp and thermal diffusion coefficient of mixture material are calculated by mixing law and kinetic theory of gases respectively.

To judge the adequacy of airflow design for the parametric CFD analysis, two primary visualization methods were used. First, velocity vectors were plotted on several imaginary planes cut through the room (Fig.3). This technique gave a good indication of how air flowed throughout the room. The second visualization method involved the use of iso-surfaces/contour plots to show the boundary of a particular concentration of hydrocarbon gas. Two monitoring planes, plane A at distance of 2.0m and plane B at a distance of 6.0m from the ceiling of the coater room were used to obtain hydrocarbon distribution inside the clean room. When plotted in a 3-dimensional view, the iso-surfaces appear as clouds in space. The object of this technique is to reduce the size of the cloud to a minimum, thereby providing the best ventilation. Both visualization techniques were used on all parametric models until the best ventilation currents and smallest gas clouds were achieved.

4. RESULTS AND DISCUSSION

Path line and velocity vector plots gave us an initial guess about the placement of the table duct Fig.3. Concentration of the hydrocarbon was observed in two monitor planes one above the table and one below the porous floor (Fig.4).

Ducts near the table and wall are given different bleed ratios (ratio of mass of air bleeded out to the total mass). Simulations were done to study the effect of each duct independently and a bleed duct configuration (case VIII in Table 1) is finalized, since this duct geometry gave the smallest gas clouds and maximum percentage of hydrocarbon removed from the room for a fixed bleed ratio. 41.7% hydrocarbon removed for a bleed ratio of 0.2 (Fig.5).

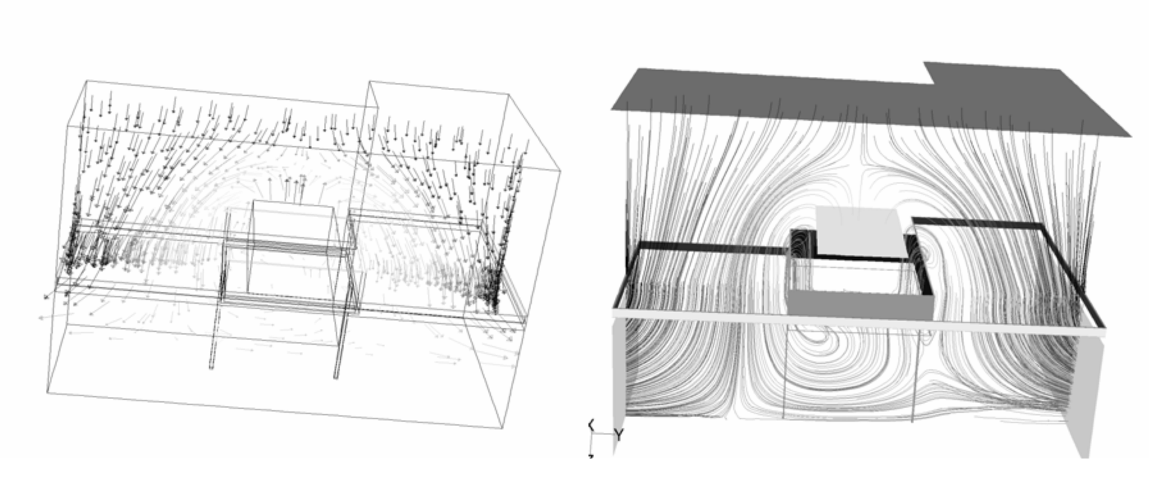

Fig.3 Velocity vector field and path lines around the coater table

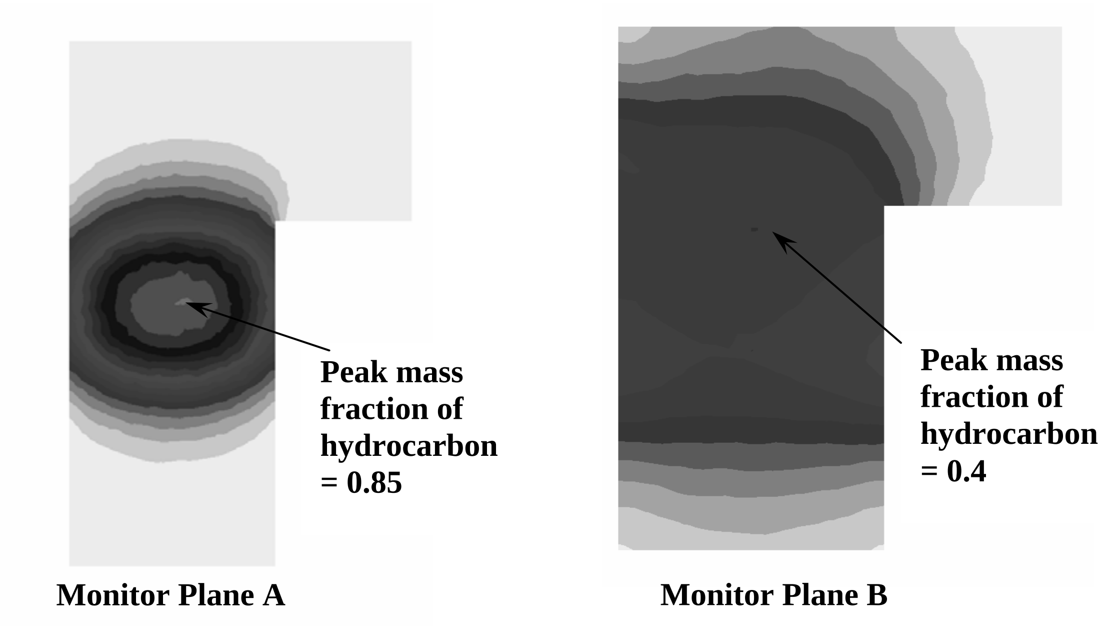

Fig.4 Hydrocarbon distributions on two-monitoring planes for case VIII

Simulations were also done with various bleed ratios in order to find the optimum bleed ratio for test case VIII (Fig.6). For maintaining a sufficient level of air purity at least 70 to 80 percentage of hydrocarbon has to be removed as per clean room standards. Hence a bleed ratio of 0.4 to 0.5 is recommended for the selected duct.

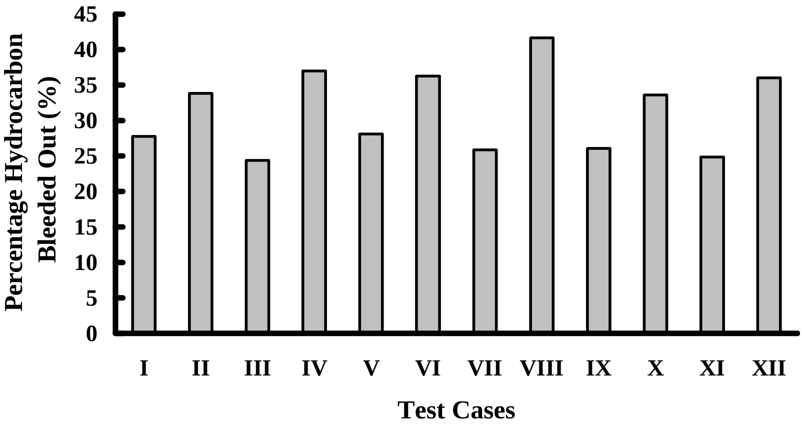

Fig.5 Percentage Hydrocarbon bleeded out for bleed ratio of 0.2

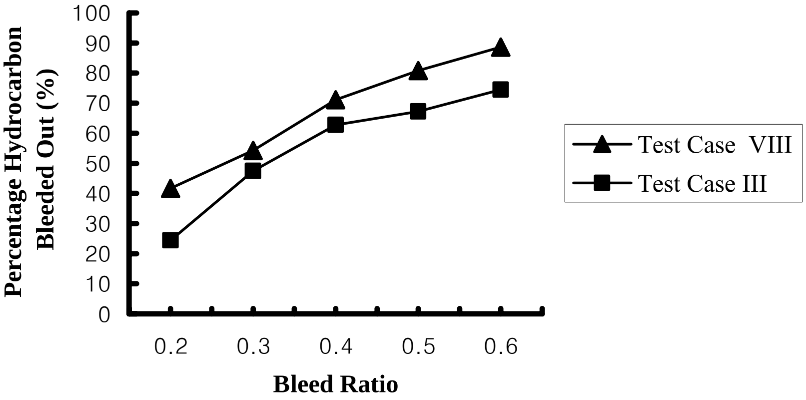

Fig.6 Percentage Hydrocarbon bleeded out for various bleed ratios

5. CONCLUSION

A table bleed duct placed at a distance of 0.3 m from the coater table with bleed duct gap of 0.08 m and 0.7 m height was found to give best ventilation (70 to 80 % hydrocarbon removed) for bleed ratios of 0.4 to 0.5, along with a wall bleed duct.

The detailed CFD analysis made it possible to develop an effective method of ventilating the coater room and optimizing their capacities. Without this analysis, it would have been necessary to substantially reduce the number of LCD panels coated in the coater room to maintain proper ventilation, thus, reducing the net output of the plant. The design was completed in less time and under the projected costs for testing of conventional physical models.

REFERENCES

[1] Craig, K.J., De Kock, D.J., Snyman, J.A., Using CFD and Mathematical Optimization to Investigate Air Pollution due to Stacks, *Numerical Methods in Engineering*, 44 (1999), pp. 551-565.

[2] Cook, M., Ji, Y.C., Hunt, G., CFD Modeling of Buoyancy-Driven Natural Ventilation Opposed by Wind, Proceedings, 9th International IBPSA Conference, Montreal, Canada, August 15-18, 1997.